# Multimodal Investigation of Brain Network Systems: From Brain Structure and Function to Connectivity and Neuromodulation

Hengda He

Submitted in partial fulfillment of the requirements for the degree of Doctor of Philosophy under the Executive Committee of the Graduate School of Arts and Sciences

**COLUMBIA UNIVERSITY** 

© 2023

Hengda He

All Rights Reserved

#### **Abstract**

Multimodal Investigation of Brain Network Systems: From Brain Structure and Function to

Connectivity and Neuromodulation

## Hengda He

The field of cognitive neuroscience has benefited greatly from multimodal investigations of the human brain, which integrate various tools and neuroimaging data to understand brain functions and guide treatments for brain disorders. In this dissertation, we present a series of studies that illustrate the use of multimodal approaches to investigate brain structure and function, brain connectivity, and neuromodulation effects. Firstly, we propose a novel landmark-guided region-based spatial normalization technique to accurately quantify brain morphology, which can improve the sensitivity and specificity of functional imaging studies. Subsequently, we shift the investigation to the characteristics of functional brain activity due to visual stimulations. Our findings reveal that the task-evoked positive blood-oxygen-level dependent (BOLD) response is accompanied by sustained negative BOLD responses in the visual cortex. These negative BOLD responses are likely generated through subcortical neuromodulatory systems with distributed ascending projections to the cortex. To further explore the cortico-subcortical relationship, we conduct a multimodal investigation that involves simultaneous data acquisition of pupillometry, electroencephalography (EEG), and functional magnetic resonance

imaging (fMRI). This investigation aims to examine the connectivity of brain circuits involved in the cognitive processes of salient stimuli. Using pupillary response as a surrogate measure of activity in the locus coeruleus-norepinephrine system, we find that the pupillary response is associated with the reorganization of functional brain networks during salience processing. In addition, we propose a cortico-subcortical integrated network reorganization model with potential implications for understanding attentional processing and network switching. Lastly, we employ a multimodal investigation that involves concurrent transcranial magnetic stimulation (TMS), EEG, and fMRI to explore network perturbations and measurements of the propagation effects. In a preliminary exploration on brain-state dependency of TMS-induced effects, we find that the propagation of left dorsolateral prefrontal cortex TMS to regions in the lateral frontoparietal network might depend on the brain-state, as indexed by the EEG prefrontal alpha phase. Overall, the studies in this dissertation contribute to the understanding of the structural and functional characteristics of brain network systems, and may inform future investigations that use multimodal methodological approaches, such as pupillometry, brain connectivity, and neuromodulation tools. The work presented in this dissertation has potential implications for the development of efficient and personalized treatments for major depressive disorder, attention deficit hyperactivity disorder, and Alzheimer's disease.

# **Table of Contents**

List of Table	es	iv
List of Figur	res	v
Acknowledg	gments	xx
Chapter 1: Is	Introduction	1
1.1 Overv	view	1
1.2 Motiv	vation	5
1.3 Backg	ground	8
Chapter 2: A	Advanced Methods for the Analysis of Structural and Functional MRI and Its	
Applications	s in Investigating the Negative BOLD Responses	14
2.1 Overv	view	14
2.2 Landr	mark-guided Region-based Spatial Normalization (LG-RBSN) for Analyzing	
Structural	l and Functional MRI	16
2.2.1	Introduction	16
2.2.2	Methods	21
2.2.3	Results	35
2.2.4	Discussion	55
2.3 Negat	tive BOLD Responses in the Human Visual Cortex	63
2.3.1	Introduction	63
2.3.2	Methods	67
222	Dogulta	70

2.3.4	Discussion	92
Chapter 3: S	Spatiotemporal Dynamics of Functional Brain Networks during Salience Processi	ng
and Its Asso	ociations to the Neuromodulatory System	. 101
3.1 Overv	view	. 101
3.2 An A	utomatic and Subject-specific Method for Locus Coeruleus Localization and	
Function	al MRI BOLD Activity Extraction	. 102
3.2.1	Introduction	. 102
3.2.2	Methods	. 103
3.2.3	Results	. 109
3.2.4	Discussion	. 109
3.3 Pupil	lary Response Is Associated with the Reset and Switching of Functional Brain	
Networks	s during Salience Processing	. 110
3.3.1	Introduction	. 110
3.3.2	Methods	. 113
3.3.3	Results	. 126
3.3.4	Discussion	. 144
3.4 Dyna	mic Causal Modeling of the Locus Coeruleus and preSMA Circuit in Attentional	
Processin	ng	. 160
3.4.1	Introduction	. 160
3.4.2	Methods	. 160
3.4.3	Results	. 161
2 4 4	Discussion	164

Chapter 4: Modulation of Functional Brain Networks using Transcranial Magnetic Stimulation	
and Its Brain-state Dependent Effects	66
4.1 Introduction	66
4.2 Methods	67
4.3 Results	70
4.4 Discussion	74
Chapter 5: Conclusions and Future Directions	76
5.1 Summary	76
5.2 Limitations and Future Work	79
References 1	85

# **List of Tables**

Table 2.1:	Dice similarity coefficient (DSC) between warped and fixed images of using ANTS are	d
	LG-RBSN in the simulation cases of (a) aligned and (b) mis-aligned initially 3	8
Table 2.2:	Comparison of the HRFs obtained for the cNBR and iNBR (cNBR vs. iNBR; * p 0.05; uncorrected).	
Table 2.3:	Comparison of the HRFs obtained for the PBR and NBRs (* p < 0.05; ** p < 0.0	Ι;
	uncorrected).	5

## **List of Figures**

Figure 2.2: Illustrate our method for automatic landmark extraction and matching for landmark-based regional non-linear registration with example on superior temporal cortex (STC) region. In step a), for STC region (Cyan color), vertices of the GW/WM and GM/CSF boundaries triangular meshes are extracted as landmarks (GM/CSF surface vertices shown as red dots, GW/WM surface vertices are not showing in the figure); In step b), landmarks of STC region are down-sampled by down-sampling the original dense surface mesh (green meshes) to a sparser surface mesh (red meshes) and sampled back to the original vertices (yellow dots) to keep consistency; In step c), correspondence of STC regional landmarks between the MNI template and the subject is established through spherical registration (corresponding landmarks in subject space shown as yellow dots); In step d), corresponding regional landmarks are initially aligned with linear transformations in 3D Euclidean space; In step e), a diffeomorphic non-linear

landmark-based registration is used to generate regional warping field for STO	C region
The step f) is only showing that STC regional warping field can be used to	warp the
subject's regional volume onto MNI template space. WM: white matter; G	W: grey
matter; CSF: cerebrospinal fluid.	26

- Figure 2.4: Comparison of ANTS and LG-RBSN registration results in cortical gyrus registration simulations with cases of moving and fixed images (a) aligned initially and (b) misaligned initially. In experiment (a), ANTS matched the whole gyrus mask perfectly but failed to accurately align the underlying 3 regions (yellow and green arrows mark the same location across images). In experiment (b), ANTS fell into a local minimum and failed to match even the binary mask of the entire gyrus. LG-RBSN matched the whole structure mask and regions perfectly in both experiments. ANTS: advanced normalization tools; LG-RBSN: landmark-guided region-based spatial normalization.
- Figure 2.5: Visualization of LG-RBSN estimated global displacement vector field of one example subject. The X, Y, and Z denote the displacement in each direction with a unit of millimeter. This displacement vector field has a maximum displacement of 16.1 and a minimum displacement of -17.3, and is mostly within a range between -8 to 8. The visualization shows that our method is capable to work with large and localized displacements. LG-RBSN: landmark-guided region-based spatial normalization.... 40
- Figure 2.6: Spatial normalized brain qualification evaluation comparison between LG-RBSN and ANTS. The first and the last columns illustrate subjects' brain images rigid aligned (showing as moving images) to MNI152 brain images (as fixed images). The second and the third columns illustrate subjects' brain images after ANTS/LG-RBSN non-

	performance compared to ANTS in red dotted circles highlighted areas. In subject 2,
	ANTS mismatched a Gyrus of the subject's cerebral cortex to a Sulcus in MNI152
	space, whereas LG-RBSN matched the corresponding Sulci properly. ANTS:
	advanced normalization tools; LG-RBSN: landmark-guided region-based spatial
	normalization
Figure 2.7:	Cortical regional DSC comparison between Affine, ANTS, CVS and LG-RBSN in
	different brain lobes. LG-RBSN shows significantly higher DSC in matching brain
	cortical regions than ANTS and CVS. ANTS: advanced normalization tools; LG-
	RBSN: landmark-guided region-based spatial normalization; CVS: combined
	volumetric and surface registration; DSC: Dice similarity coefficient
Figure 2.8:	DSC comparison between Affine, ANTS, CVS and LG-RBSN. LG-RBSN shows
	significantly higher DSC in matching brain cortical regions, sub-cortical regions, and
	cerebral WM than ANTS. LG-RBSN shows significantly higher DSC in matching
	brain cortical regions and cerebral WM than CVS. And LG-RBSN is more robust
	working with both young and older subjects compared to ANTS and CVS, as LG-
	RBSN shows less variance of DSC in matching brain cortical regions and cerebral
	WM. ANTS: advanced normalization tools; LG-RBSN: landmark-guided region-
	based spatial normalization; CVS: combined volumetric and surface registration;
	DSC: Dice similarity coefficient; WM: white matter
Figure 2.9:	Number of non-positive Jacobian voxels decreases along bijectivity constrain iterations
	for (a) forward (subject to MNI152) (b) backward (MNI152 to subject) warping field.
	The red curve and the grey region represent the mean and the standard deviation 47
Figure 2.10	: The processing pipeline for task-based fMRI data. The thick arrows show the transfer
	of 4D fMRI data, the double thin arrow shows the transfer of the 3D data, and the thin
	arrow shows the transfer of the parameters. ANTS: advanced normalization tools; LG-
	RBSN: landmark-guided region-based spatial normalization; EPI: echo planar
	imaging

linear registration to MNI152 brain images. LG-RBSN shows clearly better

- Figure 2.11: Distribution of the point estimates for visual task-based fMRI group level visual activation in brain contralateral occipital lobe using different spatial normalization methods (Left: for stimulating left visual hemifield; Right: for stimulating right visual hemifield). ANTS: advanced normalization tools; LG-RBSN: landmark-guided region-based spatial normalization; CVS: combined volumetric and surface registration.

- Figure 2.15: a) Illustration of a segment of the time-course of the visual-audio event related task. The blue line shows the timing of the auditory stimuli, the red line shows the timing of the visual stimuli, and the red stick line shows the subject responses (i.e., each time they press the button). In this sample demonstration, subjects were requested to attend to the visual stimulus and ignore the auditory stimulus. This is evident by the response pattern as the button is pressed twice as soon as the attended stimulus (i.e., visual

stimulus) is terminated. b) Flashing checkerboard visual stimulus presented on the left
and right hemifield69
Figure 2.16: The preprocessing pipeline for task-based fMRI data. The thick arrows show the transfer of 4D fMRI data, the double thin arrow shows the transfer of the 3D data, and the thin arrow shows the transfer of the parameters
Figure 2.17: Demonstration of activation/deactivation in response to right visual hemifield stimulation from a single subject in the attended condition. Positive BOLD responses are color-coded with red/yellow and negative BOLD responses are color-coded with blue/cyan. The unilateral visual stimulation induces robust PBR in the contralateral (relative to the stimuli) visual cortex accompanied by a robust cNBR in its vicinity, and a robust iNBR in the opposite hemisphere. Note that spatial smoothing is carried out here only for better illustration
Figure 2.18: Linearity of the a) cNBR, b) iNBR, and c) PBR with respect to stimulation duration. The blue and red dots show, respectively, the mean amplitudes for negative and positive BOLD responses of each subject. The black dots indicate the mean amplitude of the BOLD responses (i.e., averaged over all subjects) for each duration category. The black dashed lines represent the regression lines. The absolute values of the mean cNBR and iNBR amplitudes scale linearly with the stimulus duration. Please note that the timeseries have zero mean and unit standard deviation for this analysis, thus the relative change between categories carries the information and not the b-coefficient value at each category. As a sanity check for the method, we also applied the same method to the PBR. As expected, the PBR scales linearly with the stimulus duration.

Figure 2.19: The HRFs of positive BOLD, and contralateral/ipsilateral negative BOLD responses to a) attended and b) unattended visual stimuli. The curves are adjusted based on average of the HRF for 5 second prior to the stimulus onset. The unit of the magnitudes are percent changes (subtracted by mean and then divided by mean). Error bars represent the standard error of the mean. As is evident here, the two negative HRFs

are closely similar in terms of their overall dynamics and amplitudes (* p $< 0.05$ ; ** j
< 0.01; Bonferroni correction)
Figure 2.20: A) The definition of amplitude, time to peak, onset time, falling edge time, and time
to undershoot of the BOLD responses as illustrated for the PBR case. B-F) Student'
t-test of any statistically significant difference between the B) amplitude in percen
change, C) time to peak, D) onset time, E) falling edge time, and F) time to undershoo
of the two NBRs and PBR using sinc-interpolation up-sampled subject-wise HRF
Error bars represent the standard error of the mean. Statistically significant difference
are marked with asterisk symbols (* p < 0.05; ** p < 0.01; uncorrected) 80
Figure 2.21: Correlation of the mean amplitudes of the BOLD responses to the visual stimuli in
the attended (a, b, and c) and unattended (d, e, f) conditions. The value of the slop
Pearson correlation coefficient, the p-value of PCC are presented for each case. The
dashed black lines represent the regression lines with all the data, and the solid red
lines represent the regression lines with data after outliers removed. As is depicted
regardless of the attention condition, the subject-wise expression of the iNBR and
cNBR are significantly more correlated with each other than each one with the PBR
Figure 2.22: Subject-wise interhemispheric functional connectivity between regions with iNBI
and cNBR are depicted using boxplot alongside the subject-wise functional
connectivity between regions with iNBR and PBR using Pearson correlation
coefficient for a) right visual hemifield stimulation, b) left visual hemifield
stimulation, and c) the mean of the two functional connectivity. The results of the
group differences are also presented in each plot using Student t-test
Figure 2.23: Spatial distribution of PBR, cNBR, and iNBR overlaid on a sphere (inflated brain)
Boundaries of different visual areas V1 to V4 are depicted using different colors. A
is demonstrated here, iNBR has a higher spatial correspondence to PBR than to cNBR
Note that spatial smoothing is carried out only for better visualization

Figure 3.1: (a) fMRI data preprocessing and nuisance signal regression. The middle time point EP
volume was used as the reference in motion correction. No spatial smoothing was
applied. Motion parameters include 6 standard head motion parameters, their tempora
derivatives, and the squares of the above 12 motion parameters. (b) Intra-subject inter-
modality image registration
Figure 3.2: LC localization using a predefined LC atlas and the TSE image of each subject. In T1w
structural space, we use a criterion (Student's t-test) to determine a coarse LC location
Then, either TSE intensities in the LC mask or an LC atlas is transformed to EP
functional space for a more precise localization (using trilinear interpolation). The
result is one of three possible outcomes: 1) we localize the LC structure within $M_{1SD}$
2) we localize the LC structure within $M_{2SD}$ ; 3) we localize the LC structure with the
predefined LC atlas (i.e., without using any information from $I_{TSE}$ )
Figure 3.3: (a) GLM to estimate and test the contributions of PDB and PR to LC BOLD activity
(controlling for the variance due to the presence of stimuli). Trial-to-trial variabilities
of PDB and PR (VPDB and VPR) were modeled as boxcar functions with the
amplitude of each trial modulated by the pupil measurements. The boxcar functions
were convolved with a canonical double-gamma hemodynamic response function
before fitting into the GLM. (b) Group level statistical analysis in testing regression
weights against zero. * $p < 0.05$ ; ** $p < 0.01$
Figure 3.4: Flow chart illustrating the steps of data acquisition, preprocessing, single-modality
analyses, and cross-modality analyses
Figure 3.5: Schematic illustration of auditory oddball paradigm, single-trial analysis, and single
trial variability EEG-informed fMRI analysis. For each temporal window $\tau$ , we applied
a single-trial analysis with the extracted EEG data in the windows from all the trials
where a logistic regressor was trained to learn a weight matrix w maximally
discriminating the target vs standard trials. From the weighting on the EEG channels
with matrix w, a EEG discriminating component was computed as a low-dimensiona
representation of the EEG data. For example, two EEG sensors (channel $i$ and $j$ ) were
illustrated in the figure with a hyperplane discriminating target (red dots) and standard

- Figure 3.6: Network nodes definition with HCP-MMP atlas. The nodes (circles) of the SN, DMN, and DAN are overlaid with the selected network areas from the HCP-MMP atlas and the MNI152 brain image. The group-level region of interest masks (illustrated as spatial distribution maps) were obtained from majority vote across subjects......... 122

- Figure 3.9: Axial slices of the thresholded group-level significant activations in the traditional fMRI analysis of the oddball effects (contrast as oddball versus standard stimuli). The z-statistic maps were displayed on top of the MNI152 template brain image. FMRIB's Local Analysis of Mixed Effects (FLAME) from the FSL software package was used for the group-level statistical inference. The group-level statistical parametric maps were thresholded with z > 3.1 and corrected cluster significance threshold of p = 0.05 (Gaussian random field method). Regions in the dorsal attention network, salience network, visual and auditory cortex, primary somatosensory cortex, and subcortex

were identified as significant clusters. Please be noted that only the significant positive effects are shown here, and we did not observe any significant negative effects in the regions of the default mode network. The 'R' in the figure denotes right side of the brain.

Figure 3.10: Neural correlates of salience processing defined with the EEG single-trial variability (STV) informed fMRI analysis. (A) Timing diagram showing significant group-level activation clusters (p < 0.05 cluster-wise multiple comparison correction). STV in EEG temporal components discriminating the target versus standard trials was used to map the spatiotemporally distributed BOLD fMRI correlates spanning the trial. EEG STV information was incorporated as BOLD predictors in voxel-wise general linear model (GLM) analysis of fMRI, controlling for the variance due to the presence of stimuli and response time (RT). Cluster colors denote positive (red) and negative (blue) effects. Time is relative to stimulus onset. (B) Definition of salience processing nodes. Each node is a sphere centered on the peak voxel of the group-level STV EEGinformed fMRI analysis results. Centroid of peak locations was used for regions involved in more than one temporal windows. Node colors denote timing of involvement in the trial from early to late (temporal order: red, orange, yellow, green, and blue). All clusters and nodes were overlaid on a 3D Montreal Neurological Institute (MNI) 152 brain pial surface for visualization. BOLD, blood-oxygen-leveldependent; RH, right hemisphere; LH, left hemisphere; A, anterior; P, posterior; S, superior; I inferior; SPL, superior parietal lobule; M1, primary motor cortex; S1, primary somatosensory cortex; V2, secondary visual cortex; OFC, orbitofrontal cortex; IPL, inferior parietal lobule; IFC, inferior frontal cortex; mPFC, medial 

Figure 3.11: Network localization approach to map functional networks underlying salience processing nodes. (A) BOLD signals from the nodes (intersected with the grey matter mask) were extracted, controlling the nuisance signals (motion-related, ventricle and white matter signals). (B) Group-level functional connectivity (FC) results of each node (t-value, mixed-effect, p < 0.001 uncorrected). Seed-based FC analysis (with the task-related variability regressed out) was used to map network of regions connected

- Figure 3.12: Functional connectivity (FC) across salience processing nodes (group averaged z-score, mixed-effect, p < 0.05 uncorrected). fMRI BOLD signals from the nodes (intersected with the grey matter mask) were extracted, controlling the nuisance signals (motion-related, ventricle and white matter signals). Pearson's correlation was calculated between BOLD signals from the nodes (with the task-related variability regressed out). FC results identified three distinct groups of the nodes, organized by the EEG discriminating component time windows, indicating a temporal network organization of the nodes: 1) early-time network includes ISPL and rSPL, rM1, rV2, and IS1; 2) middle-time network includes IOFC and rOFC, IIPL, and rIFC; 3) late-time network includes mPFC, SMA, left frontal operculum and temporal pole..... 133
- Figure 3.13: Group-level mean effective connectivity modulated by the oddball stimuli between salience processing nodes (Bayesian parameter averaging;  $\alpha < 0.05$ ; Bonferroni corrected). Please be noted the results here reflect mean group effect. The orange and blue color represents positive and negative effective connectivity, respectively.... 135

- Figure 3.17: Whole brain temporal signal-to-noise ratio (tSNR) analysis was performed to assess the fMRI signal quality especially for the BOLD signal in the LC. The tSNR was computed for each voxel, by dividing the mean over the standard deviation. (A) Group-level mean tSNR map of preprocessed fMRI data (no spatial smoothing). The tSNR map of each run was spatially normalized into the MNI152 space, and then was averaged across all the runs of subjects. (B) Quantitative analysis and boxplot of tSNR distributions across runs in each ROI. The color denotes the tSNR before (red) and after (blue) the nuisance signal regression (motion parameters and BOLD signals in the 4th ventricle and the left and right hemisphere white matter and lateral ventricles). Before the functional connectivity analysis of the LC, we regressed out the BOLD signal in the 4th ventricle. The tSNR was computed for each voxel in the subject's native functional space, and then was averaged within the ROI (segmented with FreeSurfer). The LC two standard deviation template was used to delineate the LC

	30) (Grueschow et al., 2021)
Figure 3.18	3: T-statistic maps of the LC seed-based whole-brain functional connectivity results. We used a mixed effects model for group inference. Each subject's FC map was transformed into z-score with Fisher's Z transformation. And the FC z-score map was thresholded at p < 0.01. In the group-level, one sample student's t-test was performed to obtain the significant seed-based FC map of the LC (p < 0.001 uncorrected) Significant clusters were identified in the cerebellum, supplementary motor area (SMA), right and left anterior insula (AI), left postcentral gyrus, right precentral gyrus and thalamus.
Figure 3.19	9: Group-level mean effective connectivity modulated by the oddball stimuli between the nodes of DMN, SN and DAN (Bayesian parameter averaging; $\alpha < 0.05$ ; Bonferron corrected). The orange and blue color represents positive and negative effective connectivity, respectively.
Figure 3.20	2: Neural cascades of salience processing and the spatiotemporal network organizations of salience processing nodes. Previous seed-based and node-by-node functional connectivity results suggest both spatial and temporal network organizations of the identified salience processing nodes, respectively. We hypothesized that the node-specific involvement of these functional networks might indicate a crucial role of these nodes in the temporally evolved processes of salience signal and the relationships between these networks. ECN, executive control network
Figure 3.2	1: Cortico-subcortical integrated network reorganization (CS-INR) system. Previous brain-pupil relationships results aligned with the network switching model of SN in the literature, and also showed the role of the locus coeruleus norepinephrine (LC-NE) system in the network reset and the dynamic switching between anticorrelated networks (SN-to-DAN and SN-to-DMN). In support with the literature (Bouret and Sara, 2005), we hypothesized that the reset and switching might be modulated by the release of the NE, as an effect of the ascending neuromodulation, which indicates that the SN and LC-NE system might cooperate and share an integrated role in salience

processing. dACC, dorsal anterior cingulate cortex; lAI and rAI, left and right anterior
insula; ISPL and rSPL, left and right superior parietal lobule; IFEF and rFEF, left and
right frontal eye fields; mPFC, medial prefrontal cortex; PCC, posterior cingulate
cortex; lAG and rAG, left and right angular gyrus

- Figure 3.22: DCM and the endogenous/modulatory connections between the LC and preSMA. (A) and (B) represent the DCM connections before and after RETROICOR, respectively. The overlaid brain is only for illustration purposes. The numerical value with each connection represents the corresponding average effect at the group level. After RETROICOR, the results indicate a positive endogenous effect between the VOIs, whereas the self-connections are negative. (C) The comparison of endogenous connections before and after RETROICOR. (D) The comparison of context-dependent modulatory connections before and after RETROICOR. The 'STD' represents the standard stimuli situation, and the 'ODD' represents the oddball stimuli situation. 163

- Figure 4.2: Illustration of brain-state dependency analysis. Single-pulse TMS trials were grouped into four bins based on their timing relative to frontal alpha phase. The TMS trials in the figure were labeled according to their phase bin group using four different colors: red, yellow, blue, green. The onset times of TMS trials in each phase bin were convolved with the canonical HRF, resulting in four predictors of the fMRI BOLD time series. Response amplitudes (beta weights) were used to describe TMS-induced effects on each condition (frontal alpha phase).

- Figure 4.5: Brain state-dependency analysis results. (A) Preferred v.s. non-preferred phase contrast. Regions in the lateral frontoparietal network (L-FPN) were identified as significant clusters (t-value; p<0.001; uncorrected). (B) Spatial overlap between TMS response contrast and functional connectivity. Functional connectivity map using the

left DLPFC as the seed region showed a network overlapped with the TMS res	ponse
contrast map	174

## Acknowledgments

This journey began with an email. In 2016, I reached out to Dr. Ray Razlighi at Columbia Uniersity Medical Center with a question about the region-based spatial normalization project. Surprisingly, he responded with a detailed explanation. This interaction inspired me to come to the US and pursue my undergraduate thesis in Ray's lab, where I first entered the world of neuroimaging. Ray is helpful on my research and also inspiring. I always left his office feeling refreshed and energized. When Ray moved to Cornell, I joined Dr. Paul Sajda's lab, where he opened the door for me to explore various fields of neuroscience, including fMRI, EEG, pupillometry, TMS, and machine learning. Paul has been a great mentor, supporter and friend, always encouraging me to pursue any ideas that sparked my curiosity. And I always feel that I still have so many things to learn in the lab. I would also like to thank Dr. Linbi Hong for her patience and guidance when I joined the lab, as well as Xiaoxiao Sun for her help with the TMS project. I would love to thank my parents, Fuqiang He and Ying Zhou, my grandparents and other family members. I feel so lucky to have such wonderful parents who love me and support me. And I want to thank all my friends both in China and the US. I cannot imagine being here and finishing the PhD without the support from my friends. I would also like to thank the dissertation committee members: Dr. Joshua Jacobs, Dr. Qi Wang, Dr. Vince D Calhoun, and Dr. Yaakov Stern for their valuable feedback during my thesis proposal and defense.

Finally, I would like to thank the many researchers and scientists whose work has inspired me. Recently, Ray was telling me about the locus coeruleus and default mode network, and Paul was saying about the traveling waves in the brain. I still remember when we were having the lunch with Dr. Nikos Logothetis before his talk, he was talking about his research and I can see that his eyes light up with excitement. Maybe, the journey just started.

## **Chapter 1: Introduction**

#### 1.1 Overview

The primary goal of this dissertation is to investigate brain network systems with multimodal approaches. We aim to utilize a broad spectrum of data modalities to provide comprehensive coverage of the structural and functional characteristics of the brain network systems. Leveraging computational approaches, multimodal neuroimaging, simultaneous data acquisition, and neuromodulation, we will explore the organization and dynamics of brain network systems from various aspects including neuroanatomical variability, functional response properties, functional brain mapping, connectivity of brain circuits, and brain network perturbation. To be specific, we will firstly focus on a novel spatial normalization technique based on computational anatomy, to investigate the anatomy variabilities with structural magnetic resonance imaging (MRI) data. Secondly, we will examine the properties of the taskrelated brain hemodynamic response in the sensory system (i.e. visual cortex with simple visual stimuli), by assessing the blood-oxygen-level-dependent (BOLD) signal with functional magnetic resonance imaging (fMRI). Then, we will employ an auditory oddball paradigm to investigate the cognitive control network systems and their associations with the brainstem neuromodulatory system, where we will leverage simultaneous multimodal data acquisition of pupillometry, fMRI, and electroencephalography (EEG) to exam the functional organization and connectivity of the brain network systems. Lastly, we will explore a multimodal dataset with concurrent transcranial magnetic stimulation (TMS), fMRI, and EEG in depression treatment. This neuromodulation multimodal approach could potentially provide causal information for understanding brain network systems through the approach of probing and measuring. In summary, this dissertation will focus on the computational approaches and multimodal data

analyses in the investigation of structural anatomy, functional mapping, brain connectivity, and neuromodulation of the brain network systems.

In Chapter 2, we will describe a novel computational approach for the analysis of structural and functional MRI images, with an aim to investigate anatomy variability and develop an advanced preprocessing pipeline for neuroimaging studies. Computational anatomy is a research field in studying anatomy variability, specifically, it focuses on investigating biological variability and shape changes of anatomy in humans and primate monkeys through mathematical and computational methods (Grenander and Miller, 1998). As originally proposed by D'Arcy Thompson in 1917 (Thompson, 1992), differences in biological forms can be modeled as mathematical transformations. Biological forms are most likely to vary not only globally but also regionally. For example, brain anatomy variability lies not only in the global structures of fissures and lobes, but also local geometric structures like gyri, sulci and cortical folds, typically, simple mathematical transformations like rigid or affine transformation couldn't capture brain anatomy variability of differential geometry features in small scale. In this case, brain anatomy variability can be better modeled as a deformation field that has local features via a nonlinear transformation. The computational approach in the estimation of transformation between images to ensure spatial correspondence of homologous structures is called image registration. Specifically, image registration techniques can be used to estimate the deformation field between two arbitrary biological forms by solving an optimization problem, in which the objective function will quantify the distance between the deformed anatomy with the target anatomy, and it will also quantify the regularization on the deformation field itself. To reduce the dimensionality of the optimization problem, biological landmarks in the anatomy image can be utilized to quantify the distance and estimate deformation field. These landmarks are objectively

meaningful and reproducible points with existed biological homology counterparts in the compared biological forms. In this dissertation, we present a novel spatial normalization technique based on computational anatomy, which serves a powerful approach for quantifying brain anatomy and a more accurate preprocessing technique for neuroimaging studies. We will evaluate this method with an fMRI study involving the sensory systems, and provide a showcase example in studying the properties of both positive and negative BOLD responses in the visual cortex.

In Chapter 3, we will describe a study exploring the spatiotemporal dynamics of brain network systems, with a focus on the associations between the cortical networks and the brainstem neuromodulatory system. In our daily life, the brainstem plays a crucial role in the regulation of mood, consciousness, sleep, respiratory and cardiovascular functions, as well as many other autonomic and cognitive functions. Despite the extensive exploration of the cortex, the brainstem still remains a *Terra incognita*, with many aspects yet to be investigated, especially its associations with the cortical network systems. For example, it is still unclear how the brainstem relates to the organization, connectivity, and dynamics of the cortical networks. In Chapter 3, we will focus on the locus coeruleus-norepinephrine (LC-NE) system, which is an important brainstem neuromodulatory system with implications for attention, arousal, task performance and exploration behaviors. Specifically, we propose to develop an approach for localizing the LC and examining the associations and connectivity between the cortical network systems and the LC-NE system. The characteristics of such cortico-subcortical relationship are extremely important in various cognitive processes and neurological diseases. For example, a frontal-vagal network theory for major depressive disorder (MDD) and a noradrenergic theory for cognitive reserve have been proposed in the literature (Iseger et al., 2019; Robertson, 2013).

Additionally, the LC has been shown as the first brain region in which Alzheimer's disease (AD) related pathology appears (Braak and Del Tredici, 2014). In this proposal, we focus on the interactions between the cortical networks and the LC-NE system in the context of salience processing.

In Chapter 4, we will present a neuromodulation study, exploring the BOLD responses and connectivity changes in brain network systems under TMS perturbation. With the computational quantification of the TMS effects across brain networks, we aim to investigate the network-level effects of TMS, by assessing how the TMS-induced effects propagate to the brain network systems that are distal, but interconnected to the stimulation site. We also aim to quantify TMS-induced changes in whole-brain network connectivity. TMS over the left dorsolateral prefrontal cortex (L-DLPFC) is an FDA-approved treatment for depression. The quantification of TMS effects on brain network systems will have important implications for understanding the mechanisms of TMS in depression. With the probing of a specific brain region or a targeted circuit, and the measurement of the TMS responses across the brain network systems, this neuromodulation approach in conjunction with multimodal neuroimaging could potentially provide more causal evidence on the organization and dynamics of brain network systems, compared with the conventional correlation-based neuroimaging approach. Additionally, another important aspect of brain networks systems remains less explored is the dependency of the BOLD activity and connectivity on the brain-state. In this dissertation, by leveraging the multimodal neuroimaging acquisition of fMRI and EEG, we will examine the brain-state dependency of the TMS effects on brain network systems. This type of brain-state dependent analysis is important for the future efforts to temporally optimize and personalize TMS targeting in the treatment of depression.

This dissertation is organized as follows: We first explain the motivation, purpose of studies, and aims in Section 1.2. Then, we give a brief background on the current approaches and relevant studies in Section 1.3. In Chapter 2, we will describe the method developments and investigations on the brain structural anatomy and functional responses. In Chapter 3, we will discuss the connectivity of brain circuits and its associations with the brainstem neuromodulatory system. In Chapter 4, we will examine the brain's responses to neuromodulation, and the brainstate dependency effects. Finally, we conclude the thesis in Chapter 5 with a discussion on the limitations and future work.

#### 1.2 Motivation

Spatial normalization is an essential pre-processing step in many neuroimaging studies, where brain image registration will be performed to quantify the biological anatomy variability across individuals. The spatial alignment of brain structures will make between-subjects and between-groups comparisons possible by warping each subject's brain onto a standard space. Studying biological anatomy variability can help us understand how disease affects the anatomy compared to normal anatomy such as quantifying brain atrophy caused by certain disease like Alzheimer's Disease and multiple sclerosis. Most widely used spatial normalization methods are based on registration of the whole brain at once and suffer from local minima problem, resulting poor registration of cortical regions due to the complex shape of cerebral cortex and large intersubject variability (Klein et al., 2009).

In Chapter 2, we propose a novel landmark-guided region-based spatial normalization approach to accurately quantify the structural anatomy of the brain. Specifically, we locally register each cortical region independently based on automatic landmark matching, and regional

warping fields are composited and constrained to obtain a single global bijective warping field that can accurately match brain cortical regions. We propose to evaluate this approach with the functional imaging data, and provide a showcase example in the investigation of hemodynamic response in the sensory system to visual stimuli. In a unilateral visual hemifield stimulation, task-evoked positive BOLD response (PBR) is observed in the contralateral hemisphere, which is often accompanied by contralateral (Bressler et al., 2007; Shmuel et al., 2002; A. T. Smith et al., 2004) and ipsilateral (Tootell et al., 1998) negative BOLD responses (NBRs) in the visual cortex. In the second part of Chapter 2, we aim to investigate the temporal and spatial relationships between these two types of NBRs.

In Chapter 3, we aim to investigate the functional organization, connectivity and dynamics of the cortical network systems, as well as, their associations with the brainstem neuromodulatory system. In the cortical network systems, the interactions between the default mode network (DMN), dorsal attention network (DAN), and salience network (SN) reflect a fundamental functional aspect of the human brain organization and dynamics (Fox et al., 2005b; Menon, 2011; Tsvetanov et al., 2016; Y. Zhou et al., 2018). Here, we use simultaneously acquired pupillometry, EEG and fMRI data and an auditory oddball task to study these networks' interactions. The oddball paradigm has been widely used to investigate salience processing, where subjects are instructed to detect distinct infrequent targets in a stream of standard stimuli. In the previous neuroimaging studies, both the SN and the LC-NE system have been associated with P300 event-related potential and task-evoked pupillary response (TEPR) in salience processing (Aston-Jones and Cohen, 2005; DiNuzzo et al., 2019; Menon and Uddin, 2010). Even though the SN and LC have been well characterized with the switching model (Menon and Uddin, 2010) and adaptive gain theory (Aston-Jones and Cohen, 2005), respectively, it is still

unclear what their integrated roles are in salience processing. Recently, evidence has emerged that neuromodulatory systems are important factors in shaping functional network connectivity and reorganization (Zerbi et al., 2019). With TEPR as a psychophysiological marker of the phasic LC activity (Joshi et al., 2016), here, we aim to investigate this possibility by assessing the interactions between cortical networks and brain-pupil relationships in the context of salience processing. We hypothesize that the LC might play a role in the interactions between large-scale cortical networks in the processing of salient stimuli. We expect the results will shed light on our understanding of the functions of these two important systems and their interactions.

Additionally, to conduct direct neuroimaging of the LC using fMRI, we propose to develop a LC localization approach, where the BOLD signal in the LC will be extracted and we will examine the dyanmic causal modeling of the LC and pre-supplementary motor area (preSMA) circuit.

In Chapter 4, we aim to test the effect of TMS on brain network systems. We hypothesize that the single pulse TMS over the left dorsolateral prefrontal cortex will modulate the interactions between the brain networks systems. The modulations of the connections between specific brain systems might be dependent on the prefrontal EEG oscillation phase in the alpha frequency band at the time of TMS pulse delivery, where the phase of prefrontal EEG alpha oscillation will be used as an index of brain-state, and we exmaine this type of brain-state denpendency effects in brain network perturbation. Neuromodulation in conjunction with neuroimaging, for example, concurrent TMS-fMRI technique, has been shown as a powerful tool to provide causal information in understanding brain network systems and their interactions. For example, in (Chen et al., 2013), the authors found that TMS over the node of central executive network (CEN) induced causal downstream effects on the DMN. The combination of neuroimaging and causal techniques, such as TMS, allows to make stronger inference on the

causal role of these brain network systems (Bergmann et al., 2021; Siddiqi et al., 2022), which is essential for the translational research in the treatment of neuropsychiatric disorders. Based on the results of Chapter 3, where we exmaine the dynamics and reorganization of brain networks in task-related modulation, Chapter 4 will exmine the endogenous cortical network reorganization in neuromodulation with concurrent TMS-EEG-fMRI. We believe that these types of quantification and investigation of TMS-induced effects along with their brain-state dependency have important clinical implications. For example, in a study of TMS mechanisms in alleviating depression (Liston et al., 2014), the authors found that the TMS selectively modulates the connectivity between the CEN and DMN.

### 1.3 Background

In the study of anatomy variability, deformation field can be used to distinguish two samples of different forms and quantify the difference, which could be applied to the diagnosis of diseases with features of anatomic shape variability. An example was studied in (Bookstein, 1989) about the abnormality of the biological structures caused by Apert Syndrome. The x-ray images of the structures of the joining bones at the base of the brain are compared between patients and normal subjects, thin plate spline method was used to estimate the deformation field, and the geometry local features of the Apert deformation were found through decomposed principal warps of the deformation field. These local features include primarily a vertical deformation around landmarks Pterygomaxillary Fissure (Ptm) and Posterior Nasal Spline (PNS). Such deformation features can be used to quantify the severity of the disease. And in the studies of anatomy changes along time, deformation field can model, quantify and study the

features of human anatomy development and growth like brain atrophy, early brain development and human anatomy changes caused by disease, aging or under certain treatment.

Focusing on the field of neuroscience, investigating biological anatomy variability and shape changes is important, because studying inter-subject and interspecies brain anatomy variability can help identifying corresponded brain anatomy locations between subjects and species. Under landmark-guided registration setting, deformation field estimated with corresponded anatomy landmarks can drive a rational higher-level alignment of the anatomy. With this known correspondence in the anatomy, it can help automatical segmentation of brain structural and functional regions and help align the functional neuron activation of the brain for group level statistical analysis. In fMRI data preprocessing, deformation field estimation between subjects' native space and a standard space for functional data alignment is called spatial normalization. Proper estimation of the deformation field that is capable of quantifying the brain anatomy variability can help delineate a clearer group level averaged brain activation with a higher statistical power (Miller et al., 2005). For example, in a study of large deformation diffeomorphic metric mapping (LDDMM) (Joshi and Miller, 2000), individual variation in the cortical topography was studied. Cerebral cortex is a layered and highly folded shell of grey matter with complex anatomical and functional regions, and it is of the great interest in studying the brain functional organization. In this example, the cortical surface is unfolded onto a 2D flat plane. Geometry features associated with deep folds of the sulci and the fundi were used to generate the deformation field. And the deformation field was used to compare two different methods of cortical surface partition. In the study, another example of macaque brain anatomy variability between two macaques was studied with cryo-section images. Gyri and sulci labels were identified using geometry features of each brain and used to estimate the deformation field. Besides, this technique was also used for hippocampus segmentation and results were compared with manual segmentation. Studying brain anatomy variability across subjects can also be applied to build up deformable standard template model which is called brain atlas. For example, in (Vaillant et al., 2004), shape variability of hippocampus among 19 normal subjects has been studied and applied to build up a mean configuration among these subjects. In the geodesic shooting setting of diffeomorphic registration, the representative tangent space is a natural setting for studying anatomy shape variability and changes. In this example, the three largest variability variances of the hippocampus shapes were extracted with principal component analysis applied to the initial momentum in the linear tangent space, that represents the diffeomorphism flow of anatomy variability.

The research problem is to estimate a nonlinear deformation field with nice properties to model, quantify and analyze biological anatomy variability and changes via landmark matching. The most straightforward way to estimate a smooth deformation field from landmark correspondences is by using smoothing spline based interpolation methods such as thin-plate spline (TPS) method (Bookstein, 1989), which is commonly used in the field of studying biological shape difference and changes. To further estimate the deformation field that accounts for the shape variability in a more natural and physical way, regularization of the deformation field like diffeomorphism (smooth, invertible and invert smooth) property is pursued to be constrained into the deformation. It can be realized through large deformation diffeomorphism landmark matching method (Joshi and Miller, 2000), which has strong theoretical guarantees. However, as deformation field with diffeomorphism property is modeled through a flow of a vector field along time, this nonlinear diffeomorphic shape space is intractable in practice. To address this, the Diffeomorphism Deformation Tangent Space Representation (DDTSR) method

(Vaillant et al., 2004) used a geodesic shooting approach, which means tangent space representation of a geodesic flow on the diffeomorphism group. This linear tangent space at a single time point can represent the nonlinear diffeomorphism shape space, and it will make it easier to estimate the optimal deformation field and analyze the features of anatomy variability.

To investigate the functional aspects of the human brain, fMRI has been used for thirty years, with a growth in our knowledge of the organizations and functions of the brain. Large-scale functional brain networks, such as the DMN, DAN, SN, and ventral attention network (VAN), along with other networks have been identified and been associated with various cognitive processes and neurological diseases. However, brainstem, which plays a crucial role in our daily functioning, such as mood, consciousness and sleep, remains *Terra incognita*.

Neuroimaging of the brainstem is challenging and often overlooked. Because, the deep brain activity is almost invisible in the EEG scalp recordings. Even with the help of fMRI, the signals around the brainstem have a poor signal-to-noise ratio and most of the neuroimaging preprocessing pipelines were not designed well suitable for the brainstem areas.

One challenge in the study of brainstem and its associations with the cortex is nuclei localization. For example, the LC is a very small nucleus in the brainstem with many other nuclei in the vicinity, rendering the challenges in the location of the LC in neuroimaging data.

Localization approaches based on the LC atlas and neuromelanin-sensitive MRI have been developed (Keren et al., 2009; Sasaki et al., 2006). Another measurement that allows us to make inference on the neural activity in the LC is pupillometry. Pupil size not only changes in response to lighting conditions, but also can be modulated by cognition and mental processes, such as effort, arousal, attention, fluid intelligence, and cognitive states (Joshi and Gold, 2020; Jason S. Tsukahara and Engle, 2021). Studies have shown that non-luminance changes in pupil

diameter covary with LC electrophysiological recordings in non-human primates (Joshi et al., 2016). Recent studies have shown that the LC is the first brain region in which Alzheimer's disease related pathology appears (Braak and Del Tredici, 2014). The LC-NE system and its relationships and connections with cortical systems are critical in the understanding of many neurological diseases, such as AD. For example, a recent study has found that the structural connectome from the LC to transentorhinal cortex has decreased fiber integrity with increased AD severity (Sun et al., 2020). However, these interactions and connections are not fully understood. Some interesting hypotheses have been proposed. For example, the LC-NE system has been associated with the cognitive reserve (noradrenergic theory of cognitive reserve) (Robertson, 2013). Emerging findings seem to support this hypothesis, as the LC-NE system and the SN have both been closely related to novelty and efforts (Mather and Harley, 2016). And recent studies have associated baseline pupil diameter to fluid intelligence, which is a maker of cognitive reserve. It is reasonable to speculate that the connection and interaction between the LC-NE system and the SN may play an important role in various cognitive functions and have many clinical implications.

TMS-fMRI is a widely used technique for studying the mechanisms of TMS in depression treatment and investigating the causal role of brain network systems. Quantifying TMS-induced activity in the brain is important for understanding these mechanisms. One study using single-pulse TMS targeted at the left DLPFC showed that TMS involves areas with neuroanatomical connectivity to frontal-striatal-thalamic loops (Dowdle et al., 2018). Propagation patterns of the TMS-induced activity and inter-subject variability were further explored in (Vink et al., 2018). The authors showed that the propagation from the DLPFC to the subgenual anterior cingulate cortex (sgACC) is associated with the depression treatment efficacy.

However, substantial inter-subject variability in TMS effects has been widely reported, with evidence suggesting that connectivity between DLPFC target and the SN may play a role (Hawco et al., 2018). In the studies of TMS neuromodulation, researchers are also interested in how induced activity at a targeted local area can influence integrated activity throughout brain network systems (Cocchi et al., 2015). TMS in conjunction with multimodal neuroimaging data has been used to map the causal circuits underlying the induced effects (Bergmann et al., 2021; Chen et al., 2013; Siddiqi et al., 2022; Sydnor et al., 2022). Investigating the downstream causal effects of TMS has important clinical implications, as TMS has been shown to normalize the abnormal activity and connectivity in brain network systems including the DMN, CEN, and SN (Anderson et al., 2016). Additionally, network theories of neuromodulation treatments in depression, such as the frontal-vagal network theory (Iseger et al., 2019), have been proposed. Multimodal neuroimaging and computational approaches can be used to optimize and personalize TMS protocols for depression treatment in terms of spatial and temporal parameters (Faller et al., 2022; Fox et al., 2012; Pantazatos et al., 2023).

# Chapter 2: Advanced Methods for the Analysis of Structural and Functional MRI and Its Applications in Investigating the Negative BOLD Responses

## 2.1 Overview

As the size of the neuroimaging cohorts being increased to address key questions in the field of cognitive neuroscience, cognitive aging, and neurodegenerative diseases, the accuracy of the spatial normalization as an essential pre-processing step becomes extremely important. Existing spatial normalization methods have poor accuracy particularly when dealing with the highly convoluted human cerebral cortex and when brain morphology is severely altered (e.g. aging populations). To address this shortcoming, in the first part of Chapter 2, we propose a novel spatial normalization technique that takes advantage of the existing surface-based human brain parcellation to automatically identify and match regional landmarks. To simplify the nonlinear whole brain registration, the identified landmarks of each region and its counterpart is registered independently with topology-preserving deformation. Next, the regional warping fields are combined by an inverse distance weighted interpolation technique to have a global warping field for the whole brain. To ensure that the final warping field is topology-preserving, we used simultaneously forward and reverse maps with certain symmetric constraints to yield bijectivity. We have evaluated our proposed solution using both simulated and real (structural and functional) human brain images. Our evaluation shows that our solution can enhance structural correspondence compared to the existing methods. Such improvement also increases the sensitivity and specificity of the functional imaging studies, reducing the required number of subjects and subsequent study costs. We conclude that our proposed solution can effectively

substitute existing substandard spatial normalization methods to deal with the demand of large cohorts which is now common in clinical and aging studies.

In the second part of Chapter 2, we will utilize this novel spatial normalization approach in a task-based fMRI study of brain's responses in the sensory system. In a unilateral visual hemi-field stimulation, the task-evoked positive BOLD response is often accompanied by robust and sustained contralateral as well as ipsilateral negative BOLD responses in the visual cortex. The signal characteristics and the neural and/or vascular mechanisms that underlie these two types of NBRs are not completely understood. In the second part of this chapter, we investigated the properties of these two types of NBRs. We first demonstrated the linearity of both NBRs with respect to stimulus duration. Next, we showed that the hemodynamic response functions (HRFs) of the two NBRs were similar to each other, but significantly different from that of the PBR. Moreover, the subject-wise expressions of the two NBRs were tightly coupled to the degree that the correlation between the two NBRs was significantly higher than the correlation between each NBR and the PBR. However, the activation patterns of the two NBRs did not show a high interhemispheric spatial similarity and the functional connectivity between them was not different than the interhemispheric functional connectivity between the NBRs and PBR. Finally, while attention did modulate both NBRs, the attention-related changes in their HRFs were similar. Our findings suggest that the two NBRs might be generated through common neural and/or vascular mechanisms located in distal/deep brain regions that project to the two hemispheres.

# 2.2 Landmark-guided Region-based Spatial Normalization (LG-RBSN) for Analyzing Structural and Functional MRI

## 2.2.1 Introduction

Spatial normalization is an essential pre-processing step in many neuroimaging studies that makes between-subjects and between-groups comparisons possible by warping each subject's brain image onto a common or standard space. Spatial normalization is often performed by an underlying subject-to-subject or subject-to-standard image registration. Image registration, by definition, serves to make all subjects' neuroanatomical regions correspond to a standard space and consequently to each other. Without neuroanatomical correspondences, it is challenging if not impossible, to perform any across-subjects univariate or multivariate statistical analyses (likely the most essential step in obtaining and interpreting scientific results from neuroimaging data). Yet inter-subject registration of the brain, especially the human brain cerebral cortex, remains challenging due to its highly convoluted patterns of sulci and gyri with large inter-subject morphological variability. For example, cortical folding (e.g. sulci branches) is not consistent between subjects in many cortical regions (Van Essen, 2005). This not only makes their registration challenging, but also increases the likelihood of false-positive findings in neuroimaging studies (Desai et al., 2005; Liu et al., 2017). Better correspondence between neuroanatomical regions will improve the statistical power to detect any brain effect and will increase spatial specificity, resulting in a reduced number of required subjects and consequently study costs (Miller et al., 2005).

The most commonly employed spatial normalization methods perform either a volume-based non-linear registration of structural images in 3D Euclidean space, or a surface-based non-linear registration of the cerebral cortex surfaces in 2D parametric surface space. For example,

currently widely-used volume-based brain image registration methods include large deformation diffeomorphic metric mapping (Beg et al., 2005; Zhang et al., 2017), advanced normalization tools (ANTS) (Avants et al., 2008), Quicksilver (Yang et al., 2017), and VoxelMorph (Balakrishnan et al., 2019). Alternatively, commonly used surface-based methods include FreeSurfer (Fischl et al., 1999) and spherical demons (Yeo et al., 2010). There are also volume and surface hybrid methods available, that extend the cortex correspondence specified using surface-based registration to 3D Euclidean space. For example, Joshi et al. and Lepore et al. used harmonic mapping, whereas Postelnicu et al. used Navier operator of elastic diffusion for extending the surface correspondence to the volumetric space (Guo et al., 2005; Joshi et al., 2007; Lepore et al., 2010; Postelnicu et al., 2009).

The following lists the major concerns of volume-based spatial normalization: 1) Human neuroanatomical regions are distributed throughout a highly folded surface of the cerebral cortex which often makes the Euclidean distance less reliable in segregating adjacent regions with completely distinct functionality. For instance, the posterior and anterior banks of the Sylvian fissure have completely distinct functionalities, but they could be seen adjacent to each other in the Euclidean space. Therefore, even a small misalignment in the Euclidean space can exert drastic consequences in matching neuroanatomical regions. 2) There is almost no difference in the intensity of the cerebral gray-matter throughout the entire cortex. This makes intensity-based similarity measures, used often as the cost function in image registration, less sensitive in distinguishing different neuroanatomical regions throughout the cortex, particularly in adjacent ones. As we have demonstrated in our simulation, even if volume-based registration were able to align the cortical folding patterns between-subjects, it would still be less likely to correspond perfectly between different cortical regions along the aligned cortical gray-matter ribbons. 3)

Every non-linear image registration method relies on an underlying optimization step. Due to the complexity and large inter-subject variability in the cortical morphology of human brain, the optimization objective function becomes nonconvex almost at all cases causing many local optima that could be detected as the final solution, without providing an accurate correspondence between the regions. Thus, even the best performing volume-based non-linear registration (ANTS) results in a poor correspondence between the cortical regions (Dice similarity coefficient (DSC) of 0.6 to 0.7 (Klein et al., 2009)). Therefore, it is not surprising that even the recently-developed deep learning methods still have comparable performance as ANTS (Balakrishnan et al., 2019; Yang et al., 2017). Such poor correspondence can attribute the location of brain activation to different regions of the standard space in group-level analysis, reducing the statistical power available to detect significant effects.

To address these shortcomings, surface-based methods were proposed to directly align brain folding patterns of gyri and sulci based on their underlying curvature instead of relying on voxel intensity. For instance, Fischl et al. demonstrated that compared to nonlinear volumetric methods, a surface-based method more consistently aligns brain cyto-architectonic boundaries (Brodmann areas) (Fischl et al., 2008). Optimization in surface-based methods is more efficient as it works in a 2D surface space with fewer degrees of freedom. However, all surface-based spatial normalization methods are required to project functional data extracted from gray-matter volume to a cortical surface. This mapping process is challenging in practice and potentially problematic. For example, cortical surfaces are typically extracted from structural scans and projected onto functional image space. Due to excess geometric distortion in fast acquisition techniques, such as echo planar imaging (EPI) often used for fMRI acquisition and their low resolution, co-registration between functional and structural scans is likely to have inaccuracies

that directly result in sampling non-gray-matter regions. By sampling non-gray-matter regions or regions from a neighboring gyrus/sulcus onto the cortical surface, functional activation can easily get lost and affect the results of the group-level analysis. It has been shown that during mapping of functional activation from the volume to the surface, the functional signal can be diluted to neighboring gyri. This effect can be consistent across subjects and detected at the group-level, resulting in a false-positive cluster of brain activation otherwise absent in volume-based spatial normalization (Tucholka et al., 2012). Another shortcoming of the surface-based methods is that they cannot be applied for registering sub-cortical regions. Finally, almost all widely used brain image registration techniques whether volume- or surface-based, or a hybrid method, are based on solving the optimization problem of matching the whole brain at once, while suffering from the local minimum problem, resulting in poor correspondence between brain cortical regions.

To alleviate the local minimum problem in volume, surface, or hybrid methods, we use a region-based local registration technique (Razlighi, 2016), in which each brain's cortical/sub-cortical region is independently registered to its corresponding region. The superiority of the region-based method is due to the fact that inter-subject variability in each brain region is much smaller than the inter-subject variability in their whole brains. We have evaluated this automatic landmark-guided region-based local registration technique, which can accurately match brain cortical segmented regions with an averaged DSC of 0.8 (He and Razlighi, 2020). However, in our previous method and some other ROI-based methods (Miller et al., 2005), applying regional warping fields individually to each region will result in overlaps and gaps between regions after the warping, which makes it challenging to warp whole brain images and functional activation maps covering multiple regions. To overcome this, in this chapter, we propose to combine the

regional locally estimated non-linear displacement warping fields to obtain a smooth whole brain global displacement field using an inverse distance weighted (IDW) interpolation. However, the interpolated global deformation field is not guaranteed to preserve the topology during warping. Thus, we propose a residual compensation iterative algorithm to enforce bijectivity and topology-preserving properties into the global deformation field, which is also applicable to other given non-topology-preserving deformation fields. During the residual compensation regularization, to avoid losing the match of brain regions, we applied a region-based demons registration to match the cerebral cortex mask and sub-cortical regions at the same time.

The present study proposes a novel region-based volumetric spatial normalization method, which is the first study using regionally and independently estimated local non-linear displacement fields to composite a global bijective displacement field for the whole brain. And it is also the first study to use dense brain tissue surface vertices as pseudo-landmarks to guide the volumetric registration. Compared to volumetric methods, instead of matching voxel intensity, we propose to use landmarks guidance as the registration similarity measurement. In our method, we directly estimate a volumetric warping field using corresponding vertices on the surface of WM/GM (WM: white matter; GW: grey matter) and GM/CSF (CSF: cerebrospinal fluid) boundaries as automatically extracted landmarks in the 3D Euclidean space, which allows us to incorporate brain anatomical information and features into the volumetric registration process with exact correspondence. Compared to the surface-based methods, as our method extend the surface-based registration results to the 3D Euclidean space, our solution circumvents the projection of volumetric fMRI data onto the cortical surface. And our method is applicable to not only the cerebral cortex but also sub-cortical, cerebellar, ventricular, and other brain regions. In summary, we propose an automatic algorithm to extract and match the corresponding vertices on

the WM/GM and GM/CSF boundary surfaces in each anatomical regions; Next, to estimate a topology preserving warping field, we independently estimate a landmark-guided volumetric warping field via large deformation diffeomorphisms.

Section 2.2 is organized as follows: We first explain the detail of the proposed landmark-guided region-based spatial normalization (LG-RBSN) method in Section 2.2.2. We also explain the subjects' demographics and acquisition parameters used to acquire MRI scans in our experiments. In Section 2.2.3, we first used simulated 2D images to illustrate problems associated with volume-based methods as well as demonstrating the effectiveness of our proposed method in registering these simulated special cases. We then compare our method with other non-linear whole brain registration methods using real human brain images. Our results show that our method achieves higher DSC than the existing top performing volumetric registration method (ANTS) (Klein et al., 2009) and a hybrid registration method (combined volumetric and surface registration, CVS) (Postelnicu et al., 2009) in warping the brain's cortical regions, sub-cortical regions, and cerebral WM. In experiments with fMRI spatial normalization, our method performs better than ANTS and CVS with regard to the specificity and sensitivity of the fMRI activation at the group-level activation statistics. Finally, we include a discussion in Section 2.2.4 and we conclude this section in Section 2.2.5.

### 2.2.2 Methods

In this section we describe the details of our novel spatial normalization solution, specifically focused on accurately matching brain cortical regions, which have complicated topological variations. Constituting 40% of total brain mass, cortical regions are of primary interest to neuroscience field as the information-processing brain tissue (Saladin and McFarland,

2008). Figure 2.1 illustrates a flowchart of different processes required for our proposed LG-RBSN solution which starts with a surface reconstruction and parcellation of the cerebral cortex followed by our automatic regional landmark extraction and matching approach. Then, the landmark-guided geodesic shooting large deformation diffeomorphic registration is performed independently for each region resulting in a distinct warping field for that region. We then combine the regional warping field together using a novel interpolation technique, IDW, to give a single global warping field for the whole brain. Finally, the forward and reverse warping fields residual compensation is used to enforce bijectivity property into the global deformation field with a region-based Demons registration to keep matching of the sub-cortical regions and cerebral cortex during regularization.

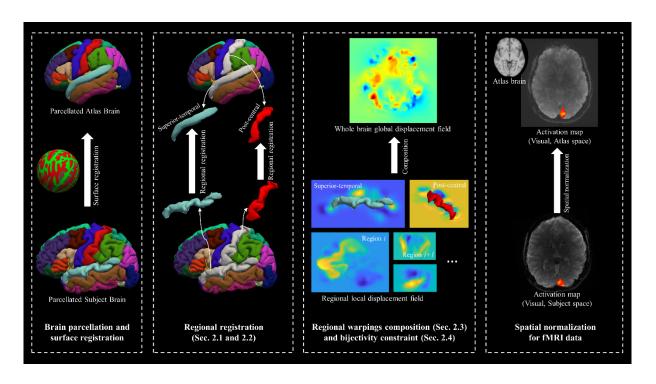


Figure 2.1: The pipeline for the landmark-guided region-based spatial normalization (LG-RBSN) solution. Subject's T1 image is processed with FreeSurfer for surface reconstruction and parcellation. Then, an automatic regional landmark extraction and matching approach (Subsection 2.1 Automatic regional landmark extraction and matching) is used to extract regional landmarks from the results of surface registration. For each region independently, the landmark-guided large deformation diffeomorphic registration (Subsection 2.2 Landmark-based large deformation diffeomorphic registration via geodesic shooting) is performed resulting in a distinct displacement field for that region. We then combine the regional displacement fields together using a novel interpolation technique (Subsection 2.3 Inverse distance weighted interpolation of neighboring region-based displacement composition) to give a single global displacement field for the whole brain. Finally, a residual compensation approach is used to enforce bijectivity property into the global deformation field (Subsection 2.4 Bijectivity constraints with residual compensation and Demons registration).

Automatic regional landmark extraction and matching Landmark-based image registration can be an alternative to the volumetric registration that circumvents the use of intensity-based similarity measures to estimate a volumetric warping field. Whereas existing landmark-based image registrations generate a direct and accurate correspondence between images and generally do not face the local minimum problem, they require a manual identification of corresponding

landmarks, which is labor intensive, subject to human error, and usually has a limited number of landmarks. For example, Anand A. Joshi et al. used manually labeled sulci features as landmarks to guide the registration (Joshi et al., 2007, 2005). Durrleman et al. used manually delineated sulcal lines, and represented them as currents in the registration (Durrleman et al., 2008). Shantanu H. Joshi et al. also used manually delineated sulci, but instead of currents they introduced a velocity representation of the sulci curves (Joshi et al., 2012). Auzias et al. applied an automatic technique to extract, identify and simplify sulcal landmarks, and the sulcal edges were represented as mathematical measures in the registration (Auzias et al., 2011). Here, instead of using landmarks only from sulci lines, we define landmarks as dense pseudo-landmarks from the vertices of the brain tissue surface triangular meshes to guide the registration, which covers both the sulci and gyri of the cortical surface and the white matter surface. And we propose an automatic landmark identifying and matching procedure that accounts for approximately 2000 landmarks per region, with totally around 136,000 landmarks per subject.

Our method starts with processing subjects' structural T1-weighted images and MNI152 template using FreeSurfer pipeline (http://surfer.nmr.mgh.harvard.edu/, RRID:SCR\_001847), resulting in 68 cortical regions (Fischl et al., 2004). However, using FreeSurfer for initial reconstruction and delineation of the human cerebral cortex is just an arbitrary choice, other accurate surface reconstruction and delineation methods can also be used for this purpose. The framework of landmarks matching and regional registration is illustrated in Figure 2.2. For each region, vertices of the WM surface (boundary between GM and WM) and pial surface (boundary between GM and CSF) triangular meshes are extracted as landmarks using the labels assigned by FreeSurfer's cortical surface parcellation algorithm. The pial surface landmarks of one of the cortical regions (superior temporal cortex) are illustrated in Figure 2.2(a). To reduce

computation, the landmarks for regions with large number of landmarks are down-sampled. Based on the time-accuracy tradeoff, a fixed down-sampling rate is assigned to each region varying from 10% to 60%. In our experiment, the down-sampling process only sacrifices a small amount of accuracy, but it substantially reduces the computation time. Down-sampled vertices are then matched back to the closest vertices on the original sphere mesh to maintain consistency between down-sampled vertices and original ones. The down-sampled pial surface landmarks of one of the cortical regions (superior temporal cortex) are illustrated in Figure 2.2(c). Next, the correspondence of regional landmarks between each subject and the MNI template is established through the FreeSurfer spherical registration algorithm (Fischl et al., 1999). Specifically, the MNI vertices of each region are transformed into the subject's spherical surface space using the spherical registration. For each projected vertex, the closest vertex of the subject's original vertices is identified as the matching landmark in the subject's space.

We then performed two initial linear alignments between corresponding landmarks for each region, including a global and a local transformation, independently. First, assuming that we have m regions  $R_i$  (i=1,...,m), subject space  $S(x), x \in \Omega_S \subset \mathbb{R}^3$ , and MNI space  $M(x), x \in \Omega_M \subset \mathbb{R}^3$ , the subject's brain structural image is registered to the MNI brain template entirely with an affine transformation A(x), and subsequently each subject's cortical region mask is separately registered to its corresponding region in MNI space with a translation only transformation  $A_i'(x), i=1,...,m$ . In our experiments, translation only transformations generate more appropriate linear initial alignments for brain cortical regions without causing any overfitting for the subsequent regional non-linear registration. Regional landmarks are transformed using these two linear transformations for initial alignment. The final regional warping field is the concatenation of two initial linear transformations and the non-linear warping field.

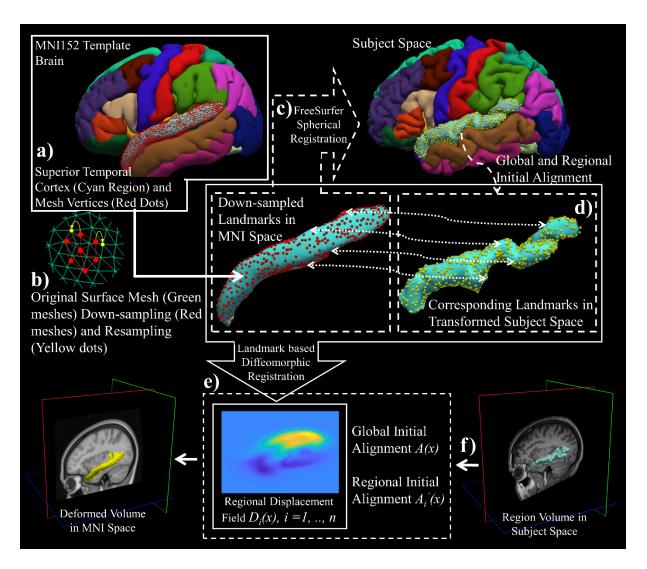


Figure 2.2: Illustrate our method for automatic landmark extraction and matching for landmark-based regional non-linear registration with example on superior temporal cortex (STC) region. In step a), for STC region (Cyan color), vertices of the GW/WM and GM/CSF boundaries triangular meshes are extracted as landmarks (GM/CSF surface vertices shown as red dots, GW/WM surface vertices are not showing in the figure); In step b), landmarks of STC region are down-sampled by down-sampling the original dense surface mesh (green meshes) to a sparser surface mesh (red meshes) and sampled back to the original vertices (yellow dots) to keep consistency; In step c), correspondence of STC regional landmarks between the MNI template and the subject is established through spherical registration (corresponding landmarks in subject space shown as yellow dots); In step d), corresponding regional landmarks are initially aligned with linear transformations in 3D Euclidean space; In step e), a diffeomorphic non-linear landmark-based registration is used to generate regional warping field for STC region. The step f) is only showing that STC regional warping field can be used to warp the subject's regional volume onto MNI template space. WM: white matter; GW: grey matter; CSF: cerebrospinal fluid.

# Landmark-based large deformation diffeomorphic registration via geodesic shooting

Traditional landmark-based non-linear image registration methods are based on smoothing spline interpolation with different radial basis functions, such as thin-plate spline (Bookstein, 1989). Yet due to their questionable invertibility, spline-based methods often fail when dealing with the human brain's highly convoluted topology, especially in cases that require large deformation, dense placement, or curved trajectories of landmarks (Joshi and Miller, 2000). To address the problem of large deformation, we use a large diffeomorphic deformation method with geodesic shooting (Vaillant et al., 2004) to estimate a valid warping field for each cortical region. With the optimal landmarks' geodesic paths, both forward and reverse diffeomorphic regional deformation maps are estimated. Here, we provide a review of the large diffeomorphic deformation registration for the sake of completeness. For the initially aligned corresponding landmarks  $x_n$  and  $y_n$  (n in 1, ..., N) in the same coordinate, image warping is described as a time-varying flow quantified by a transport equation  $\frac{d\phi(x,t)}{dt} = v(\phi(x,t),t)$ . With time denoted by  $t \in [0,1]$ , spatial space by  $x \in \Omega \subset \mathbb{R}^3$ , a time-dependent flow by  $\phi(x,t)$ , and a velocity vector field by v(x, t). This ordinary differential equation has the solution of  $\hat{\phi}(x, t) =$  $\int_0^t \hat{v}(\hat{\phi}(x,t'),t')dt' + x$ , with initial condition  $\phi(x,0) = x$ . The final deformation map is taken as the end point of this image warping flow which is  $\hat{\phi}(x, 1)$ , and the final displacement vector field is denoted as  $D_i(x) = \hat{\phi}_i(x, 1) - x$  for the  $i^{th}$  region.

The deformation map is constrained to be diffeomorphism through a regularization penalty on the smoothness of the velocity vector field. Thus, to obtain diffeomorphic registration, the optimization objective function becomes the following:

$$J(v) = \int_0^1 \int_{\Omega} ||Lv(x,t)||^2 dx dt$$

$$+ \sum_{n=1}^N [y_n - \phi(x_n, 1)]^T \Sigma_n^{-1} [y_n - \phi(x_n, 1)]$$
(2.1)

where  $x_n$  and  $y_n$  are moving and fixed landmarks, respectively, and L is the linear momentum operator defined on a Hilbert space V with Lv ( $v \in V$ ) considered as a mapping from V to  $\mathbb{R}^3$ , which satisfies  $||v_t||_V^2 = Lv_t(v_t)$ . The mapping  $Lv_t$  is defined as the momentum of the system at time t. The second term in the objective function is the Mahalanobis distance between transformed moving landmarks and fixed landmarks, and  $\Sigma_n$  is the covariance matrix of landmarks, quantifying the error of inexact matching of landmarks (as soft correspondences between landmarks).

Under geodesic shooting settings, the geodesic path of landmarks can be represented with an initial momentum space at the initial time point and an initial configuration of moving landmarks. Considering the conservation law of system momentum, the objective function becomes a function of the initial momentum. The optimization problem can be solved with typical gradient descent, and the optimal landmarks geodesic path is uniquely specified using the Hamiltonian principle with the optimal initial momentum and the moving landmarks configuration. The velocity vector field is assumed as Gaussian random fields and is interpolated over the entire domain. Finally, the displacement vector field  $D_i(x)$ ,  $x \in \Omega_S$  is obtained for each region  $R_i$  (i = 1, ..., m) with the solution of transport equation at t = 1. By interpolating the reverse velocity vector field from the reverse of the optimal landmarks geodesic path using the same scheme, we obtain a reverse displacement vector field  $D_i^{-1}(x)$ ,  $x \in \Omega_M$ . We use an available Matlab script for landmark-based diffeomorphic image registration to perform our landmark-guided non-linear regional registration (Sommer et al., 2011).

Inverse distance weighted interpolation of neighboring region-based displacement **composition** To estimate a single smooth global warping field that is applicable to all brain regions and can be applied to warp the whole brain all together at once, we propose the IDW interpolation method to combine all regional warping fields of the cortical regions. Regional displacement fields composition is illustrated in Figure 2.3. First, for region i, the global initial alignment A(x), regional initial alignment  $A'_i(x)$ , and non-linear regional displacement vector field  $D_i(x)$  are concatenated to a single regional displacement vector field  $T_i(x) = D_i(x)$  $A_i'(x) \circ A(x)$ . For interpolation between regions, morphology operations are performed to identify the region-to-region transition area in the brain. For example, for region i denoted as  $R_i$ , all other regions  $R_j$   $j=1,...,m,j\neq i$  are unioned  $(\bigcup_j R_j)$  then dilated  $(\bigcup_j R_j) \oplus SE$  to intersect with the dilated region i ( $R_i \oplus SE$ ) for finding the transition area of the region i that is  $[R_i \oplus SE] \cap [(\bigcup_j R_j) \oplus SE]$ , which leads to region i without transition area denoted as  $R_i^* =$  $R_i - [R_i \oplus SE] \cap [(\bigcup_j R_j) \oplus SE], j = 1, ..., m, j \neq i$ , where SE is the structural element. Here, we use a sphere with a radius of two voxels as our SE. The shortest distance from spatial location x to  $R_i^*$ , which is called  $d_i(x)$ , is used as the weighting factor in our IDW interpolation. Given subject space  $S(x), x \in \Omega_S \subset \mathbb{R}^3$  and MNI space  $M(x), x \in \Omega_M \subset \mathbb{R}^3$ , the global forward displacement vector field  $u_{SM}(x)$  is a normalized weighted sum of regional displacement vector fields,

$$u_{SM}(x) = \sum_{i=1}^{m} w_i(x) T_i(x)$$
 (2.2)

where  $w_i(x)$  is the normalized weight defined as follows:

$$w_{i}(x) = \begin{cases} 1, & x \in R_{i}^{*} \\ 0, & x \in R_{j}^{*}, j = 1, ..., m, j \neq i \\ \frac{q_{i}(x)}{\sum_{j=1}^{m} q_{j}(x)}, & otherwise \end{cases}$$
(2.3)

Here,  $q_i(x) = \frac{1}{d_i(x)^{\mu}}$  and  $\sum_{i=1}^m w_i(x) = 1$ . The first derivative of the interpolated global forward displacement vector field  $u_{SM}(x)$  is continuous with  $\mu > 1$  (Shepard, 1968), and in our method we set  $\mu = 4$ . The same IDW interpolation is also applied to the reverse regional displacement vector fields  $T_i^{-1}(x) = [A(x)]^{-1} \circ [A_i'(x)]^{-1} \circ D_i^{-1}(x)$  to obtain the global reverse displacement  $u_{MS}(x)$ . With the IDW interpolated displacement vector fields  $u_{SM}(x)$  and  $u_{MS}(x)$ , we obtain the corresponded deformation maps  $U_{SM}(x) = x + u_{SM}(x)$  and  $U_{MS}(x) = x + u_{MS}(x)$ . Unlike the regional deformation map, after the interpolation, these deformation maps are no longer diffeomorphic, and are not invertible. Next, we explain our method to overcome this shortcoming in our LG-RBSN method.

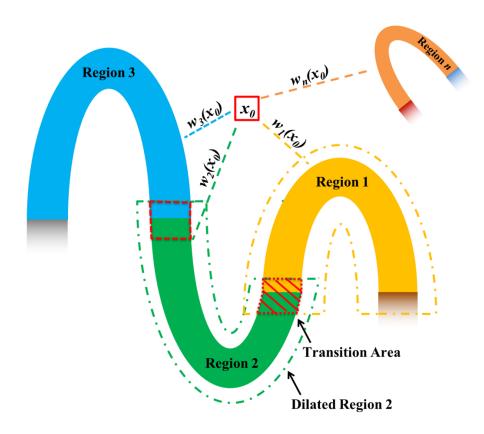


Figure 2.3: Combining adjacent regions' non-linear displacement fields using inverse distance weighted interpolation. For each location in the background and region-to-region transition area, the displacement is calculated as a normalized weighted sum of the displacement values in all regional warping fields at that location. The weight is based on the inverse of the closest distance between the location and the region.  $\mathbf{w}_i(\mathbf{x})$  is the normalized weight at location  $\mathbf{x}$  for region  $\mathbf{i}$ .

Bijectivity constraints with residual compensation and demons registration During spatial normalization the topology of a brain's anatomical structures should be preserved between healthy normal subjects, with connected neighboring morphological structures remain connected during deformation. Topology preservation is defined as a homeomorphic map that should be continuous, bijective, and inverse continuous. Topology preservation is a desired property for the estimated deformation field to perform a valid spatial normalization, because one-to-one and bijective correspondences of location structures between one brain and another are necessary

requirements for generating biologically meaningful warped brains. A simple and fast solution to embed topology preservation into the deformation field is through considering simultaneously forward and reverse maps with certain symmetric constraints. Existing topology preserving methods use different strategies to achieve this goal. For instance, Thirion used an iteration scheme to compensate for half of the residual of the reverse warped forward transformation equally to both of the forward and reverse transformations until the residual reaches identity transformation (Thirion, 1998). Ashburner et al. used a Bayesian framework with a symmetric prior, so that the probability distribution of the forward and reverse deformations is identical (Ashburner et al., 1999). Inverse consistency constraint was proposed in (Christensen and Johnson, 2001), which used a symmetric cost function. Avants et al. proposed a symmetric diffeomorphic registration model where forward and reverse deformations meet at the middle of the registration (Avants et al., 2008), whereas Kuang used a cycle-consistent design in a deep-learning network to learn forward and reverse deformations concurrently (Kuang, 2019).

In our solution, the deformation field for each region is diffeomorphic with strict bijective constraints, but the combined deformation using IDW interpolation will no longer guarantee bijectivity. For example, moving local gyrus images needed to be cut to prevent overlap during warping (Pitiot et al., 2003). To address invertibility a poly-affine method was proposed that composites local velocity vector fields associated with each local affine transformation, rather than compositing the displacement (Arsigny et al., 2005). However, this velocity vector field parametrization of the displacement is difficult for non-linear deformation in our case. Alternatively, our solution uses a residual compensation method to impose bijective property into the existing non-bijective global warping fields  $U_{SM}(x)$  and  $U_{MS}(x)$ , while using a demons

registration to match sub-cortical regions and the cerebral cortex mask. This prevents the mismatching of brain structures during residual compensation.

We use a residual compensation scheme to enforce bijectivity into both the direct forward deformation map  $U_{SM}(x) = x + u_{SM}(x), x \in \Omega_S$  from S to M and the reverse deformation map  $U_{MS}(x) = x + u_{MS}(x), x \in \Omega_M$  from M to S. At the same time, we use a demons registration method to match the brain's sub-cortical regions  $(SubR^i, i = 1, ..., n)$  and cerebral cortex mask (CC). We have initial direct deformation map  $U_{SM}^{(0)}(x) = x + u_{SM}^{(0)}(x)$  and initial reverse deformation map  $U_{MS}^{(0)}(x) = x + u_{MS}^{(0)}(x)$ . At each iteration t, we update both  $u_{SM}^{(t)}(x)$  and  $u_{MS}^{(t)}(x)$  according to following steps:

Compute residual displacement

$$r_{SM} = u_{SM}^{(t)} + u_{MS}^{(t)} \circ U_{SM}^{(t)} \tag{2.4}$$

$$r_{MS} = u_{MS}^{(t)} + u_{SM}^{(t)} \circ U_{MS}^{(t)} \tag{2.5}$$

Compute demons velocity for matching the brain's cerebral cortex mask

$$v_{SM}^{CC} = \frac{\left(CC_S - CC_M \circ U_{SM}^{(t)}\right) \nabla CC_S}{\|\nabla CC_S\|^2 + \alpha \left(CC_S - CC_M \circ U_{SM}^{(t)}\right)^2}$$
(2.6)

$$v_{MS}^{CC} = \frac{\left(CC_{M} - CC_{S} \circ U_{MS}^{(t)}\right) \nabla CC_{M}}{\|\nabla CC_{M}\|^{2} + \alpha \left(CC_{M} - CC_{S} \circ U_{MS}^{(t)}\right)^{2}}$$
(2.7)

Compute demons velocity for matching the brain's sub-cortical regions

$$v_{SM}^{SubR} = \sum_{i=1}^{n} \frac{\left(SubR_S^i - SubR_M^i \circ U_{SM}^{(t)}\right) \nabla SubR_S^i}{\left\|\nabla SubR_S^i\right\|^2 + \alpha \left(SubR_S^i - SubR_M^i \circ U_{SM}^{(t)}\right)^2}$$
(2.8)

$$v_{MS}^{SubR} = \sum_{i=1}^{n} \frac{\left(SubR_{M}^{i} - SubR_{S}^{i} \circ U_{MS}^{(t)}\right) \nabla SubR_{M}^{i}}{\left\|\nabla SubR_{M}^{i}\right\|^{2} + \alpha \left(SubR_{M}^{i} - SubR_{S}^{i} \circ U_{MS}^{(t)}\right)^{2}}$$
(2.9)

Update displacement fields

$$u_{SM}^{(t+1)} = u_{SM}^{(t)} - w_1 \cdot \beta \cdot r_{SM} - w_2 \cdot G(\sigma^2) * v_{SM}^{CC} - w_3 \cdot G(\sigma'^2) * v_{SM}^{SubR}$$
 (2.10)

$$u_{MS}^{(t+1)} = u_{MS}^{(t)} - w_1 \cdot \beta \cdot r_{MS} - w_2 \cdot G(\sigma^2) * v_{MS}^{CC} - w_3 \cdot G(\sigma'^2) * v_{MS}^{SubR}$$
 (2.11)

where,  $w_1$ ,  $w_2$ , and  $w_3$  are normalized weight with  $w_1 + w_2 + w_3 = 1$ ,  $G(\sigma^2)$  is a

Gaussian kernel with variance  $\sigma^2$ . We will show in the experiment section that by using this approach we can significantly reduce the number of non-positive Jacobian voxels after IDW interpolation.

**Subjects and data acquisitions** All research procedures were performed in accordance with relevant guidelines and regulations as approved by the Columbia University Institutional Review Board. Forty two subjects  $(27/15 \text{ young/older}, \text{age (mean} \pm \text{std}) = 25.11 \pm 3.24/66.93 \pm 3.71$  years) were scanned using a Siemens Prisma 3-Tesla MR scanner. T1-weighted images were acquired using a magnetization-prepared rapid gradient-echo (MPRAGE) (TR = 2300 ms; TE = 2.32 ms; flip angle =  $8^{\circ}$ , voxel size =  $1 \text{ mm} \times 1 \text{ mm} \times 1 \text{ mm}$ ; matrix size =  $256 \times 256$ , and 192 slices without gap). Task-based functional MRI were acquired using a T2\*-weighted multiband gradient-echo EPI (TR = 1 s; TE = 30 ms; flip angle =  $62^{\circ}$ , 64 slices without gap; slice thickness = 2 mm; 480 volumes; voxel size  $2 \text{ mm} \times 2 \text{ mm} \times 2 \text{ mm}$ , multiband factor = 4) pulse sequence. Another fMRI scan was acquired in the opposite phase encoding direction, which was used in this work solely for geometric distortion correction (GDC).

We employed an event-related fMRI experimental task design. The task consisted of two ongoing stimuli: 1) A maximum contrast flashing checkerboard (i.e., visual stimulus) presented on either the right or left side of the screen, and 2) An alternating tone (i.e., auditory stimulus) paradigm played on either the right or left ear. The two sensory stimuli were presented with random onsets and durations (uniform distribution, range = 1.0 - 5.0 sec). Overlaps between

visual and audio stimuli were allowed, however temporal overlapping of the bilateral presentation in the same modality was prohibited.

The data were collected in 2 runs; in the first run, subjects were instructed to attend to only one sensory stimulus (i.e., either visual or tonal) while ignoring the other. In the second run, they were instructed to attend the other sensory stimulus. Each scan consisted of 120 events: 60 events for visual and 60 for auditory stimulus. For each modality, 30 events on the right and 30 events on the left side spaced at inter-stimulus-intervals in the range of 1 - 17 sec were drawn from a uniform distribution. Control for attention was achieved by asking the subjects to press a button twice with their right/left index finger (depending on the lateralization of the attended stimulus) as soon as the attended stimulus terminated. These responses were recorded during the entire scans. Throughout the experiment, subjects were required to maintain their gaze on a minuscule fixation spot in the center of the screen, and were given feedback on any incorrect or out-of-time responses by changing the color of the fixation spot from green to red. Eye fixation was monitored by recording the eye position and movement at all times using an eye-tracking system. Subjects were trained multiple times outside of the scanner to learn and perform the task properly. All subjects learned the task correctly.

### 2.2.3 Results

In this section, we evaluate the performance of the proposed LG-RBSN technique using simulated and real data. We first generated simulated 2D images of folded ribbons that resemble the folding patterns of the human cerebral cortex. Our main goal in this simulation was to show how the top performing volumetric normalization methods could fail in registering such simple 2D scenarios. We then extended our validation to experiments with real MRI and fMRI data

targeting both primary visual and auditory regions. Our results were compared to a hybrid registration method (CVS) and a volumetric non-linear whole brain registration method (ANTS) (http://www.picsl.upenn.edu/ANTS/, RRID:SCR\_004757) that is considered the top performing non-linear registration algorithm (Klein et al., 2009).

Simulation of cortical gyrus registration To illustrate the problems associated with volumetric whole-brain registrations and to demonstrate the effectiveness of our proposed solution to overcome those problems, we simulate a single cortical gyrus registration experiment in 2D. To best simulate the real task of cortical regions registration we assumed that both moving and fixed gyri have a similar shape and width (4 pixels corresponding to 4 mm in most of the currently acquired T1-weighted MRI scans), but are comprised of 3 regions of different lengths across the gyrus, as shown in the first column of Figure 2.4 where the 3 cortical regions are color-coded for both images. The two rows in Figure 2.4 illustrate two simulated experiments with different initial positions: (a) with a relatively aligned initial position, and (b) with a misaligned initial position. Please note that even with initial affine registration of the whole brain, many cortical features (sulci and gyri) could still remain completely misaligned. Therefore, the simulated initial positions of alignment and mis-alignment between the moving and fixed images are very common in most spatial normalization or brain image registration scenarios. We used regional landmarks distributed at two sides of the ribbons in each region, as shown in the second column of Figure 2.4, to estimate a global bijective warping field using our method LG-RBSN. We also applied a modified ANTS non-linear registration pipeline from the half-C to full-C registration experiment to match the moving and fixed images (Avants et al., 2014).

In experiment (a), both LG-RBSN and ANTS resulted in a comparable overlap between the entire gyrus structure (ANTS: 99.11% versus LG-RBSN: 99.86%), shown as a binary mask in the third and last columns of Figure 2.4. However, such high correspondence for the entire gyrus, did not hold for the 3 comprising regions and the average regional DSC dropped from 99.91% for LG-RBSN to 86.39% for ANTS. This is because intensity-based volumetric registrations, such as ANTS, cannot discriminate adjacent cortical regions. Therefore, the underlying 3 regions will not necessarily be registered, as shown in the third column of Figure 2.4. Alternatively, LG-RBSN almost perfectly aligns the underlying regions, as shown in the last column of Figure 2.4.

In experiment (b), unlike LG-RBSN which generated a perfect correspondence, ANTS failed to generate an acceptable overlap even on the binary mask of the entire gyrus (ANTS: 82.49% versus LG-RBSN: 99.66%), as seen in third and last columns of Figure 2.4. As mentioned in the introduction, the ANTS failure is due to its vulnerability to the local minimum during optimization. The global affine initial alignment failed to provide a sufficient initial alignment of cortical regions, which is often the case in any non-linear registration problem.

Consequently, the underlying 3 regions drastically failed to correspond when using ANTS methods (ANTS: 42.60% versus LG-RBSN: 99.66%), as seen in the third and last columns of Figure 2.4. These results highlight the importance of detecting a true optimum point in any non-linear registration method.

Table 2.1: Dice similarity coefficient (DSC) between warped and fixed images of using ANTS and LG-RBSN in the simulation cases of (a) aligned and (b) mis-aligned initially.

Experiments	DSC between warped moving and fixed binary mask of all regions		Average DSC between warped moving and fixed image labels		Number of non-positive Jacobian pixels	
	ANTS	LG-RBSN	ANTS	LG-RBSN	ANTS	LG-RBSN
(a)	99.11%	99.86%	86.39%	99.91%	0	0
(b)	82.49%	99.66%	42.60%	99.66%	217	0

Jacobian matrix is commonly used to evaluate the diffeomorphic property of the warping field, as the local deformation is invertible and preserves the topology only at locations with positive Jacobian determinant. Table 2.1 also lists the number of voxels with non-positive Jacobians in each registration method. While we enforce all regional warping fields to be topology preserving by imposing bijectivity during the regional registration process, the combined global warping field is not guaranteed to be topology preserving due to the sharp transitions between some neighboring regions. To address this issue, we used residual compensation method to impose bijectivity to the obtained global warping field. To evaluate the performance of the utilized method, we used the number of voxels with non-positive Jacobian. As it seen in the Table 2.1, ANTS produces 217 pixels with non-positive Jacobian determinant in experiment (b), whereas all pixels show positive Jacobian determinant when LG-RBSN is being used for registration, emphasizing the performance of a residual compensation method in our LG-RBSN using simulated data.

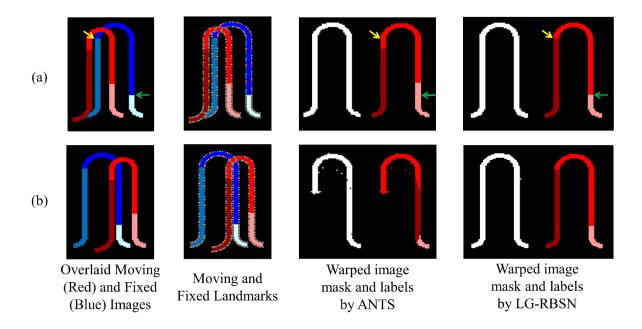


Figure 2.4: Comparison of ANTS and LG-RBSN registration results in cortical gyrus registration simulations with cases of moving and fixed images (a) aligned initially and (b) mis-aligned initially. In experiment (a), ANTS matched the whole gyrus mask perfectly but failed to accurately align the underlying 3 regions (yellow and green arrows mark the same location across images). In experiment (b), ANTS fell into a local minimum and failed to match even the binary mask of the entire gyrus. LG-RBSN matched the whole structure mask and regions perfectly in both experiments. ANTS: advanced normalization tools; LG-RBSN: landmark-guided region-based spatial normalization.

Evaluation using human brain structural images Using our LG-RBSN solution we estimated a global warping field between each subject, described in Section 2.2.2, and the MNI152 template utilizing regional WM and pial surfaces's vertices to extract corresponding landmarks. Figure 2.5 shows the estimated global warping field between one typical subject and the MNI152 using LG-RBSN solution. For comparison, we also used ANTS (deformation model: SyN; similarity: normalized mutual information; regularization: Gaussian smoothing) to perform the same registration. For qualitative evaluation of our method and ANTS, the two obtained global warping fields were applied to each subject's T1-weighted structural brain image, with results shown in Figure 2.6 for three selected subjects. LG-RBSN shows a clear improvement in

aligning brain cortical regions as highlighted by red dotted circles in Figure 2.6. The arrows in Figure 2.6 show how a sulcus can be generated by ANTS where the target image does not have such a structure (Subject 1), and how ANTS mismatched a gyrus of the subject to a sulcus in MNI152. Our method on the other hand properly matched the corresponding sulcus of the subject to the sulcus in MNI152 (Subject 2). This is because of performing optimization in 3D Euclidean space to find correspondence of the brain, which is often used in volumetric registration methods including ANTS. A small shift in the volume space can mismatch two functionally distinct locations of the brain, whereas our solution uses spherical registration to find the correspondence that directly matches brain folding patterns in each brain region, independently.

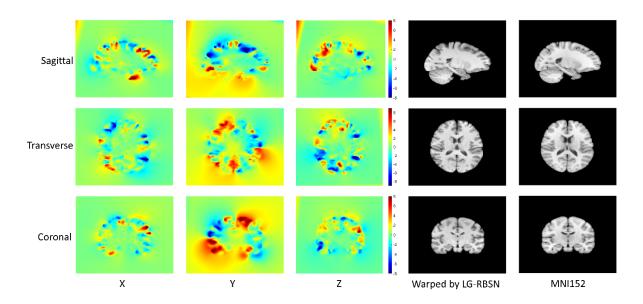


Figure 2.5: Visualization of LG-RBSN estimated global displacement vector field of one example subject. The X, Y, and Z denote the displacement in each direction with a unit of millimeter. This displacement vector field has a maximum displacement of 16.1 and a minimum displacement of -17.3, and is mostly within a range between -8 to 8. The visualization shows that our method is capable to work with large and localized displacements. LG-RBSN: landmark-guided region-based spatial normalization.

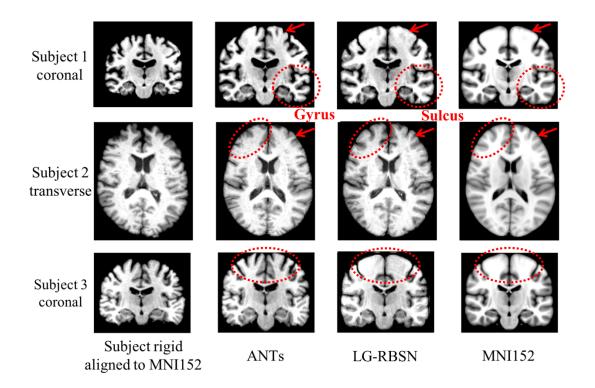


Figure 2.6: Spatial normalized brain qualification evaluation comparison between LG-RBSN and ANTS. The first and the last columns illustrate subjects' brain images rigid aligned (showing as moving images) to MNI152 brain images (as fixed images). The second and the third columns illustrate subjects' brain images after ANTS/LG-RBSN non-linear registration to MNI152 brain images. LG-RBSN shows clearly better performance compared to ANTS in red dotted circles highlighted areas. In subject 2, ANTS mismatched a gyrus of the subject's cerebral cortex to a sulcus in MNI152 space, whereas LG-RBSN matched the corresponding sulci properly. ANTS: advanced normalization tools; LG-RBSN: landmark-guided region-based spatial normalization.

For quantitative evaluation, we first evaluate the first two blocks of the algorithm (Section 2.2.2 in Figure 2.1), which generate the regional warping fields after the landmark matching and regional large deformation diffeomorphic registration. These regional warping fields can accurately match brain cortical regions with an averaged DSC of 0.8 (He and Razlighi, 2020), which validated the accuracy and efficiency of the initial FreeSurfer surface registration, landmark down-sampling, automatic landmark-matching and the regional diffeomorphic registration steps. Although, these regional warping fields can match cortical regions accurately,

but are limited to be only applicable to each region independently instead of the whole brain. As independently warping each region can cause overlaps and gaps between regions after the deformation, regional warping fields are not ideal for the application of brain structures and the functional brain activation patterns, which typically cover multiple brain regions. Thus, we introduced the IDW interpolation and bijectivity constraints steps to overcome these problems. Finally, for the quantitative evaluation of the global warping fields after all the steps of the algorithm, we used the global warping fields obtained above to warp each subject's FreeSurfer delineated regions, described in Section 2.2.2, onto MNI152 space (cortical regions include: banks of superior temporal sulcus, caudal anterior cingulate, caudal middle frontal, corpus callosum, cuneus, entorhinal, fusiform, inferior parietal, inferior temporal, isthmus cingulate, lateral occipital, lateral orbitofrontal, lingual, medial orbitofrontal, middle temporal, parahippocampal, paracentral, pars opercularis, pars orbitalis, pars triangularis, pericalcarine, postcentral, posterior cingulate, precentral, precuneus, rostral anterior cingulate, rostral middle frontal, superior frontal, superior parietal, superior temporal, supramarginal, frontal pole, temporal pole, transverse temporal and insula). As done previously (Balakrishnan et al., 2019; Klein et al., 2009; Yang et al., 2017), we have evaluated our registration accuracy using the DSC between the regional binary masks of the warped and corresponding target regions. We chose FreeSurfer because it has been shown to produce reliable parcellations of the cortex with a high accuracy compared to manual delineation of cortical regions (Desikan et al., 2006); However, any other consistent parcellation technique can be used for this underlying segmentation of the human brain. For comparison, we also applied affine registration (similarity as correlation ratio), ANTS (deformation model: SyN; similarity: normalized mutual information; regularization: Gaussian smoothing) and CVS (default settings). Figure 2.7 illustrates the distribution of the

DSC between corresponding regions for all cortical regions in FreeSurfer using boxplot for Affine (in red), ANTS (in black), CVS (in magenta) and LG-RBSN (in blue) categorized in six lobar brain segments. As shown in Figure 2.7, LG-RBSN significantly outperforms ANTS and CVS in all cortical regions reaching to highest DSC in the insula region with (DSC =  $0.9185 \pm$ 0.0116 (mean  $\pm$  std); ANTS: improved by 28.35% (p = 1.59e-31); CVS: improved by 20.84% (p = 6.24e-39)) and the lowest DSC in the pericalcarine region (DSC =  $0.7737 \pm 0.0379$  (mean  $\pm$ std); ANTS: improved by 140.88% (p = 1.76e-50); CVS: improved by 37.15% (p = 1.77e-43)). Compared to ANTS, as for the improvement in lobar segments of the brain, our results show that the highest improvement was achieved in the occipital lobe (DSC improved by 108.36%; p = 1.91e-52) with the least improvement in the insular lobe (DSC improved by 28.35%; p = 1.59e-31). Compared to CVS, the highest improvement was also achieved in the occipital lobe (DSC improved by 38.06%; p = 3.42e-53) with the least improvement also in the insular lobe (DSC improved by 20.84%; p = 6.24e-39). As shown in Figure 2.8, in total, using LG-RBSN has substantially improved the correspondence between cortical regions (DSC =  $0.8558 \pm 0.0080$ (mean  $\pm$  std)), which is significantly higher (DSC improved by 67.30%; p = 1.23e-50) than the results obtained by ANTS (DSC =  $0.5115 \pm 0.0641$ ; mean  $\pm$  std), and is also significantly higher (DSC improved by 29.80%; p = 1.95e-69) than the results obtained by CVS (DSC =  $0.6593 \pm$ 0.0197; mean ± std). Comparing the improvement of cortical regions correspondence in young and older subjects, LG-RBSN outperforms ANTS in both groups with a significantly higher improvement (p = 0.0042) in older subjects (DSC improved by 75.04%) than the improvement in young subjects (DSC improved by 63.25%).

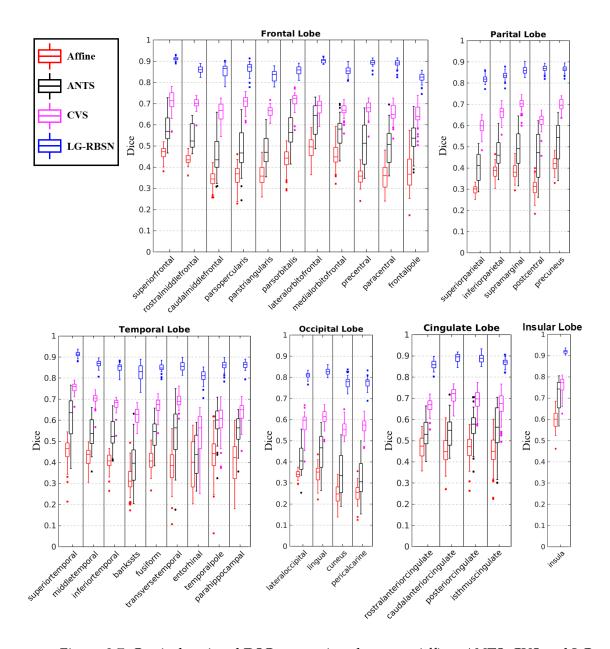


Figure 2.7: Cortical regional DSC comparison between Affine, ANTS, CVS and LG-RBSN in different brain lobes. LG-RBSN shows significantly higher DSC in matching brain cortical regions than ANTS and CVS. ANTS: advanced normalization tools; LG-RBSN: landmark-guided region-based spatial normalization; CVS: combined volumetric and surface registration; DSC: Dice similarity coefficient.

Next, we evaluated the effectiveness of the LG-RBSN for aligning the sub-cortical regions and cerebral WM in comparison with the results obtained by using ANTS and CVS

(segmented with FreeSurfer, sub-cortical regions include lateral ventricle, ventral DC, cerebellum white matter, cerebellum cortex, thalamus, caudate, putamen, pallidum, hippocampus, amygdala, third ventricle and brainstem). Figure 2.8 shows the results of this evaluation along with the evaluation of all cortical regions obtained above. As shown in Figure 2.8, our method significantly (p = 8.76e-03) outperformed ANTS in matching sub-cortical regions with a higher DSC value ( $0.8056 \pm 0.0267$ ; mean  $\pm$  std) compared to DSC values when using ANTS ( $0.7840 \pm 0.0446$ ; mean  $\pm$  std). And our method shows comparable performance with CVS in matching sub-cortical regions (p = 0.41). Furthermore, our method shows significantly improved DSC ( $0.9387 \pm 0.0046$ ; mean  $\pm$  std) of matching cerebral WM mask (ANTS: DSC improved by 25.56%, p = 9.33e-40; CVS: DSC improved by 9.00%, p = 5.48e-53), compared to the DSC of using ANTS ( $0.7477 \pm 0.0499$ ; mean  $\pm$  std) and compared to the DSC of using CVS ( $0.8613 \pm 0.0186$ ; mean  $\pm$  std).

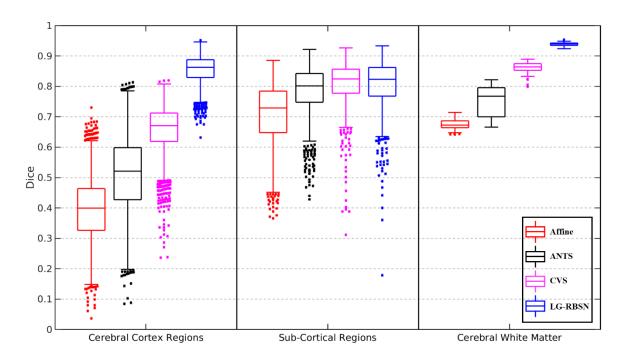


Figure 2.8: DSC comparison between Affine, ANTS, CVS and LG-RBSN. LG-RBSN shows significantly higher DSC in matching brain cortical regions, sub-cortical regions, and cerebral WM than ANTS. LG-RBSN shows significantly higher DSC in matching brain

cortical regions and cerebral WM than CVS. And LG-RBSN is more robust working with both young and older subjects compared to ANTS and CVS, as LG-RBSN shows less variance of DSC in matching brain cortical regions and cerebral WM. ANTS: advanced normalization tools; LG-RBSN: landmark-guided region-based spatial normalization; CVS: combined volumetric and surface registration; DSC: Dice similarity coefficient; WM: white matter.

Akin to the simulation section, the number of non-positive Jacobian voxels is used to quantify the bijectivity property of the global warping field, with a smaller number of nonpositive Jacobian voxels indicates better bijectivity property. To evaluate the last block of the algorithm (Figure 2.1), which is the bijectivity constrain step, we calculated the number of nonpositive Jacobian voxels along with iterations. Results are shown in Figure 2.9. The final global warping fields estimated by using our solution have  $1338.1 \pm 404.3$  (mean  $\pm$  std) non-positive Jacobian voxels for the forward warping field and  $1318.3 \pm 405.9$  (mean  $\pm$  std) voxels for the backward warping field, compared to ANTS with  $1483.2 \pm 2121.1$  (mean  $\pm$  std) for the forward warping field and  $1473.9 \pm 2239.1$  (mean  $\pm$  std) for the backward warping field. There is no significant difference between the number of non-positive Jacobian voxels between ANTS and LG-RBSN for both forward (t = 0.4354; p = 0.6644) and backward (t = 0.4433; p = 0.6587) warping fields. Compared with LG-RBSN and ANTS, CVS has a greater number of non-positive Jacobian voxels (7204.0  $\pm$  5591.2; mean  $\pm$  std) with worse bijectivity. However, for LG-RBSN, the number of non-positive Jacobian voxels can be lowered even to reach zero by using our residual compensation method, with a small cost in the accuracy. We will discuss the tradeoff between accuracy and the regularization in the discussion section.

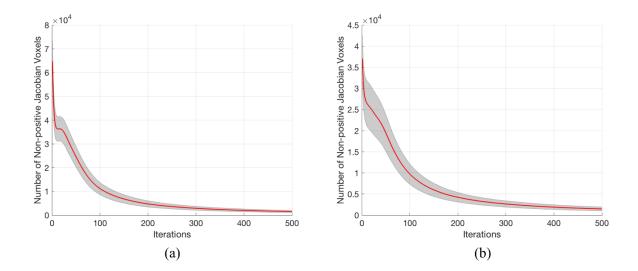


Figure 2.9: Number of non-positive Jacobian voxels decreases along bijectivity constrain iterations for (a) forward (subject to MNI152) (b) backward (MNI152 to subject) warping field. The red curve and the grey region represent the mean and the standard deviation.

Evaluation using human brain functional images We have shown in the previous section that LG-RBSN significantly improves the regional correspondence between warped and reference images. However, that does not necessarily imply that the enhancement will be directly transformed to functional imaging data. As we have shown previously in a preliminary study (Razlighi, 2016), the improvement in the structural overlap had significantly increased the statistics of the group-level brain activations in primary visual cortex, but it did not generalize to the group-level activations from the primary auditory cortex. We again applied LG-RBSN to the statistical parametric maps obtained from both an auditory and a visual fMRI experiment to generate group-level activation maps.

We have compared the obtained activation maps to those generated using Affine, ANTS and CVS, and to the anatomy of the primary visual and auditory cortices, where we expect to detect the true-positive activations. The preprocessing pipeline for the task-based fMRI data is

illustrated in Figure 2.10. Briefly, slice timing correction was applied to the raw fMRI timeseries to account for the difference in the acquisition delay between slices (Parker et al., 2017; Parker and Razlighi, 2019a). At the same time, motion parameters were estimated on raw fMRI scans using rigid-body registrations performed on all the volumes in reference to the first volume. Additionally, the first volumes were extracted from another fMRI scans with opposite phase encoding directions to estimate the geometric distortion correction field using a susceptibilityinduced distortions correction technique called topup (Andersson et al., 2003) provided in FSL software package (https://fsl.fmrib.ox.ac.uk/fsl, RRID:SCR 002823) (S. M. Smith et al., 2004). Then, the estimated motion parameters and geometric distortion field were combined and applied to the slice timing corrected fMRI time-series to get the distortion and motion-corrected fMRI time-series. First level general linear modeling was performed independently on each voxel using multiple regression with four variables of interest (stimuli timing convolved with canonical Double-Gamma hemodynamic response function) resulting to 4 different statistical parametric maps which will be warped onto a standard space to be able to perform group-level statistical analysis. Each subject's global registration warping field estimated in the previous experiment was concatenated with the within-subject functional to structural rigid-body transformation, and used to project brain auditory/visual activation statistical maps of that individual into MNI152 space for group-level analysis. Group-level analysis was done by simple regression where a voxel was deemed active if its averaged point-estimates were significantly different from zero.

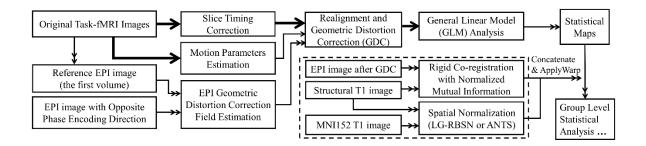


Figure 2.10: The processing pipeline for task-based fMRI data. The thick arrows show the transfer of 4D fMRI data, the double thin arrow shows the transfer of the 3D data, and the thin arrow shows the transfer of the parameters. ANTS: advanced normalization tools; LG-RBSN: landmark-guided region-based spatial normalization; EPI: echo planar imaging.

We first compared the actual statistics of the group-level analysis results when LG-RBSN was used as the spatial normalization versus the results obtained with using Affine, ANTS and CVS. The statistics were quantified as the point estimates ( $\beta$  values) of the 1000 activated voxels with highest z-statistics in the brain's left lateral occipital cortex for stimulating right visual hemifield and vice versa. Figure 2.11 illustrates the distribution of the point-estimates in the top 1000 activated voxels using boxplots (Left: for stimulating left visual hemifield; Right: for stimulating right visual hemifield). As seen in Figure 2.11, the mean point estimates of group-level brain activation using our method (Left:  $\beta = 280.20 \pm 40.96$  Right:  $\beta = 315.33 \pm 57.34$ ) is significantly higher (Left:  $\beta = 30.08$  p = 0, Right:  $\beta = 26.32$  p = 0) than that obtained by ANTS (Left:  $\beta = 229.24 \pm 34.54$ , Right:  $\beta = 255.76 \pm 42.84$ ), and is also significantly higher than that obtained by CVS for the left visual hemifield stimuli ( $\beta = 261.90 \pm 35.70$ ; p = 8.62e-26) but is not significantly higher for the right hemifield stimuli ( $\beta = 309.98 \pm 64.71$ ; p = 5.06e-2).

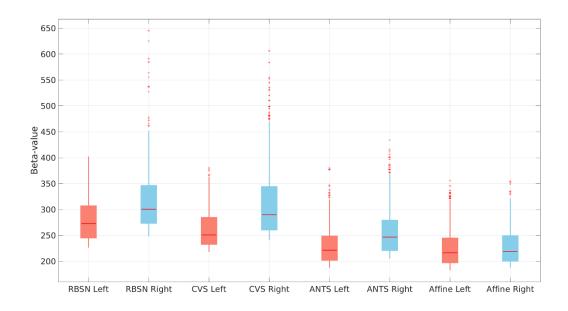


Figure 2.11: Distribution of the point estimates for visual task-based fMRI group level visual activation in brain contralateral occipital lobe using different spatial normalization methods (Left: for stimulating left visual hemifield; Right: for stimulating right visual hemifield). ANTS: advanced normalization tools; LG-RBSN: landmark-guided region-based spatial normalization; CVS: combined volumetric and surface registration.

For auditory stimulation we used combination of two FreeSurfer regions (transverse temporal gyrus and superior temporal gyrus) to generate a binary mask for the primary auditory cortex. Figure 2.12 illustrates the distribution of the point estimates from the 1000 voxels with highest significance level within the binary mask using boxplots and also shows the comparison between the point estimates obtained by our LG-RBSN solution and the ones obtained by using Affine, ANTS and CVS (Left: for stimulating left ear; Right: for stimulating right ear). As seen in this figure, the mean point estimates of the group level brain activation using our method (Left:  $\beta = 255.22 \pm 48.84$ , Right:  $\beta = 236.28 \pm 33.02$ ) is significantly higher (Left: t = 12.89, p = 1.40e-36; Right t = 16.68, p = 0) than that obtained by ANTS (Left:  $\beta = 230.46 \pm 36.12$ , Right:  $\beta = 211.48 \pm 33.47$ ). Compared to CVS, the mean point estimates using LG-RBSN is slightly higher than that obtained by CVS for the left ear stimuli ( $\beta = 253.56 \pm 45.97$ ; p = 0.43) but is

significantly lower for the right ear stimuli ( $\beta$  = 253.58 ± 39.08; p = 5.79e-26). As compared to ANTS, the group level statistics results in both visual and auditory task-based fMRI indicate that the magnitude of the fMRI signal will significantly increase if we use a more accurate spatial normalization technique (either CVS or LG-RBSN). When comparing CVS and LG-RBSN, results indicate that the improvement in the regional correspondence would improve the group-level activation statistics in visual and left ear auditory stimuli evoked activation, but the regional correspondence improvement did not transform to the increase in the group-level activation statistics of right ear auditory stimuli evoked activation. This might be due to the misalignment between the brain morphology and the underlying functional architecture, which will be discussed later in the discussion section.

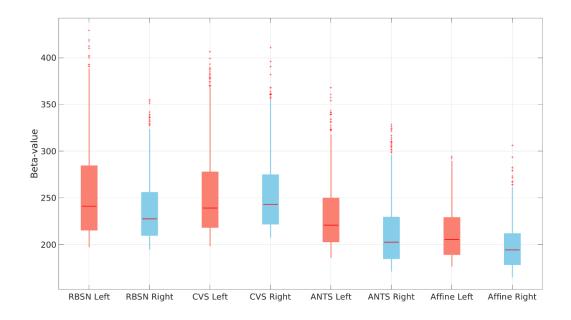


Figure 2.12: Beta values of tonal task fMRI group level auditory activation in contralateral transverse temporal cortex and superior temporal cortex using different spatial normalization methods (Left: for stimulating left ear; Right: for stimulating right ear). ANTS: advanced normalization tools; LG-RBSN: landmark-guided region-based spatial normalization; CVS: combined volumetric and surface registration.

Improving the group-level statistics in our fMRI experiments shows that the proposed spatial normalization technique increases the statistical power to detect smaller effects that may not be detectable with the conventional methods such as ANTS. Still, the method does not guarantee that the false-positive rate will not increase as well, which is often the case in many advanced developments for fMRI processing. To address this problem, we use receiver operating characteristic (ROC) curves which associate the cost of improvement in the true-positive rate (sensitivity) to the false-positive rate (1-specificity) at different threshold levels for detecting an effect. However, using ROC curve for evaluating any fMRI experiment is a challenging task due to the lack of gold standard measurement. In this study, we use the masks of the primary visual cortex (lateral occipital) and auditory cortex (transverse temporal gyrus and superior temporal gyrus), given by FreeSurfer, as the regions that we expect to see activated voxels in and any detection of activated voxels outside these masks can be considered as false-positive. Therefore, true-positive rate is the number of activated voxels divided by the total number of voxels inside the region, and false-positive rate is the number of activated voxels in the vicinity of the regional masks (obtained by dilating the same regional masks) divided by the total number of voxels in the dilated regions. By changing the threshold for significance (t-statistics ranging from 0 to 15), we plot the curve illustrating the association between these two rates. The area under the curve (AUC) of the ROC is often used as the main performance metric for quantitative comparison.

Figure 2.13 illustrates the ROC curves obtained for the two visual stimuli (left plot: for stimulating left visual hemifield; right plot: for stimulating right visual hemifield) when LG-RBSN were used (blue curve) versus Affine (black curve), ANTS (green curve), and CVS (red curve). Our LG-RBSN method shows an AUC equal to 0.7124/0.7180 for left/right hemifield visual stimulation which demonstrates about 10.24%/8.23% improvement in comparison to the

AUC obtained from ANTS ROC (0.6462/0.6634 for left/right visual hemifield stimulation). And LG-RBSN also outperforms CVS (0.7022/0.7086 for left/right hemifield visual stimulation). This result indicates that such improvement in the sensitivity of our proposed method is not at the expense of an increased false-positive rate.

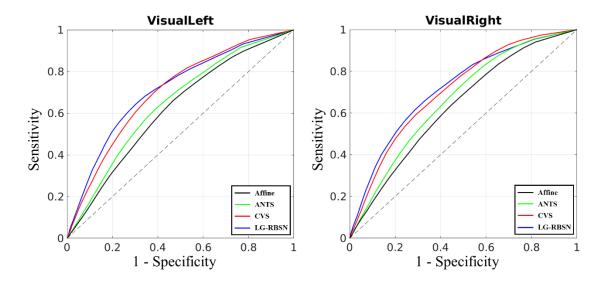


Figure 2.13: ROC curve evaluating spatial normalization methods with visual task-based fMRI group level t-statistics activation map compared to FreeSurfer lateral-occipital region (Left: for stimulating left visual hemifield; Right: for stimulating right visual hemifield). ANTS: advanced normalization tools; LG-RBSN: landmark-guided region-based spatial normalization; CVS: combined volumetric and surface registration; ROC: receiver operating characteristic.

Figure 2.14 illustrates the ROC curves obtained for the two auditory stimuli (left plot: for stimulating left ear; right plot: for stimulating right ear) when LG-RBSN was used (blue curve) versus Affine (black curve), ANTS (green curve), and CVS (red curve). LG-RBSN shows an AUC equal to 0.8276/0.8490 for left/right ear auditory stimulation which demonstrates about 1.47%/5.10% improvement in comparison to the AUC obtained from ANTS ROC (0.8156/0.8078 for left/right ear auditory stimulation). As compared to CVS (0.8238/0.8513 for left/right ear auditory stimulation), LG-RBSN shows a slightly higher (0.46%) AUC for the left

ear auditory stimulation, but a slightly lower (-0.27%) AUC for the right ear auditory stimulation. As compared to ANTS, the results again indicates that such improvement in the sensitivity of our proposed method is not accompanied by an increase in the false-positive rate. But similar to the previous results on the point estimates, when comparing LG-RBSN and CVS, regional correspondence improvement did not transform to the increase in the sensitivity and specificity for the group-level activation statistics for the right ear auditory stimuli. As discussed previously, one reason might be the misalignment between the brain morphology and the underlying functional architecture. Due to the lack of gold standard, another explanation might be the assumption we made when defining the primary auditory cortex, where we treated as the expected location of true-positive activations.

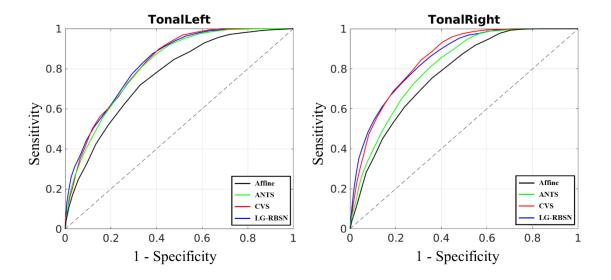


Figure 2.14: ROC curve evaluating spatial normalization methods with auditory task-fMRI group level T-statistics activation map compared to FreeSurfer segmented neuroanatomical brain contralateral primary auditory mask (Left: for stimulating left ear; Right: for stimulating right ear). ANTS: advanced normalization tools; LG-RBSN: landmark-guided region-based spatial normalization; CVS: combined volumetric and surface registration; ROC: receiver operating characteristic.

Taken together, results in Figure 2.13 and Figure 2.14 highlight the superiority of the proposed LG-RBSN solution in detecting small effects that were not detectable using conventional methods such as ANTS, without increasing the false-positive rate, which is the ultimate goal in any advancement in method development for fMRI processing pipeline. Further functional evaluation with fMRI data between LG-RBSN and CVS might be needed with more detailed brain parcellations such as HCP MMP (Glasser et al., 2016), or using other task stimuli with more specific activation patterns such as face stimuli and the fusiform face area.

Coding and execution time Most of the implementation in this work is done with Matlab R2017b. We have shared the code for LG-RBSN solution on our laboratory website (https://qnlab.weill.cornell.edu/research/pre-processing-fmri-data) as well as our laboratory github repository page (https://github.com/QuantitativeNeuroimagingLaboratory). The current implementation of the LG-RBSN takes an average of around 18 hours to be performed on each region. However, since the registration of each region is done independently, they all can be done in parallel using cluster of high-performance computing with around 100 number of cores. Using the cluster makes the total execution time to be around 75 hours for each subject's brain registration. However, applying the obtained warping field takes no more time than applying other conventional spatial normalization methods.

#### 2.2.4 Discussion

We presented a novel region-based volumetric spatial normalization solution for human structural and functional brain image processing and statistical analysis. Compared to typical volume-based spatial normalization methods that use intensity-based similarity measurements,

our solution uses landmark guidance which specifies a concrete spatial correspondence in the volumetric space based on matching of the brain cortical folding patterns. To address the local minimum problem in optimization steps in most of the whole brain volume- or surface-based, or hybrid image registrations, we propose to independently estimate a diffeomorphic warping field for each cortical region. Locally-affine and poly-affine registration methods have been previously used in medical image registration (Arsigny et al., 2005; Porras et al., 2018). However, here we propose a novel region-based nonlinear registration approach and present the first study in combing the regional non-linear warping fields. To generate a single smooth global warping field with a smooth transition across adjacent regions, we propose to use IDW interpolation. Compared to other symmetric registration algorithms (Ashburner et al., 1999; Avants et al., 2008; Christensen and Johnson, 2001), which regularize the bijectivity property during registration, our proposed residual compensation method is applicable to any given nontopology-preserving warping fields, as long as both forward and backward warpings are available.

Compared to typical surface-based spatial normalization methods that only warp brain cortical surface, our solution extended surface-based methods to estimate a volumetric warping field. This method is considered more robust than typical surface-based spatial normalization methods, since fMRI brain activations are captured originally in the 3D Euclidean space and thus avoiding the projection of the volumetric data onto the cortical surface. Furthermore, surface-based methods are more susceptible to the inaccuracies that often occur during reconstructions of cortical surface due to geometric distortion, especially in high-field and multiband acquisitions. While any inaccuracy in the surface reconstruction will cause surface-based method to include regions from outside of the brain or the white matter, our solution computes volumetric

deformation mappings that are applied to all gray-matter, white-matter, and other brain regions, thus preventing loss of fMRI data due to inaccurate surface extraction. In future work, we will aim at a quantitative evaluation between our volume-based registration method and other surface-based registration methods (e.g. FreeSurfer), however a direct comparison is challenging as the group activation results are in different space (Tucholka et al., 2012). The comparison between surface-based and volume-based spatial normalization is beyond the scope of this study.

Evaluating spatial normalization methods has received considerable attention in recent years, which are typically evaluated by measuring the overlap between the warped anatomical regions and the counterpart regions in the reference brain. Klein et al. evaluated 14 methods with four MRI dataset of healthy and young subjects, and showed that these methods perform well in warping the sub-cortical regions (average DSC above 80%), but even the top performing method ANTS (Avants et al., 2008) and recently-developed deep learning methods generally have poor performance in warping cortical regions (average DSC between 60% and 70%) (Balakrishnan et al., 2019; Klein et al., 2009; Yang et al., 2017). It is because almost all of the widely used brain image registration techniques that work in the 3D Euclidean space, whether volume-based, or surface and volume hybrid methods, are based on solving the optimization problem of matching the whole brain at once and suffer from the local minimum problem, resulting in poor registration of brain cortical regions. Recent advances in intensity-based brain image registration methods used both T1 and T2 weighted images to guide inter-subject registration (Simonovsky et al., 2016). This multi-modal approach will help the delineation and matching of grey matter boundaries. However, intensity-based methods still have the issue of the homogeneous intensities between cortical regions within the cortical grey matter, which hinders the matching of corresponding cortical regions between subjects. Furthermore, many existing retrospective

datasets have limited access to scans from other modalities (only T1-weighted structural scans). Spatial normalization is even more challenging to studies of populations with severe brain morphology changes. For example, caution should be taken when studying aging population, as it has been shown that brain morphology changes along normal aging with grey matter volume reduction (Good et al., 2001), especially in prefrontal regions (Tisserand and Jolles, 2003) and in the medial temporal lobe (Jack et al., 1997). In these cases, inaccurate spatial normalization can transfer population-related residuals to the normalized group-level brain activation, which will no longer be a valid representation of the population. Hence, any conclusion drawn with this biased representation will heavily be confounded by the residuals. For example, the age-related atrophy in the brain of the older participants has shown to further deteriorate the accuracy of the spatial normalization, and subsequently interpreted as age-related attenuation of BOLD response amplitude (Liu et al., 2017).

We have evaluated our proposed solution using three different experiments: 1) Using simulated 2D images of a single gyrus we demonstrated that our solution not only aligns cortical folding patterns, but also keeps an accurate correspondence in its internal regional structures. Furthermore, we showed using the simulated images that our solution is more robust to the local minimum problem compared to a top performing volumetric registration method ANTS. The simulated experiments highlighted the issues with intensity-based whole-brain registration methods (e.g. ANTS) even in a simplified 2D scenario. Whereas, our proposed LG-RBSN solution addressed these challenges by leveraging the features of using landmark guidance and region-based registration. However, it should be noted that these simulated experiments cannot substitute the complexities in the registration of real brain images, as human brains have highly convoluted folding patterns and large inter-subject shape variability. Thus, in this study, we also

validated our method with real structural and functional human brain MRI data. 2) Using structural images of human brains, we showed that our solution increases the correspondence between cortical regions, sub-cortical regions, and cerebral white matter in comparison to the existing top performing volumetric registration method ANTS and a hybrid registration method CVS. In Figure 2.8, all methods performed better in the registration of sub-cortical regions than cortical regions, which is expected as sub-cortical regions are bounded by the white matter and have less complex shapes, rendering an easier case for most of the spatial normalization methods. However, only the method proposed in this study performed well in cortical regions, which have highly convoluted patterns of sulci and gyri, showing a compelling case for the proposed LG-RBSN method. Our solution also showed that the number of non-positive Jacobian voxels can be decreases with the utilized residual compensation iterations to the level of ANTS, and is much lower than that of CVS. 3) Using functional images of human brains, we first showed that improving the correspondence between regional structure not only increases the statistical power in detecting smaller activations, but also keeps the false-positive rate low. This was measured by AUC of the ROC curves, indicating about 6.3% improvement compared to ANTS, and about 1.1% improvement compared to CVS. However, the improvement in the regional correspondence did not transform to the increase in the sensitivity and specificity in the group level statistics when comparing LG-RBSN and CVS for the right ear auditory stimuli condition. Together, our findings suggest that LG-RBSN solution is a more accurate and reliable substitute for conventional spatial normalization techniques commonly used in the field.

We have preliminarily used region-based registration methods to align MRI brain images with optimization running separately for each individual brain regional mask instead of the whole brain (Razlighi, 2016). This region-based spatial normalization method resulted in a 44%

improvement of the correspondence between cortical regions (DSC around 0.75) in comparison to the top performing non-linear whole brain registration (ANTS). However, the inter-subject variability of cortical regions was still causing the optimization process to fall into local minimums especially in regions with severe age-related atrophy and deformations, like temporal lobe regions. Additionally, in our previous method, separately warping each region individually with its own warping field can introduce gaps and overlaps in-between regions. Edwards et al. has also compartmentalized the medical images of the human body into two separate segments in which the rigid and deformable structures of the body were registered independently to their counterparts, transformed separately, and then combined (Edwards et al., 1995). This method improved registration accuracy but was limited for the resultant discontinuity in structural boundaries. This limitation was addressed in a following paper (Little et al., 1997) using a single global smooth transformation. The global transformation was composited using a modified radial basis function and the inverse distance interpolation (Shepard, 1968) based on rigid structures within the image. Another similar method used only affine transformations for different segments of the brain (Pitiot et al., 2003), where, each gyrus locally registered to its counterpart using affine transformation for 2D registration of myelin-stained histological sections of the human brain. Local registration methods interpolate locally linear transformation fields, whereas our method not only uses topographical landmarks to guide the non-linear registration, but also deals with the regional transition by an IDW interpolation method with enforced bijectivity to ensure both regional and final global warping field are diffeomorphic and topology preserving deformations.

The tradeoff between regional correspondence and bijectivity regularization (for topology preserving deformation) can be tuned to find a balance between the matching of brain structures

and number of voxels violating the diffeomorphism. In LG-RBSN, by tuning the weights between matching and regularization, the number of non-positive Jacobian voxels can be lowered even to reach zero, however, this will cause a decrease in the correspondence between the cortical regions (the average DSC of cortical region will drop to around 80%). In our experiments, we choose to tolerate 1300 number of voxels (0.0077% of total number of voxels) with non-positive Jacobian determinant, to achieve about DSC = 86% correspondence between cortical regions, which was the optimal setting in this work, however other applications may require further adjustment to obtain their optimal ranges. In addition, in the IDW interpolation method we set  $\mu=4$ , which produced acceptable results in our experiments. However, a thorough optimization is required in the future to obtain the optimal value for the  $\mu$  in each registration application.

In our experiments and results section, the reported DSC for ANTS in this work may seem lower than the ones reported in the literature (Klein et al., 2009). This is because; a) healthy elderly adults comprise more than one-third of our sample and generally show excessive brain atrophy in comparison to younger subjects, particularly in the prefrontal and temporal cortical regions (Jack et al., 1997; Tisserand and Jolles, 2003). It has been shown that brain atrophy can significantly alter the effectiveness of brain registration accuracy (Avants et al., 2008). b) we have evaluated a subject-to-template registration while most of the evaluation in the existing evaluation are done with subject-to-subject registration (Klein et al., 2009). This will be even more problematic when we have older population in our sample group. In future studies, cerebral cortex regions overlap can be further improved with a custom group average template specifically designed for use with LG-RBSN.

In our experiments, we evaluated our method with both structural (T1-weighted structural scan) and functional data (visual and auditory task-based fMRI scans) from human brain, and we detected statistically significant improvement and stronger brain activations by using our proposed method. This improvement might reduce the required number of subjects to detect the group effects in functional imaging studies. However, future studies are needed to evaluate the robustness of our method by using a large number of subjects. Furthermore, in this study, the samples do not include subjects in the middle-age group. We highlighted the challenges of dealing with subjects in the old group by using a conventional method, and the superior performance of using our method. We expect that our method will also work well with subjects from the middle-age group, as these subjects have been shown to have a less age-related morphological alterations in brain structures compared to subjects in the old group (Razlighi et al., 2017). Future studies are needed to test our method on subjects in the middle-age group. And it is an important topic to investigate the age-related brain variability, however, we feel it is out of the scope of this study, as the spatial normalization methods focused on quantifying the intersubject brain variability. Our proposed method utilizes the morphometric procedures from FreeSurfer, which have been demonstrated to be insensitive to the heterogeneity in the data acquired from different scanner platforms (Han et al., 2006; Han and Fischl, 2007; Reuter et al., 2012). Therefore, we feel confident that our method will have a comparable performance dealing with brain images acquired from different scanners. However, future work is warranted to test the reliability of our proposed spatial normalization method with multi-scanner imaging data.

Finally, it would be interesting to evaluate the performance of the LG-RBSN solution for multivariate techniques such as group independent component analysis (ICA), or partial least-squares (PLS). The difference between the evaluation of the multivariate and univariate (voxel-

based) methods is that multivariate techniques often require warping the actual 4D fMRI data, whereas univariate analysis can be performed after the first-level statistical analysis. Therefore, one might expect to obtain a different performance in applying LG-RBSN to the multivariate data. Furthermore, we only evaluated the LG-RBSN technique on structural and functional MRI scans. It would be interesting to assess the effectiveness of this method on other MRI modalities such as diffusion weighted imaging, arterial spine labeling, and susceptibility weighted imaging amongst others. We also expect that our proposed spatial normalization method could be extended to enhance spatial normalization accuracy in the other imaging modalities such as positron emission tomography and computed tomography.

# 2.3 Negative BOLD Responses in the Human Visual Cortex

## 2.3.1 Introduction

Functional magnetic resonance imaging is the most commonly used modality for *in-vivo*, and non-invasive functional mapping of the human brain based on endogenous BOLD contrast (Ogawa et al., 1992). A focal task/stimulus-evoked neuronal activation usually generates a localized change in the MR signal of the activated area relative to its pre-stimulus period. The shape and properties of this change in MR signal, henceforth referred to as positive BOLD response, have been thoroughly investigated and reported as the hemodynamic response function (HRF) of the BOLD signal (Mandeville and Marota, 1999; Menon et al., 1995). In addition to the PBR, fMRI responses in the opposite direction, which are often referred to as negative BOLD response (NBR), have been observed in regions adjacent and remote to the PBR regions (Shmuel et al., 2002; A. T. Smith et al., 2004).

While much progress has been made towards characterizing the shape of PBRs hemodynamics and their underlying mechanisms, the properties of NBRs and their corresponding underlying mechanisms are yet to be fully characterized (Liu et al., 2011; Logothetis, 2008). Numerous studies have detected NBR during stimulation of sensory and motor cortices from regions in the vicinity of the PBR (Shmuel et al., 2006, 2002) and in ipsilateral regions relative to a unilateral stimulus (Kastrup et al., 2008; Mullinger et al., 2014; Shmuel et al., 2003; S. M. Smith et al., 2004; Stefanovic et al., 2004). However, there is no consensus on the origins and properties of these two types of NBRs. Several hypotheses have been made with regard to the mechanisms contributing to NBRs: (1) Decreases in neuronal activity due to local neuronal inhibition or decreases in afferent neuronal input (Shmuel et al., 2006, 2002; Smith et al., 2000; S. M. Smith et al., 2004; Stefanovic et al., 2004); (2) Passive reduction of cerebral blood flow (CBF) in regions adjacent to PBR, due to shared upstream arterial supply (blood steal), independent of changes in neuronal activity and/or neural control signals (Harel et al., 2002; Hu and Huang, 2015; Shmuel et al., 2002); (3) Active reduction of CBF (blood flow control) due to neural control signals that cause contraction of smooth muscles surrounding arteries and arterioles supplying the NBR regions, to ensure adequate supply to the areas of demand (A. T. Smith et al., 2004), and (4) Venous backpressure due to limited drainage capacity of venous compartments in response to massive increase in CBF to the PBR region (Boas et al., 2008; Goense et al., 2012; Shmuel et al., 2006). However, none of these mechanisms has been proposed and/or evaluated considering concurrent observation of NBRs in proximity to PBR and in the opposite hemisphere during unilateral sensory stimulation. While some studies have used the observed NBR in the ipsilateral hemisphere as evidence to invalidate the blood steal hypothesis (mechanism 2), since the two hemispheres have distinct, and quasiindependent arterial supply (Mullinger et al., 2014; Shmuel et al., 2003; A. T. Smith et al., 2004), we postulate that inducing concurrent NBR in two opposite hemispheres has not been used to its full capacity to provide evidence in support or against of the existing hypotheses.

Since both contralateral NBR (cNBR) from the vicinity of PBR, and ipsilateral NBR (iNBR) from the opposite hemisphere, can be simultaneously induced and detected during unilateral visual hemi-field stimulation, it is natural to ask whether a common or distinct neural/vascular mechanism/s underlies the cNBR and iNBR? Furthermore, if both NBRs are generated through a common mechanism, then it is important to know whether PBR is the underlying force for their simultaneous generation. The answer to these questions is of paramount importance because they could provide strong evidence for remote but active blood flow control (mechanism 3) and against two of the aforementioned hypotheses (blood steal, and venous backpressure). It essentially determines whether the two NBRs are regulated locally and independently within each hemisphere's visual cortex, through major inter-hemispheric callosal pathway connecting homologues regions, through the reported inter-hemispheric functional connectivity in visual cortex, or remotely through an intervening distal region with access to both hemispheres. By investigating the temporal and spatial relationships between these two types of NBRs and comparing those with the relationship of each NBR with PBR, we aim to provide evidence for distal regulation and against local regulatory mechanisms, such as inter-hemispheric synchrony through major callosal pathway, or functional connectivity.

We start by investigating the linearity of the two NBRs in respect to stimulus duration since it is the pre-requisite for most of the statistical analysis conducted in fMRI. Even the most basic HRF extraction techniques using deconvolution (i.e. finite impulse response (FIR)) is based on the linearity assumption. Linearity of NBR with respect to stimulus duration, to our

knowledge, has not been shown previously and without its validation our extracted HRFs for NBR and brain statistical maps for NBRs will not be valid. Once linearity was established, we extracted the HRFs of both NBRs to investigate any difference between their magnitudes and dynamics and compare it with the HRF of the PBR. Furthermore, we investigated the association between subject-wise expression of the two NBRs and compared it with the relationship of each NBR with PBR. Our results indicate that the HRFs of two NBRs obtained from two opposite hemispheres have similar amplitudes and dynamics whereas they both are significantly different in comparison to the HRF of the PBR. Furthermore, the subject-wise expression of the two NBRs are significantly more correlated with each other than each one with that of PBR. The high inter-hemispheric synchrony in the magnitudes, dynamics and inter-subject variabilities of the two NBRs motivates the examination of the role of interhemispheric callosal pathway, or functional connectivity for facilitating such synchrony. Thus, we first computed interhemispheric spatial similarities of the regions showing NBRs and compared it to the interhemispheric spatial similarity of the cNBR with PBR. Then, to rule out the effect of interhemispheric functional connectivity in inducing coherent NBRs in two hemispheres, we computed the inter-hemispheric functional connectivity of the regions showing NBRs and compared it with the inter-hemispheric functional connectivity of the cNBR with PBR. Neither interhemispheric callosal pathway nor interhemispheric functional connectivity explained the observed synchrony between two NBRs, providing evidence for remote blood flow control.

Finally, we studied the performance correlates of the two NBRs and whether the two NBRs were modulated by attention. These experiments are motivated with our recent findings that the NBRs detected from DMN regions are attention-specific and are correlated with performance (Parker and Razlighi, 2019b). Any difference in the attention and/or performance-

association highlights the possibility of having a separate underlying neural and/or vascular mechanism. Our findings suggest that the cNBR and iNBR share a common neural and/or vascular mechanism which is different not only from the ones underlying PBR, but also from the mechanism underlying NBR detected from the DMN, and probably regulated by a distant brain structure that projects to the two hemispheres and actively controls blood flow distribution of the cerebral cortex.

### 2.3.2 Methods

**Participants** Twenty-seven healthy young subjects (mean age  $\pm$  SD = 25.11  $\pm$  3.24, female/male = 20/7, all right-handed) were recruited using random market mailing approach within 50-mile radius of Columbia University Irving Medical Center and were compensated for their time spent partaking in this study. All subjects gave their informed written consent prior to the scanning sessions. The experimental design of our study and the recruitment process were approved by Columbia University institutional review board.

**fMRI Experimental Design** We employed an event-related fMRI experimental task design to effectively examine the timing and the shape of the extracted HRFs. The task consisted of two ongoing stimuli: 1) An almost square checkerboard with alternating luminance between 25% and 44% of maximum luminance, spatial frequency of 1.17 cycle per degree, and contrast reversal rate (temporal frequency) of 6 Hz was presented to the right or left of the screen (with 50% of maximum luminance) approximately between 2.29° and 9.14° angle, as shown in Figure 2.15b; and 2) An alternating tone paradigm played on either right or left ear via MR compatible earphones, with alternating frequency (pure tones at 698.46 Hz and 440.00 Hz with a 0.1 s

duration of each tone). The two sensory stimuli were presented with random onsets and durations, sampled from a uniform continuous distribution in the range of 1.0-5.0 sec; visual and auditory stimuli timings were sampled independently. Overlaps between visual and audio stimuli were allowed, however, bilateral overlapping presentation of the same sensory stimulus (leftvisual with right-visual or left-auditory with right-auditory) was prohibited. The data were collected in 2 runs; in the first run, subjects were instructed to attend only one sensory modality (i.e., either visual or tonal) while ignoring the other. In the second run, they were instructed to attend the other sensory modality. Each scan consisted of 120 events: 60 events for visual and 60 for auditory stimulus; for each modality, 30 events on the right and 30 events on the left side spaced at inter-stimulus-intervals drawn from an exponential distribution (center = 5.6,  $\lambda = 9.8$ ). Control for attention was achieved by asking the subjects to press a button twice with their right/left index finger (depending on the lateralization of the attended stimulus) as soon as the attended stimulus terminated. These responses were recorded during the entire scans. Moreover, subjects were required to constantly fix their gaze on a green minuscule fixation spot in the center of the screen for the entire period of the scan. Subjects were given feedback on their incorrect or out-of-time (> 3 sec) responses (if any) via change in the color of the fixation spot to red. Eye fixation was monitored at all times during scans using an eye-tracking system (EyeLink 1000 Plus). If subjects excessively deviated their eye's fixation from the central dot, we stopped the scan and instructed the participants again and repeated the scan. However, this happened only during two fMRI runs. Subjects were first trained outside of the scanner to learn and perform the task comfortably and accurately (almost 100% correct) on short training runs. All subjects learned the task correctly. An example of the timing and the design of the task is illustrated in Figure 2.15.

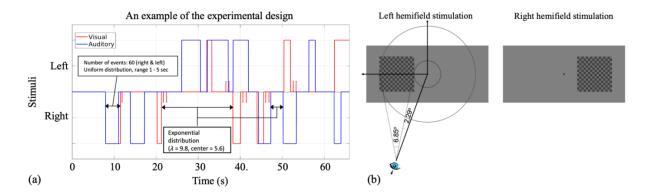


Figure 2.15: a) Illustration of a segment of the time-course of the visual-audio event related task. The blue line shows the timing of the auditory stimuli, the red line shows the timing of the visual stimuli, and the red stick line shows the subject responses (i.e., each time they press the button). In this sample demonstration, subjects were requested to attend to the visual stimulus and ignore the auditory stimulus. This is evident by the response pattern as the button is pressed twice as soon as the attended stimulus (i.e., visual stimulus) is terminated. b) Flashing checkerboard visual stimulus presented on the left and right hemifield.

MRI Acquisition Parameters Imaging was carried out using a 3 Tesla Siemens Magnetom Prisma scanner equipped with an 80 mT/m gradient system with a T2\*-weighted echo-planar imaging sequence using interleaved slice acquisition (TR/TE = 1000/30 ms; flip angle = 62°; field of view (FOV) = 200 × 200 mm; bandwidth = 1852 Hz/px; multiband factor = 4, matrix size = 100 × 100; voxel size = 2 × 2 × 2 mm; 64 axial slices with alternating phase encoding directions of anterior-posterior or posterior-anterior). Subjects were positioned supine inside the magnet bore wearing noise isolating MR safe earbuds to listen to the auditory stimuli. The flashing checkerboard visual stimuli placed within a square that was centered at the middle of the hemi-field filling up more than half of the hemi-field were projected onto a back-projection screen in the scanner. Each task-based fMRI (tb-fMRI) scan lasted 8 minutes (480 volumes). A resting-state fMRI (rs-fMRI) scan with the same length and parameters was also acquired for every participant. To prevent any bias in visual-attending/tonal-attending task modalities, we

alternated the order of fMRI acquisitions between; 1) visual-attending, resting-state, and tonal-attending; 2) tonal-attending, resting-state, and visual-attending; for each participant. An accompanying anatomical T1-weighted structural image was collected for localization and registration purposes in the same MRI session (TR/TE = 2300/2.32 ms; flip angle =  $8^{\circ}$ ; field of view =  $256 \times 256$  mm; matrix size =  $256 \times 256$ ; voxel size =  $1 \times 1 \times 1$  mm; 196 sagittal slices).

**Preprocessing of fMRI Data** The fMRI data were processed using FSL (V5.0.7) and in-housedeveloped packages. The preprocessing pipeline for the task-based fMRI data is illustrated in Figure 2.16. Briefly, slice timing correction was applied to the raw fMRI timeseries to account for the difference in the acquisition delay between slices (Parker et al., 2017; Parker and Razlighi, 2019a). At the same time, motion parameters were estimated on raw fMRI scans using rigid-body registrations performed on all the volumes in reference to the first volume. Additionally, the first volume was extracted from another fMRI scans with opposite phase encoding directions to estimate the geometric distortion correction field using a susceptibilityinduced distortions correction technique called topup (Andersson et al., 2003) provided in FSL software package (Smith S.M. et al., 2004). Then, the estimated motion parameters and geometric distortion field were combined and applied to the slice timing corrected fMRI timeseries to get the distortion and motion-corrected fMRI time-series. In order to enhance the precision in the localization of the statistically significant responsive voxels, no spatial smoothing was applied. To remove the slow scanner drift, a temporal high-pass filter (> 0.01 Hz) was applied to the fMRI timeseries. The pre-processed fMRI data were modeled with 6 predictors (except for the linearity analysis, which will be discussed later) for the presented stimuli and subject responses (i.e., visual left, visual right, audio left, audio right, motor-response left, motor-response right). Predictors were acquired by convolving the visual, auditory, and motor boxcar timings with the canonical double-gamma HRF. First-level analysis was performed via multiple regression using an in-house-developed software package in Python. Similar preprocessing was performed to the rs-fMRI data by applying slice-timing correction, spatial realignment, geometric distortion correction, and high-pass filtering (> 0.01 Hz). Structural scans were processed using Freesurfer (Fischl et al., 2004, 2002).

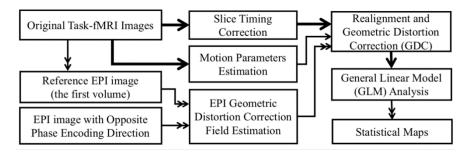


Figure 2.16: The preprocessing pipeline for task-based fMRI data. The thick arrows show the transfer of 4D fMRI data, the double thin arrow shows the transfer of the 3D data, and the thin arrow shows the transfer of the parameters.

Linearity of the cNBR and iNBR In this experiment we aimed to assess the linearity of the both NBR with regards to the change in the duration of the stimulation. The stimuli were categorized into four distinct categories with respect to their duration (i.e., category 1 included stimuli with durations between 1 to 2 seconds and in the same way category 2, 3, and 4 included stimuli with durations between 2 to 3, 3 to 4, and 4 to 5 seconds, respectively). The time series of the preprocessed fMRI data were standardized by subtracting the mean and dividing by the standard deviation. To prevent any bias in voxel selection toward any voxel with randomly exhibiting linear property, we employed bootstrapping technique where the trials were randomly split in half for voxel selection (training) and BOLD response extraction (testing). For a given iteration, the training trials' boxcar (convolved with a canonical HRF) was used in a general

linear modeling (GLM) analysis to obtain the significantly responsive voxels (|t| > 3). Once the voxels were selected, the training trials were disregarded and only the remaining trials (testing) were used for assessing the linearity in the selected voxels. The amplitude of each trial in the testing set was also normalized with regard to its duration to make sure it has a unit area under the curve in each trial's boxcar. This was done to maintain the same amplitude in all trials in the GLM predictors which essentially enables us to assess the increase in the magnitude of the BOLD response using the beta-coefficient of the GLM analysis. Each trial in the test set was then assigned to one of the four different regressors according to their categorized stimuli durations. Next, four separate GLM analyses were performed using one of the four regressors; Each one estimating the BOLD response magnitude for each duration category. Bootstrapping process was repeated with 500 iterations, and the beta-coefficient of each category was averaged separately for cNBR and iNBR across all iterations and right and left visual stimuli to compute the corresponding BOLD response amplitude. The subject-wise mean beta-coefficient (amplitudes) for the four duration categories were then plotted against the corresponding duration categories. We performed a least squares linear regression analysis along with t-test of the slope to check for significance of the linear relationship (if existed). As a sanity check, we also used this method to check the linearity of the PBR.

Generating region of interest Throughout this work, instead of performing the formal group level analysis in standard space, we performed the analysis in the subjects' native space (unless explicitly noted otherwise). Analysis in native space increases the precision of localizing ROIs in each subject compared to the regular group level analysis in the standard space. The latter often introduces spatial misalignments across different subjects due to lack of precision in non-linear

registrations (Klein et al., 2009; Liu et al., 2017; Razlighi et al., 2014). Hence, for each individual subject, two ROIs per hemisphere were generated. The first region of interest (ROI) was generated for each hemisphere, by selecting the voxels within the visual cortex that showed statistically significant PBR (activation) during the unilateral visual stimulation using the zstatistical map derived from first-level analysis (z > 4). The subject-wise mask of the visual cortex was obtained using FreeSurfer. The first ROI was then dilated by a spherical kernel with 10 mm radius - resulting in a large ribbon surrounding it in each hemisphere - to delineate the neighboring voxels required for identifying the NBR in the vicinity of the activated regions (cNBR). The union of the two masks on the opposite hemisphere (due to visual stimulation of opposite hemi-field) was used as the ROI to identify voxels with iNBR. Any intersection with the inferior parietal and precuneus regions was eliminated from the two generated ROIs, since they might be part of the NBR from the default mode network which may have different characteristics and/or underlying mechanism. Finally, in order to eliminate any possible misalignment or interhemispheric leakage due to a rather smooth point spread function of the fMRI BOLD signal, the two bilateral ROIs were constrained to be within each brain hemisphere (hemisphere mask delineated by using FreeSurfer software). This was also done to avoid any possible overlap between the ROIs from the two hemispheres.

Hemodynamic response functions of cNBR and iNBR The goal of this experiment was to extract and compare the shapes of the HRFs of the two task-evoked cNBR and iNBR obtained from the visual cortex. Since we are investigating the shape of the HRF, voxel selection cannot be performed using a canonical double Gamma HRF. This is to prevent any bias toward a preselected HRF shape. Hence, we used a set of optimized basis functions known as FMRIB's linear

optimal basis set (FLOBS) to perform our voxel selection for this experiment (Woolrich et al., 2004). FLOBS technique does not impose a fix timing and/or dynamic for the BOLD response; Thus, voxels exhibiting response with completely unique shape and dynamics can be selected as responsive voxels for a given stimuli timing. We selected the significantly responsive voxels according to the F statistics |F| > 6 within the predefined ROI masks. An initial response function for each voxel was computed by a weighted average of the FLOBS basis functions according to the estimated beta-coefficient in the first-level FLOBS GLM analysis. Then, we integrated the initial response function for the first 10 seconds interval to obtain the sign of the area under the curve, and we classified the significantly responsive voxels into either positive or negative responsive voxels. Once the negatively and significantly responsive voxels are identified within the generated ROIs, the time courses of the selected voxels were given to the FIR deconvolution technique, which to our knowledge is the least constrained approach for extracting the shape of the impulse response function in fMRI (Goutte et al., 2000). We extracted the voxel-wise HRFs of each subject for cNBR and iNBR for both attended and unattended stimuli. Subsequently, the extracted HRFs were averaged across all responses to the right and left visual stimuli to obtain the mean subject-wise HRFs for cNBR and iNBR for both attended and unattended stimuli (i.e., HRF<sub>cNBRatt</sub>, HRF<sub>iNBRatt</sub>, HRF<sub>cNBRunatt</sub>, and HRF<sub>iNBRunatt</sub>). For comparison purposes, the positive BOLD HRF was also extracted using the same procedure and the time-series were converted to percent change (subtracted by the mean and then divided by the mean).

We subtracted the mean signal of the pre-stimulus period (time points within 5 seconds before the onset of the stimulus) from the subject-wise HRF. Then, we up-sampled the subject-wise HRF with sinc-interpolation. In order to compare the magnitudes and dynamics of the extracted HRFs for cNBR, and iNBR, as well as for PBR, subject-wise extracted HRFs were

used to obtain onset time, time to peak, amplitude, falling edge time, and time to undershoot of the BOLD responses. As shown in Figure 2.20A for illustrating the PBR case, time to peak was defined as the first instance where the HRF reached its maximum magnitude starting from time zero (stimulus onset). The onset time was defined as the first time point where the HRF exceeded 10% of the maximum amplitude. The falling edge time was defined as the time duration between the peak time and the time at which the HRF reached back to its estimated average pre-stimulus magnitude. The time to undershoot was defined as the time that it took the HRF to reach its maximum opposite magnitude after falling back to the baseline, starting from time zero. For each characteristic, we removed measurements outside three standard deviations from the mean to eliminate the influence of outliers. Finally, Student's t-test was used to test for the significance of the difference (if any) between magnitude, time to peak, onset time, falling edge time, and time to undershoot of the HRFs obtained for cNBR, and iNBR, as well as for PBR.

Subject-wise expression of cNBR and iNBR The aim of this analysis was to assess the relationship between the subject-wise expression of different BOLD responses which could potentially hint at the underlying driver of NBRs. Using the previously generated ROI masks, the statistically significant voxels were selected inside each ROI using a z-statistics threshold of above +4 and below -3 for the positive and negative BOLD responses, respectively (not corrected for multiple comparisons correction). The NBR is usually a weaker signal than PBR, hence, we chose a slightly lower threshold for NBR to add more negatively responsive voxels. The subject-wise expression of cNBR and iNBR were calculated by averaging the beta-coefficient from the significantly responding voxels to the right and left visual stimuli. For comparison, subject-wise expressions of PBR were also obtained similarly. For each pair of the

BOLD responses (i.e., PBR vs cNBR, PBR vs iNBR, and cNBR vs iNBR), Pearson correlation coefficient (PCC) was used to assess the association (if any) between the BOLD amplitudes separately for the attended and unattended cases. Outliers were removed based on median absolute deviation and PCC was computed again to make sure the results were not an influence of outlier. The test of the difference between two correlation coefficients was used to test the significance of the difference in the correlation amplitude (use the absolute value of PCC) between pairs of the BOLD responses.

Functional connectivity between cNBR and iNBR In this analysis, we aimed to investigate the inter-hemispheric functional connectivity in the visual cortex between regions showing BOLD responses during unilateral visual stimulation (i.e., iNBR vs PBR, and iNBR vs cNBR). The similarly pre-processed rs-fMRI data were transformed to the tb-fMRI space using 6 degrees of freedom intra-subject registration (Jenkinson et al., 2002). A binary mask of the regions with significant PBR, iNBR, and cNBR was intersected with each participant's left/right hemisphere's visual cortex mask (delineated by using the FreeSurfer software) to obtain the mean time-series for the regions with PBR and NBRs from rs-fMRI data. The PCC was used to compute functional connectivity between the regions. Any significant difference between functional connectivity was assessed with the Student's t-test.

Interhemispheric spatial similarities between cNBR and iNBR The goal of this analysis was to investigate the topographical similarities between the spatial patterns of the BOLD responses that belong to two distinct hemispheres (i.e., iNBR vs PBR, and iNBR vs cNBR), elicited during unilateral visual stimulation. Similar to the HRF extraction analysis, our spatial similarity

analysis was within previously generated ROIs that exceed the selected significance threshold (i.e., |F| > 6) in the first-level FLOBS GLM analysis, and voxels were classified into positively and negatively responsive voxels based on the area under the curve during the first 10 seconds interval of the HRF. Spatial pattern similarity was measured by Dice similarity coefficient between regions showing significant cNBR and iNBR, and for comparison between iNBR and PBR. In order to compute the spatial pattern similarity between regions located in two different hemispheres, these ROI masks were required to be transferred into MNI standard space. To this end, the first EPI volumes from fMRI data (as the reference volume in preprocessing) were registered to their T1-weighted structural image using a rigid-body transformation and normalized mutual information. Then, each subject's T1-weighted structural image was registered to the standard MNI space using Landmark Guided Region Based Spatial Normalization (He and Razlighi, 2022). Combination of the two (i.e., the rigid-body transformation and the non-linear warping filed) was used to transfer the obtained ROI masks into MNI space. Next, the transferred ROI masks were flipped around mid-sagittal plane (i.e., mirrored) to be able to use DSC overlap measurement to quantify the spatial pattern similarities between iNBR and PBR, as well as iNBR and cNBR. To assess for significance in the difference (if any) between the DSC of iNBR vs PBR, and iNBR vs cNBR, t-test was used across the obtained DSC measurements.

**Behavioral correlates of the cNBR and iNBR** To assess the relationship between the NBRs and task performance, we used subject-wise median response-time as a measurement of performance, and subject-wise expression of NBRs, as explained above, as the strength of BOLD response. For comparison, we also investigated the relationship between PBR and performance

using the same method. The response-time was defined as the time interval between the end of the attended stimulus and the instance when the first corresponding button was pressed by subjects. Using PCC, we tested for any association between the median response-time of each subject and the corresponding expression for PBR, cNBR, and iNBR.

Attention dependency of the cNBR and iNBR In this analysis, the goal was to check the effect of attention on the negative BOLD signals. We used the difference in the amplitudes and dynamics of the previously extracted HRFs between the attended and unattended/ignored stimuli as a measure of attention dependency. Student t-test was used to assess the significance in the difference (if any) between the attended and unattended cases at every second after the start of the stimulus, multiple comparisons correction was performed using Bonferroni correction method.

### 2.3.3 Results

The visual stimulation induced statistically significant PBR in lower visual areas within the occipital lobe of all subjects. In addition, sustained, statistically significant NBRs ipsilateral and contralateral to the visual stimuli were observed in all subjects, for both attended and unattended cases. Participants responded correctly on 98.0/96.0% of the visual/audio stimulus presentations, where a correct response is defined as a button press within 3 seconds of the attended stimulus termination. Figure 2.17 illustrates the spatial pattern of a typical subject's PBR, cNBR, and iNBR to unilateral right hemifield presentation of attended visual stimuli using z-statistics overlaid on three orthogonal slices of the participant T1-weighted structural MRI image.

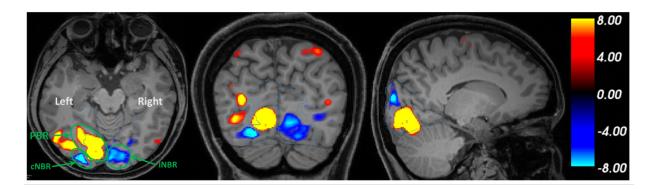


Figure 2.17: Demonstration of activation/deactivation in response to right visual hemifield stimulation from a single subject in the attended condition. Positive BOLD responses are color-coded with red/yellow and negative BOLD responses are color-coded with blue/cyan. The unilateral visual stimulation induces robust PBR in the contralateral (relative to the stimuli) visual cortex accompanied by a robust cNBR in its vicinity, and a robust iNBR in the opposite hemisphere. Note that spatial smoothing is carried out here only for better illustration.

While we did not impose any overlap between the timings of the visual and auditory stimuli, the event-related designs of the two sensory stimuli were independent, with the timing of the stimuli randomized separately for visual and auditory stimuli. This design resulted in some overlapping visual and auditory stimulations, as seen in Figure 2.15. To make sure the overlapping stimuli had negligible influence on our results, we categorized the stimuli according to their temporal overlap between each visual stimulus and the left or right auditory stimuli. Based on this, the visual stimuli trials were classified into two classes: 1) high visual and auditory stimuli overlap (overlap larger than 50%) and 2) low visual and auditory stimuli overlap (overlap smaller than 50%). We performed Student's t-test between the mean response time of these two classes' trials across subjects and found that there was no significant difference (t = -0.76; p > 0.45) between them. And there was also no significant difference between the bimodal stimuli overlapping rate between left and right presentations (t = 1.54; p > 0.13). The mean

bimodal stimuli overlapping rates of the left and right visual stimuli presentations were 0.63 and 0.61, respectively.

Eye gaze deviation quantification results We first performed the quantification of eye gaze deviation. For 20 healthy young subjects with eye tracking data available, left/right absolute gaze deviation from the screen center is  $1.3920 \pm 1.5777$  (mean  $\pm$  std) degree, and the median is 0.9922 degree. Mean of the subjects' absolute gaze deviation was within 1 degree in 71.37% of the time, between 1 to 2 degree in 11.37% of the time and more than 2 degree in 17.25% of the time. Next, we quantified the gaze deviation prior and during presentation of visual stimuli. The average gaze deviation during the pre-stimulus period of the visual stimuli (five seconds before to the onset of the stimuli) is  $-0.4959 \pm 1.7376$  (mean  $\pm$  std) degree for the left visual field presentation and  $-0.3195 \pm 1.4754$  (mean  $\pm$  std) degree for the right visual field presentation. The average gaze deviation during the presentation of the visual stimuli is  $-0.8580 \pm 2.0645$  (mean  $\pm$ std) degree for the left visual field presentation and  $0.0836 \pm 0.9869$  (mean  $\pm$  std) degree for the right visual field presentation. The negative and positive values represent the deviation is towards left and right, respectively. To quantify the amount of gaze deviation, we computed the absolute value of these subject-wise average gaze deviation. There is no significant difference between the amount of gaze deviation during the presentation of the left and right visual field stimuli (t = 0.9927; p = 0.3271). And no significant difference was found between the amount of gaze deviation during the baseline period of left and right visual stimuli (t = 0.1017; p = 0.9196). Lastly, we performed correlation analysis of the gaze deviation quantifications and the BOLD response. There is no significant correlation between the left/right gaze absolute deviation and the subject-wise mean amplitudes (beta-weight) of BOLD response (PBR: r = 0.0669, p >

0.7793; iNBR: r = -0.2601, p > 0.2680; cNBR: r = -0.0747, p > 0.7544). There is no significant correlation between the absolute amount of gaze deviation during the presentation of visual stimuli and the subject-wise mean amplitudes (beta-weight) of BOLD response for the left (PBR: r = 0.1253, p > 0.5988; iNBR: r = -0.1203, p > 0.6133; cNBR: r = -0.0073, p > 0.9755) and right (PBR: r = 0.3354, p > 0.1483; iNBR: r = -0.2131, p > 0.3670; cNBR: r = -0.1785, p > 0.4514) visual field stimuli. No significant correlation between the gaze deviation quantifications and the major characteristics of the BOLD responses was observed. In all analysis above, eye blink detection was performed with the EyeLink 1000 Plus system during the scan. The gaze position data during eye blinks were removed before the analyses.

Stimulus duration linearly scales the magnitude of cNBR and iNBR In this experiment, we aimed to assess the relationship between the magnitude of the task-evoked negative BOLD signals (i.e., cNBR and iNBR) and the stimuli duration. To this end, we averaged the beta-coefficient of the first-level GLM analysis fitted separately for each categorized stimuli duration. Results of the right and left visual stimulations are also averaged for this analysis. We then assessed the relationships between mean beta-coefficient and the categorized stimuli durations using linear regression. Figures 2.18a, 2.18b, and 2.18c show the averaged beta-coefficient as the BOLD response amplitude in terms of stimulus duration for cNBR, iNBR, and PBR, respectively. As illustrated in Figures 2.18a and 2.18b, the amplitudes of both cNBR and iNBR showed significant linear relationships with the stimulus duration (cNBR:  $\beta$  = -0.312, p < 0.009; iNBR:  $\beta$  = -0.169, p < 0.017) ranging from 1 to 4 seconds. These results provide evidence for linear relationships between the NBR amplitudes and stimulation duration, suggesting that the longer a stimulus duration is, the higher is the magnitude of both induced NBRs in the visual

cortex (i.e., amplitudes get more negative). Since the linearity of PBR has been already shown (Boynton et al., 1996), as a sanity check, we applied the same test of linearity to the PBR ( $\beta$  = 0.845, P < 6.116e-4; Figure 2.18c), confirming the linear relationship in the PBR for the same range of the stimuli durations.

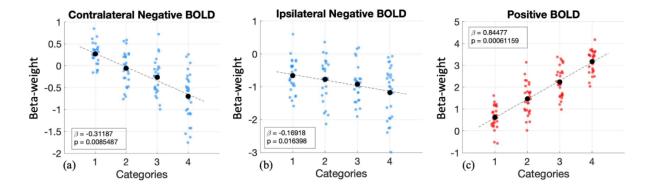


Figure 2.18: Linearity of the a) cNBR, b) iNBR, and c) PBR with respect to stimulation duration. The blue and red dots show, respectively, the mean amplitudes for negative and positive BOLD responses of each subject. The black dots indicate the mean amplitude of the BOLD responses (i.e., averaged over all subjects) for each duration category. The black dashed lines represent the regression lines. The absolute values of the mean cNBR and iNBR amplitudes scale linearly with the stimulus duration. Please note that the timeseries have zero mean and unit standard deviation for this analysis, thus the relative change between categories carries the information and not the beta-coefficient value at each category. As a sanity check for the method, we also applied the same method to the PBR. As expected, the PBR scales linearly with the stimulus duration.

The cNBR and iNBR have similar HRFs The goal of this experiment was to compare the magnitudes and dynamics of the HRFs obtained for the two NBRs. As mentioned in the methods section, we used the FIR deconvolution technique to extract the HRFs associated with the cNBR, iNBR, and PBR. The extracted HRFs for the attended and unattended cases are shown in Figure 2.19a and 2.19b, respectively. As is evident in these figures, in both attended and unattended conditions, the overall shapes of cNBR and iNBR are closely similar. To quantify this similarity, we tested for any statistically significant difference between the onset time, time to peak,

amplitudes, falling edge time and time to undershoot of the two NBRs with subject-wise upsampled HRF. As shown in Figure 2.20 and Table 2.2, there was no significant difference between the cNBR and iNRB regarding their onset time in both the attended ( $\Delta t = -0.1601 \text{ s}, p > 0.1601 \text{ s}$ ) 0.3770) and the unattended conditions ( $\Delta t = -0.0040 \text{ s}, p > 0.9827$ ), and there was no significant difference in the time to peak of cNBR and iNBR in the attended ( $\Delta t = -0.0580 \text{ s}, p > 0.7813$ ) and unattended ( $\Delta t = 0.1015 \text{ s}, p > 0.7104$ ) conditions, suggesting that the cNBR and iNBR HRFs start to rise and reach to their peak magnitude at approximately same time. We also observed no significant differences between the amplitudes of the two NBRs in both the attended  $(\Delta = -0.0578, p > 0.1969)$  and the unattended  $(\Delta = -0.0219, p > 0.5512)$  condition. We did not find any significant difference in the falling edge time of the two NBRs in the attended ( $\Delta t = -$ 0.3181 s, p > 0.6289) condition, whereas there is a significant difference in the unattended ( $\Delta t =$ -1.5770 s, p < 0.0472) condition, but it did not survive multiple comparison correction. Finally, no significant difference was observed between the cNBR and iNBR in terms of their time to undershoot for either of the attentional conditions (attended:  $\Delta t = -1.3289 \text{ s}, p > 0.2427$ ; unattended:  $\Delta t = -0.2268 \text{ s}$ , p > 0.8018). These findings suggest that there is no significant difference in the magnitude and dynamics of the HRFs extracted for the iNBR and cNBR after multiple comparisons correction. This evidence suggests that possibly common mechanism/s underlie the contralateral and ipsilateral NBRs while they are induced in two separate hemispheres of the human visual cortex.

Table 2.2: Comparison of the HRFs obtained for the cNBR and iNBR (cNBR vs. iNBR; \* p < 0.05; uncorrected).

Measurements	Attended	Unattended
--------------	----------	------------

Onset time	$\Delta t = -0.1601 \text{ s}, p > 0.3770$	$\Delta t = -0.0040 \text{ s}, p > 0.9827$
Time to peak	$\Delta t = -0.0580 \text{ s}, p > 0.7813$	$\Delta t = 0.1015 \text{ s}, p > 0.7104$
Amplitude	$\Delta = -0.0578, p > 0.1969$	$\Delta = -0.0219, p > 0.5512$
Falling edge time	$\Delta t = -0.3181 \text{ s}, p > 0.6289$	$\Delta t = -1.5770 \text{ s, p} < 0.0472 \text{ (*)}$
Time to undershoot	$\Delta t = -1.3289 \text{ s}, p > 0.2427$	$\Delta t = -0.2268 \text{ s}, p > 0.8018$

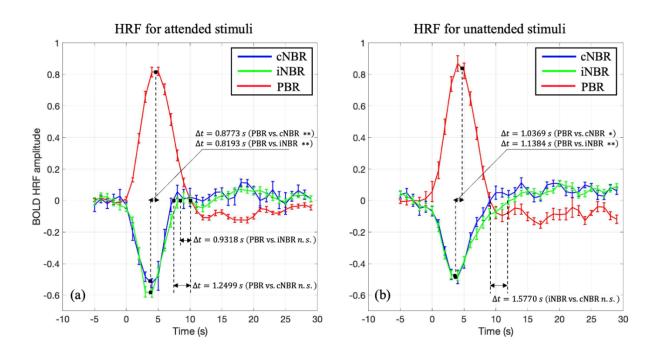


Figure 2.19: The HRFs of positive BOLD, and contralateral/ipsilateral negative BOLD responses to a) attended and b) unattended visual stimuli. The curves are adjusted based on average of the HRF for 5 seconds prior to the stimulus onset. The unit of the magnitudes is percent change (subtracted by mean and then divided by mean). Error bars represent the standard error of the mean. As is evident here, the two negative HRFs are closely similar in terms of their overall dynamics and amplitudes (\* p < 0.05; \*\* p < 0.01; Bonferroni correction).

To assess for any differences between the magnitudes and dynamics of the positive and negative BOLD HRFs, as seen in Figure 2.20 and Table 2.3, we compared the two negative BOLD HRFs to the positive one. In the attended condition, the positive BOLD HRF reached to its peak magnitude almost one second later than both negative BOLD HRFs (PBR vs. cNBR: Δt

= 0.8773 s, p < 0.0001; PBR vs. iNBR:  $\Delta t = 0.8193$  s, p < 0.0008). The amplitude of the positive BOLD HRF was significantly larger than both negative BOLD HRFs' (PBR vs. cNBR:  $\Delta = 0.2914$ , p < 8.2659e-08; PBR vs. iNBR:  $\Delta = 0.2336$ , p < 8.7143e-08). Furthermore, the PBR HRF returned to baseline only slower than the cNBR ( $\Delta t = 1.2499$  s, p < 0.0182). The time to undershoot was only significantly larger for the PBR HRF compared to cNBR HRFs ( $\Delta t = 2.5450$  s, p < 0.0098). In the unattended condition, similar to attended case, we observed the same trend in time to peak (PBR vs. cNBR:  $\Delta t = 1.0369$  s, p < 0.0037; PBR vs. iNBR:  $\Delta t = 1.1384$  s, p < 0.0031). The amplitude of the positive BOLD HRF is still significantly larger than both negative BOLD HRFs' (PBR vs. cNBR:  $\Delta = 0.4315$ , p < 3.6432e-15; PBR vs. iNBR:  $\Delta = 0.4095$ , p < 1.5076e-13). Unlike the results in the attended condition, there was only significant difference in the falling edge time between PBR HRF and iNBR HRFs ( $\Delta t = -1.8553$  s, p < 0.0017), and finally the PBR HRF time to undershoot was not significantly different from both negative BOLD HRFs' (PBR vs cNBR:  $\Delta t = 0.3628$  s, p > 0.6663; PBR vs iNBR:  $\Delta t = 0.1360$  s, p > 0.8792).

Table 2.3: Comparison of the HRFs obtained for the PBR and NBRs (\* p < 0.05; \*\* p < 0.01; uncorrected).

Measurements		Attended	Unattended
Onset time	PBR vs. cNBR	$\Delta t = 0.1703 \text{ s}, p > 0.2384$	$\Delta t = 0.0301 \text{ s, p} > 0.8619$
	PBR vs. iNBR	$\Delta t = 0.0102 \text{ s}, p > 0.9539$	$\Delta t = 0.0261 \text{ s}, p > 0.8575$
Time to peak	PBR vs. cNBR	$\Delta t = 0.8773 \text{ s, p} < 0.0001 (**)$	$\Delta t = 1.0369 \text{ s}, p < 0.0037 (**)$
	PBR vs. iNBR	$\Delta t = 0.8193 \text{ s}, p < 0.0008 (**)$	$\Delta t = 1.1384 \text{ s}, p < 0.0031 (**)$
Amplitude	PBR vs. cNBR	$\Delta = 0.2914$ , p < 8.2659e-08 (**)	$\Delta = 0.4315$ , p < 3.6432e-15 (**)
	PBR vs. iNBR	$\Delta = 0.2336$ , p < 8.7143e-08 (**)	$\Delta = 0.4095, p < 1.5076e-13 (**)$
Falling edge time	PBR vs. cNBR	$\Delta t = 1.2499 \text{ s}, p < 0.0182 (*)$	$\Delta t = -0.2783 \text{ s}, p > 0.6386$
	PBR vs. iNBR	$\Delta t = 0.9318 \text{ s}, p > 0.0547$	$\Delta t = -1.8553 \text{ s}, p < 0.0017 (**)$
	PBR vs. cNBR	$\Delta t = 2.5450 \text{ s}, p < 0.0098 (**)$	$\Delta t = 0.3628 \text{ s}, p > 0.6663$

Time to	DDD ve iNDD	$\Delta t = 1.2161 \text{ s, p} > 0.1999$	$\Delta t = 0.1360 \text{ s, p} >$
undershoot	TDK VS. INDK	$\Delta t = 1.2101 \text{ s}, p > 0.1999$	$\Delta t = 0.1300 \text{ s}, \text{ p} > 0.1300 \text{ s}$

0.8792

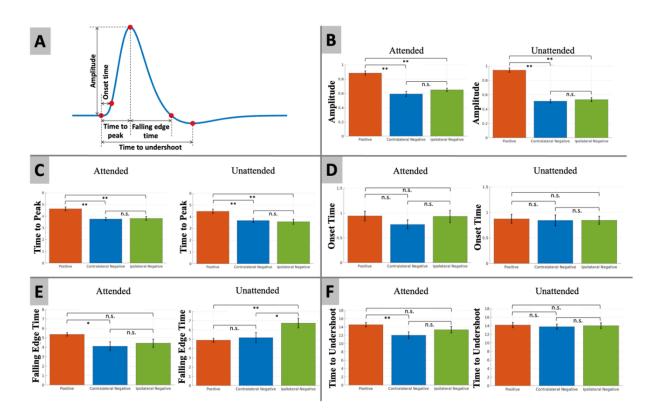


Figure 2.20: A) The definition of amplitude, time to peak, onset time, falling edge time, and time to undershoot of the BOLD responses as illustrated for the PBR case. B-F) Student's t-test of any statistically significant difference between the B) amplitude in percent change, C) time to peak, D) onset time, E) falling edge time, and F) time to undershoot of the two NBRs and PBR using sinc-interpolation up-sampled subject-wise HRF. Error bars represent the standard error of the mean. Statistically significant differences are marked with asterisk symbols (\* p < 0.05; \*\* p < 0.01; uncorrected).

**Subject-wise expressions of cNBR and iNBR are tightly coupled** The primary goals of this experiment were to investigate whether PBR observed in the visual cortex is the underlying force behind either or both cNBR and iNBR. To address this question, we examined the strength of the relationship between PBR and both cNBR and iNBR, and compared it with the strength of their

own relationship (between two NBRs). We compared the subject-wise expressions of the BOLD responses that were computed by averaging the beta-coefficient of the significant voxels within the generated ROIs. If PBR was the underlying force to induce cNBR and/or iNBR, then one would expect that the subject-wise expression of the PBR has a higher correlation with the expressions of cNBR and/or iNBR, than the corresponding correlation between the two NBRs' subject-wise expressions. On the other hand, if the iNBR was correlated more strongly with cNBR than PBR, then it is less likely that PBR would be the solo driving force of the iNBR or cNBR. Figure 2.21 shows the scatter plots of the subject-wise mean expressions of 1) iNBR versus cNBR, 2) PBR versus cNBR, and 3) PBR versus iNBR, for both attended (a, b, and c) and unattended (d, e, and f) unilateral visual hemifield stimulation. As depicted in Figure 2.21, the subject-wise expressions of the cNBR and iNBR were highly correlated with each other in both the attended (r = 0.8580, p < 1.0605e-08) and unattended (r = 0.8693, p < 8.2796e-09) conditions. The PBR was also shown to be significantly associated with cNBR (attended: r = -0.6408, p < 4.2085e-4, and unattended: r = -0.6466, p < 3.5784e-4) and iNBR (attended: r = -0.6131, p < 8.6863e-4, and unattended: r = -0.7032, p < 6.1550e-5). Although the cNBR and PBR were obtained from adjacent regions located in the same hemisphere, the cNBR showed significantly higher correlation with the iNBR (in the opposite hemisphere) than with the PBR (attended: z = 1.8037, p < 0.0357, and unattended: z = 1.9016, p < 0.0287; one-tailed), suggesting that PBR is less likely to directly associate with either of the two NBRs. These findings suggest that the two NBRs might not be associated exclusively by the PBR. Together with the results in the previous section, they indicate that the two NBRs have a common underlying neural and/or vascular mechanisms which might be different than the ones give rise to PBR.

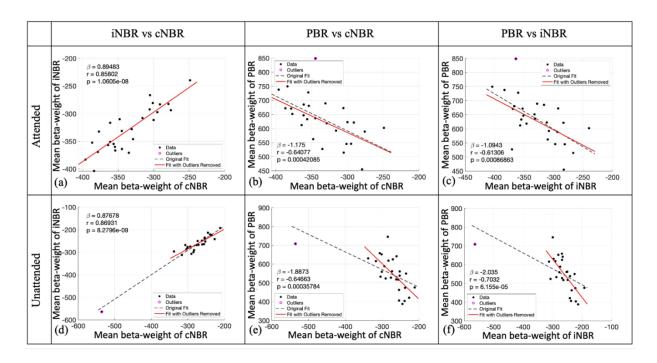


Figure 2.21: Correlation of the mean amplitudes of the BOLD responses to the visual stimuli in the attended (a, b, and c) and unattended (d, e, f) conditions. The value of the slop, Pearson correlation coefficient, the p-value of PCC are presented for each case. The dashed black lines represent the regression lines with all the data, and the solid red lines represent the regression lines with data after outliers removed. As is depicted, regardless of the attention condition, the subject-wise expression of the iNBR and cNBR are significantly more correlated with each other than each one with the PBR.

## Functional connectivity is not responsible for the high coupling between cNBR and iNBR

Results in previous sections provided evidence that cNBR and iNBR are more significantly coupled to each other (similar HRFs and highly correlated subject-wise expression) than each one with the PBR, highlighting the possibility of having similar underlying mechanism. In this experiment, we investigated whether the inter-hemispheric functional connectivity in the visual cortex could account for observing such high coupling between the two NBRs. While the regions with PBR and NBR responded to the external stimuli with opposite direction, they showed a strikingly high positive resting-state functional connectivity in all participants. Furthermore, there was no significant difference in the interhemispheric functional connectivity of the regions

with NBRs (iNBR and cNBR) versus the interhemispheric functional connectivity of the iNBR with regions of PBR (|t| < 0.38, p > 0.70; two hemifields data aggregated), see Figure 2.22 for more detail. In other words, the strong coupling between the two NBRs cannot be explained by the existing interhemispheric functional connectivity between them since the same level of functional connectivity holds between iNBR and PBR. The same relationship holds when the unilateral stimuli presented on the left hemifield (|t| < 0.24, p > 0.81), and also when the stimuli presented on the right hemifield (|t| < 0.50, p > 0.61), as shown in Figure 2.22. Furthermore, it should be noted that the relationship between the subject-wise expression of PBR and iNBR is in the opposite direction of the relationship between their FC. In other words, in the resting-state data increasing MR signal in the regions with PBR is associated with increase of the MR signal in the regions with NBR in the other hemisphere, whereas in the task-evoked response the task-related increase in MR signal (PBR) is associated with the task-related decrease in MR signal (iNBR) in the other hemisphere.

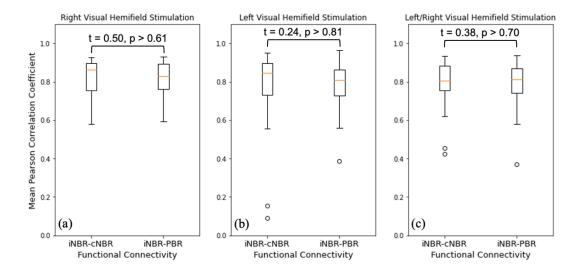


Figure 2.22: Subject-wise interhemispheric functional connectivity between regions with iNBR and cNBR are depicted using boxplot alongside the subject-wise functional connectivity between regions with iNBR and PBR using Pearson correlation coefficient for a) right visual hemifield stimulation, b) left visual hemifield stimulation, and c) the mean of the

two functional connectivity. The results of the group differences are also presented in each plot using Student t-test.

Spatial pattern of iNBR is more similar to PBR than cNBR Considering the substantially high correlation between the subject-wise expressions of iNBR and cNBR, and their similar HRFs, it is natural to examine whether the major callosal pathways which often connect interhemispheric homotopic regions can facilitate the creation of the two synchronized NBRs in the opposing hemisphere, or PBR being the underlying force for creation of iNBR through these interhemispheric pathways, as it has been postulated in the past (Bocci et al., 2014; Fabri et al., 2011; Schäfer et al., 2012). To this end, the interhemispheric spatial pattern similarities between the BOLD signals (both positive and negative) belonging to two opposite hemispheres were quantified and measured using DSC. If the interhemispheric callosal pathway was the reason behind observing such high coupling between the iNBR and cNBR, then the spatial patterns of the observed cNBR and iNBR should be significantly overlapping interhemispherically. On the other hand, if PBR/cNBR was the underlying force for creation of iNBR on the opposite hemisphere facilitated through major callosal pathway, then it should demonstrate significantly high interhemispheric spatial similarities with the spatial pattern of the iNBR. To visualize the interhemispheric spatial similarity between PBR, cNBR, and iNBR, Figure 2.23 shows the spatial pattern of the BOLD responses in the two opposite hemispheres of a single subject, projected on the inflated surface of the cerebral cortex, and subsequently on the spherical surface for a typical subject, during the attended unilateral visual stimulation. The approximate boundaries of different visual areas are delineated using a FreeSurfer extension (Benson et al., 2014) for this specific subject, to qualitatively examine any relationship between the extent of the iNBR and cNBR and retinotopic regions of the visual cortex. Since we did not perform actual retinotopic mapping in our fMRI task, we did not anticipate to see any quantitatively verified relationship.

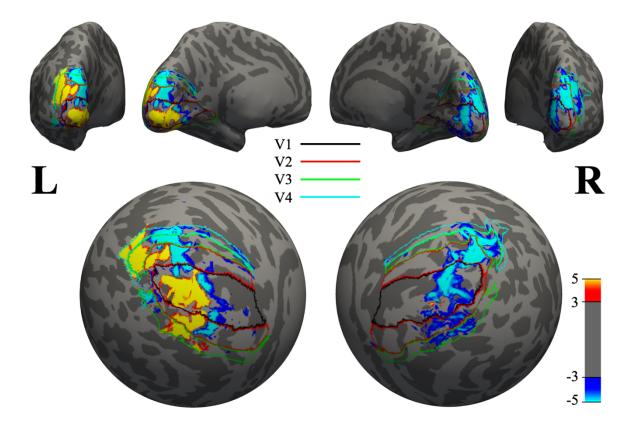


Figure 2.23: Spatial distribution of PBR, cNBR, and iNBR overlaid on a sphere (inflated brain). Boundaries of different visual areas V1 to V4 are depicted using different colors. As is demonstrated here, iNBR has a higher spatial correspondence to PBR than to cNBR. Note that spatial smoothing is carried out only for better visualization.

The interhemispheric spatial similarity between regions of iNBR and cNBR was very low (DSC =  $0.0532 \pm 0.0324$ ; mean  $\pm$  SD) and even significantly lower (p < 0.0084) than the interhemispheric spatial similarity between regions of iNBR and PBR (DSC =  $0.0720 \pm 0.0402$ ; mean  $\pm$  SD) for the attended condition. This result suggests that it is unlikely that the coupling of the two NBRs is facilitated through interhemispheric structural connection such as callosal pathways. Therefore, different regulatory mechanism with access to both hemispheres (probably in distal regions) are more likely to be responsible for such high coupling between two NBRs.

Performance correlates and attention dependency of the cNBR and iNBR The aim of this analysis was to examine whether either the cNBR or the iNBR has any significant association with the task performance. We previously reported that the NBRs detected from the DMN are attention-specific and correlated with task performance (Parker and Razlighi 2019). Here we aim to: 1) examine whether the same characteristics hold for NBRs detected from ipsilateral and/or contralateral visual cortex, 2) assess whether attention modulates both the iNBR and cNBR in a similar manner, and 3) compare the possible dependence of the cNBR and iNBR on attention to the corresponding dependence of the PBR. Using PCC between subject-wise expression of BOLD signal and median response-time, we found that the expression of the PBR, cNBR and iNBR did not show any statistically significant relationship with performance (details in (He et al., 2022)). We next assessed whether attending or ignoring a visual stimulus modulates the magnitudes and dynamics of the cNBR and/or iNBR in anyway in the visual cortex. We found that attention increased the magnitude of the NBRs' HRFs around 3-4 seconds following the onset of stimulus, and shortened the return time to the baseline (details in (He et al., 2022)). The results indicate that unlike the NBR detected from DMN, the iNBR and cNBR are not attention specific however attention modulates both iNBR and cNBR similarly suggesting common underlying mechanisms.

### 2.3.4 Discussion

In Section 2.3, we investigated the characteristics of the NBRs elicited simultaneously in the human visual cortex contralateral and ipsilateral to a unilateral visual stimulation. To the best of our knowledge, investigating the spatial and temporal properties of the cNBR and iNBR due

to the same visual stimulation has not been reported before. First, we demonstrated that the magnitudes of both NBRs increased linearly with the duration of the visual stimulus. While the linearity of PBR with respect to the stimulus duration has been previously investigated (Boynton et al., 1996; Dale and Buckner, 1997; Huettel and McCarthy, 2000), investigations of such linearity in the NBR are rare (see (Shmuel et al., 2002) for cNBR in visual cortex, and (Klingner et al., 2010) for iNBR in somatosensory cortex). To the best of our knowledge, assessment of linearity with respect to stimulus duration for simultaneous iNBR and cNBR has not been reported previously. Demonstrating the linearity is of paramount importance since most of the existing data analysis methods used in fMRI are conditioned on an underlying linearity assumption to extract the BOLD response including the GLM and FIR deconvolution methods used in this work.

Next, we found no significant difference between the amplitudes and dynamics of the HRFs extracted from the cNBR and iNBR after multiple comparison correction. In contrast, we found significant differences in both amplitudes and dynamics of the PBR HRFs and the two NBRs. Similar to our findings, Shmuel et al. demonstrated the difference between the falling edge time of the PBR and cNBR in the visual cortex (Shmuel et al., 2002). Liu et al. reported differences in the onset and falling edge times of the iNBR and PBR in the somatosensory cortex (Liu et al., 2011). Furthermore, consistent with the results of (Shmuel et al., 2002), we also found significant correlations between the expression of the cNBR and PBR. However, strikingly, the subject-wise expression of cNBR was correlated with iNBR (obtained from the opposite hemisphere) with a significantly higher correlation than with the PBR (obtained from adjacent regions), which has not been reported before. The fact that the HRF of the cNBR is different than the PBR which is detected in its proximity but similar to iNBR detected from the opposite

hemisphere suggests that there is a common force underlying both NBRs; However, PBR is less likely to be the underlying force since the subject-wise expression of the two NBRs are correlated significantly more than each NBR with PBR. Furthermore, our results suggest that while there is a strong interhemispheric functional connectivity between regions of iNBR and cNBR, the same level of functional connectivity also exists between the regions of iNBR and PBR; thus the functional connectivity is unlikely to be the underlying common mechanism for such strong coupling between the two NBRs. More interestingly, we demonstrated and reported a new finding that the regions with iNBR have a very small interhemispheric topographical spatial correspondence with both PBR regions (<6% on DSC) and cNBR (<5% on DSC) on the opposite hemisphere. While the spatial correspondence of iNBR was significantly higher with PBR than with cNBR, they were both too small to justify being part of interhemispheric homotopic regions. This finding suggests that the two NBRs with almost identical magnitudes and dynamics detected from two different hemispheres cannot be regulated by the interhemispheric callosal pathways, otherwise the spatial similarity between the two NBRs should have been higher than the one between iNBR and PBR regions.

We also found no significant relationship between task performance and NBRs while PBR showed a non-significant correlation trend with the response-time. While behavioral correlates of PBR have been shown previously (Pessoa et al., 2002), reports on the behavioral correlates of the NBR are inconsistent. Kastrup et al., reported significant correlation between the task performance and the iNBR in human somatosensory cortex during unilateral median nerve stimulation (Kastrup et al., 2008). However, Schäfer et al. did not find statistically significant correlation under the same conditions (Schäfer et al., 2012). In our experiment, the two NBRs showed no significant correlation with the task performance. This could possibly be

due to the lower magnitude of the NBRs (thus lower signal to noise ratio) relative to the PBR. Therefore, a study with larger number of subjects is warranted to address this question in the future.

Finally, we showed that attending to visual stimuli, slightly but significantly increased the peak magnitude of the ipsilateral NBR. This finding is consistent with the existing works mostly reporting an enhancement in the overall magnitude of the NBR with attention (Bressler et al., 2013; Heinemann et al., 2009; Müller and Kleinschmidt, 2004). However, in our results, the peak amplitude of PBR did not change with attention. This is in contrast with previous reports on attentional modulation of the PBR (Bressler et al., 2013; Buracas and Boynton, 2007; Gandhi et al., 1999). Furthermore, by analyzing each time point of the extracted HRFs, we found significant attentional modulations on the HRFs of cNBR in the return to baseline around 8 sec after stimulus onset. Similarly, by comparing the dynamics of the HRFs, we also found significant attentional modulations on the HRFs of iNBR in the falling edge time. Additionally, we found release from inhibition-like time-courses in the negative BOLD signals in the attended condition (results shown in the supplementary figures of (He et al., 2022)). Specifically, the falling edge following the cessation of the stimulus in the attended condition takes place earlier than their counterparts in the unattended condition. This attentional modulation in human visual cortex is similar to the release from inhibition demonstrated in macaque monkey visual cortex by (Shmuel et al., 2006), in the negative neurophysiological response associated with the NBR. Together, these findings highlight the different influence of attention on the PBR in comparison to NBRs.

The human brain hemodynamic response to any extrinsic stimulation is often more negative than positive. However, depending on the regions where the NBRs are detected, unlike

PBR, the neuronal and/or vascular mechanism underlying NBR might be different. For instance, the NBR often observed in the DMN may have completely different mechanism than the one observed in the sensory or motor cortices. Our main focus in this study was on the NBRs detected from visual cortex. We have previously reported the attention specificity of the NBR from the DMN regions, and its association with task performance (Parker and Razlighi, 2019b). While in the current study we observed that attention slightly modulated the magnitude of the NBR in the visual cortex, the disengagement from the task did not completely eliminate neither of the iNBR nor cNBR, as it did for the NBR detected from DMN regions. In addition, in contrast to the correlation of task performance with the NBR in the DMN, the subject-wise expression of the NBR in the visual cortex was not correlated with task performance. All together, these findings suggest that NBRs extracted from different regions of the brain may have different underlying neuronal and/or vascular mechanisms. Therefore, it is important for future studies to delineate what type of NBR they are investigating to remove any confusion about their results.

Our moderate size pool of samples may seem insufficient to detect any differences between the magnitudes and dynamics of the NBRs HRF. While we cannot rule out this possibility, we emphasize that with the same sample size we did detect significant differences between the magnitudes and dynamics of the two NBRs when compared with the PBR HRFs. Therefore, even if there is any significant difference between the HRF of the two NBRs, it should be substantially smaller than the difference observed between NBRs and PBR HRFs. Furthermore, we performed power analysis which showed that we have more than 85% power to detect significant differences between amplitude of the two NBR HRFs for differences as small as half a size of differences observed between two NBRs and PBR. On the same note, one might

also argue that the lack of correlation between the NBRs (as well as PBR) and performance might be due to the limited sample size of this study. Again, we emphasize that with similar sample size we were able to show previously that the NBR detected in the DMN was correlated with performance (Parker and Razlighi, 2019b). Future replication of our findings with a higher number of samples is warranted to ultimately rule out the effect of moderate sample size on our findings.

More recently Zhou et al. reported a non-linearity in the PBR for stimuli duration ranging from 17 ms to 533 ms (J. Zhou et al., 2018). Their results do not contradict our findings since our stimuli durations are longer and our study focus is on NBR; However, their results call for future studies to assess the linearity of the NBRs for stimuli duration shorter than 1 sec. While we used bootstrapping to prevent any bias in our voxel selection for evaluating the linearity of the NBRs, and we normalized each trial regressor to have unit area under curve, we feel that our task design is not optimal to test the linearity. Thus, we cannot completely rule out the possibility of having different HRF shape at different stimuli durations. Future studies with long inter-stimulus-interval (> 20 sec) are required to be able to completely address this concern. Finally, since we were only interested in the laterality of the visual and auditory stimulations in this study, we did not use a retinotopically-oriented visual task. While our preliminary results did not reveal any association between the NBRs and different visual area, we believe that future studies with optimal retinotopic mapping are required to examine the existence of any association between the NBRs and different visual areas.

On the origin of NBR Several hypotheses have been made with regard to the mechanisms underlying NBRs. Here, we discuss how our findings are in agreement or disagreement with or

suggest modifications to the existing hypotheses. As was reported previously by (Chen et al., 2005; Kastrup et al., 2008; Liu et al., 2011; Mullinger et al., 2014; Schäfer et al., 2012; Shmuel et al., 2003; A. T. Smith et al., 2004), passive vascular/blood steal hypothesis (Boas et al., 2008; Harel et al., 2002) cannot account for the observed task-evoked iNBR in the ipsilateral hemisphere, because the arterial systems of the two hemispheres are quasi-independent.

The venous back-pressure hypothesis (Boas et al., 2008; Goense et al., 2012; Shmuel et al., 2006) assumes that the increase in CBF to the PBR region increases the pressure in adjacent draining veins, thus slowing down the draining of blood from NBR regions adjacent to the PBR. However, for the venous back-pressure to be responsible for iNBR detected in the opposite hemisphere, the increased pressure needs to be generated at the level of the sagittal sinus. This means that the compliance of the sagittal sinus has to be sufficiently sensitive to react to the partial activation of the visual cortex. In addition, one might expect that any changes in the pressure of the sagittal sinus should evenly affect the ipsilateral hemisphere's regions adjacent to the sinus, which is not the case for the observed iNBR in this study.

Suppression of neuronal activity (Mullinger et al., 2014; Schäfer et al., 2012; Shmuel et al., 2006; A. T. Smith et al., 2004) could be responsible for observing the almost identical bilateral NBRs (i.e., iNBR and cNBR) facilitated by the existence of major interhemispheric pathways through corpus callosum, as reported previously (Bocci et al., 2014; Fabri et al., 2011; Schäfer et al., 2012). However, our findings indicate that the regions with iNBR and cNBR do not have the required homotopic spatial pattern similarity to be connected with major callosal pathways, making the suppression of neuronal activity hypothesis less likely to be the only force underlying the NBRs. Another possibility is that the region showing PBR induces the two NBRs via afferent signal of similar magnitude to both hemispheres to suppress activity in the

unstimulated visual regions. However, neither iNBR nor cNBR covers the entire unstimulated visual areas (see Figures 2.17 and 2.23). In addition, any similar or different retinotopic regions on the two hemispheres can be stimulated simultaneously and the associated PBR can be detected in the corresponding retinotopic regions. Therefore, it is uncertain how the visual cortex in one hemisphere would know whether the other hemisphere's visual cortex or even which retinotopic region of it has been stimulated at the same time to exclude it. Having said that we cannot rule out the possibility that the neural suppression is the underlying force for the two NBRs. In fact, we believe it is not even possible to rule out the neural suppression hypothesis using only fMRI. Nevertheless, we have shown evidence that if neuronal suppression is the underlying mechanism, it is possible that this mechanism is similar for both NBRs and they tend to be regulated through distal regions with access to both hemispheres.

Finally, a neurally controlled active blood regulation mechanism, as proposed in the "blood flow control" hypothesis (A. T. Smith et al., 2004), raises the possibility of having highly developed neural system for controlling and redistributing CBF throughout the entire brain. Our results are supportive of this hypothesis and indicate that at least the blood flow to the two hemispheres' visual cortices is regulated with a distal/deep brain structure with access to both hemispheres. If such a system exists, then it should have the capacity to tightly control the CBF across the two hemispheres, to generate highly coupled BOLD responses with similar magnitudes and dynamics as we have shown in this study. It has been previously reported that small clusters of neurons in the brainstem, basal forebrain, and thalamus have long projections of unmyelinated axons that are directly or indirectly (through GABA interneurons) innervate intracortical arterioles (Cipolla, 2009). Neuromodulators such as noradrenaline, serotonin, dopamine, and acetylcholine from these neurons are shown to influence CBF. For instance,

stimulation of cells with acetylcholine as their neurotransmitter in the basal forebrain dilated intracortical vessels within the cortex but did not alter the upstream pial arteries, causing drastic changes in CBF distribution throughout the whole brain (Iadecola et al., 1997). Altogether, this evidence and our results suggest that the brain CBF distribution is not driven entirely by activated or deactivated neurons but might be rather strategically coordinated and regulated through a separate subsystem with access to both hemispheres. However, the existence of such a system should not be considered as evidence against neuronal suppression hypothesis. Instead, we believe that it is unlikely that this system would restrain the blood flow to a brain region without any level of neuronal suppression. Future studies are warranted to investigate the mechanisms that harmonize this system that regulates the distribution of the blood flow in the brain and brain neural activation/suppression.

# Chapter 3: Spatiotemporal Dynamics of Functional Brain Networks during Salience Processing and Its Associations to the Neuromodulatory System

### 3.1 Overview

In this chapter, we aim to investigate the functional organization and connectivity of the brain network systems in the context of salience processing. In a perceptual experience, the brain is constantly processing internal goals and salient events in the environment. The interface between these two types of cognitive processes involves various top-down processes. Previous studies have identified multiple brain areas for salience processing, including the salience network, dorsal attention network, and the LC-NE system. Here, we propose to use a multimodal neuroimaging approach, to identify spatiotemporally dissociable brain networks, which might potentially reflect distinct cognitive processes in salience processing. In the literature, it is thought that the salience network and the LC-NE system have a central role in salience processing. However, interactions among these systems in the context of salient events processing remain unclear. In Section 3.3, we describe a study with simultaneously recorded pupillometry, EEG, and fMRI during an auditory oddball paradigm. The analyses of EEG and fMRI data uncovered spatiotemporally organized target-associated neural correlates. By modeling the target-modulated effective connectivity, we found that the target-evoked pupillary response is associated with the network directional couplings from late to early subsystems in the trial, as well as the network switching initiated by the SN. These findings indicate that the SN might cooperate with the pupil-indexed LC-NE system in the reset and switching of cortical networks.

In Sections 3.2 and 3.3, we utilized changes in pupil diameter as a surrogate for neural activity within the LC-NE neuromodulatory system. Our results provide evidence of the associations between the SN and the LC-NE system, which might collaboratively facilitate the reorganization between internal and external cognitive processes during salience processing. Building on the LC localization approach established in Section 3.2 and the Cortico-Subcortical Integrated Network Reorganization (CS-INR) model proposed in Section 3.3, we introduce a study in Section 3.4 that employs direct neuroimaging of the LC-NE system and investigates dynamic causal modeling of the connectivity between the critical nodes in the CS-INR model, specifically, the LC and the preSMA. Given that preSMA serves as a crucial node within the salience network, the findings of this chapter will provide valuable insights into the relationship between cortical networks and the brainstem neuromodulatory system during salience processing. Additionally, this research may have implications for various cognitive processes and neurological disorders beyond the attentional processing investigated in this chapter.

# 3.2 An Automatic and Subject-specific Method for Locus Coeruleus Localization and Functional MRI BOLD Activity Extraction

### 3.2.1 Introduction

With broad projections to the cortex, the LC has been implicated in arousal, attention, task performance and exploration behaviors (Aston-Jones and Cohen, 2005). In most fMRI studies, LC localization is based on a functional activation map (Gilam et al., 2017; Minzenberg et al., 2008), a predefined atlas (Hubbard et al., 2011; Morey et al., 2015) or both (Murphy et al., 2014). Since the LC is a small brainstem nucleus surrounded by other nuclei, these methods lack specificity in the anatomical evidence of the nucleus' location (Astafiev et al., 2010), and tend to

ignore individual variability in the LC's shape and location (Tona et al., 2017). To address this, some studies perform manual segmentation based on neuromelanin-sensitive Turbo Spin Echo (TSE) images (de Gee et al., 2017; Krebs et al., 2018). TSE images tend to localize the LC more accurately, although the images need to be manually inspected on a subject-by-subject basis. Here, by using both subject-specific TSE images and a predefined atlas, we develop an automatic localization method to extract BOLD activity in the LC. Given substantial evidence that pupil diameter and LC covary with one another (Aston-Jones and Cohen, 2005; Gilam et al., 2017; Gilzenrat et al., 2010; Joshi et al., 2016), we evaluated the quality of our results and compared them to alternative approaches by computing the trial-to-trial correlation between the extracted LC BOLD activity and simultaneously recorded pupil diameter.

### 3.2.2 Methods

Participants and experimental design Twenty-five healthy young subjects were recruited in this study and six of them were excluded from further analyses due to 1) missing neuroimaging data; 2) abnormality in the acquired neuroimaging data; 3) excessive movement; 4) inability to complete the task. Exclusion criteria were pre-established. Data from the remaining nineteen subjects (mean age  $\pm$  SD = 25.9  $\pm$  3.6 years, female/male = 13/6) were included in the analyses. All subjects had normal or corrected-to-normal vision and no history of psychiatric illness or head injury. The experimental design of our study and the recruitment process were approved by Columbia University institutional review board. All participants have provided informed consent to participate in the study, and written consent was obtained from the participants. We used a convenience sampling procedure through recruiting volunteer subjects from Columbia University and nearby areas. The sample size was based on previously published simultaneous

EEG-fMRI studies using a visual oddball task with seventeen subjects (Walz et al., 2014) and a decision-making task with twenty-one subjects (Muraskin et al., 2018).

An auditory oddball paradigm with 80% standard and 20% oddball (target) stimuli was performed, where standard stimuli were pure tones with a frequency of 350 Hz, and the oddball stimuli were broadband (laser gun) sounds. We chose an auditory (instead of visual) oddball paradigm to avoid the effects of luminance changes on the measurements of task-evoked pupillary response. We randomized the presentation of oddball and standard trials and trial order. The inter-trial intervals were in the range between 2 s and 3 s drawn from a uniform distribution, and each stimulus lasted for 200 ms. Subjects were first trained outside of the scanner to learn and perform the task comfortably and accurately on short training runs. All subjects performed the task correctly during training. During the data acquisition, stimuli were presented through MR compatible earphones, and subjects were instructed to maintain the fixation on the screen to a fixation target, and press a button (MR-compatible button box; PYKA, Current Designs, PA, USA) with their right index finger as soon as they heard the oddball sound. And subjects were instructed to ignore standard tones. Every subject was scheduled to complete five runs (105 trials per run), with an average of 4.7 runs per subject (range from three to five, SD = 0.7 runs) acquired in the experiment. The auditory oddball experimental task paradigm is illustrated in the first row of Figure 3.5, where the first five trials were constrained to be standard stimuli, and no consecutive oddball trials was allowed.

**Data acquisition and preprocessing** A 3T Siemens Prisma scanner was used to acquire pupillometry, EEG and fMRI with a 64-channel head coil. Pupillometry was recorded with a MR-compatible EyeLink 1000 Plus in Long Range Mount, at a sampling rate of 1 kHz. EEG was

recorded with a 64 channel BrainAmp MR Plus system (Brain Products, Germany), at a sampling rate of 5 kHz. The 64 channels include 63 cap electrodes and 1 ECG electrode in an extended 10-20 configuration with ground electrode at AFz and reference electrode at FCz. Functional MRI data were collected with T2\*-weighted echo planar imaging interleaved slice acquisition (TR = 2100 ms; TE = 25 ms; voxel size  $3 \times 3 \times 3$  mm; Matrix Size =  $64 \times 64 \times 42$ ; 150 volumes). For localization and registration purposes, we collected T1-weighted structural image (MPRAGE, TR = 2300 ms; TE = 3.95 ms; voxel size =  $1 \times 1 \times 1$  mm; Matrix Size = 176  $\times$  248  $\times$  256) and T2\*-weighted high-resolution EPI (TR = 6000 ms; TE = 30 ms; voxel size 2  $\times$  $2 \times 3$  mm; Matrix Size =  $96 \times 96 \times 42$ ; single-volume). For the localization of the LC, we also collected neuromelanin-sensitive MRI data using T1-weighted turbo-spin-echo acquisition (TR = 600 ms; TE = 14 ms; voxel size  $0.43 \times 0.43 \times 6$  mm; Matrix Size =  $416 \times 512 \times 5$ ). The fMRI data were processed using FSL (S. M. Smith et al., 2004) with preprocessing pipeline shown in Figure 3.1(a) and inter-modality registration as in Figure 3.1(b) (Greve and Fischl, 2009; Jenkinson et al., 2002). MR-compatible EyeLink 1000 Plus in Long Range Mount was used for pupillometry, with pupil diameter preprocessed as in (Urai et al., 2017). More details of pupillometry, EEG and fMRI data preprocessing are included in Section 3.3.2.

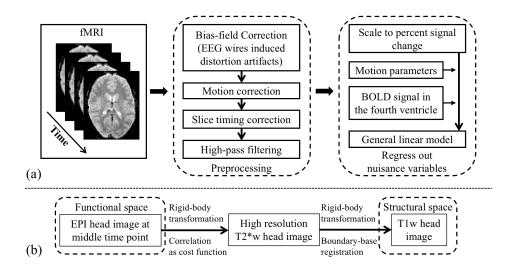


Figure 3.1: (a) fMRI data preprocessing and nuisance signal regression. The middle time point EPI volume was used as the reference in motion correction. No spatial smoothing was applied. Motion parameters include 6 standard head motion parameters, their temporal derivatives, and the squares of the above 12 motion parameters. (b) Intra-subject intermodality image registration.

Data acquisition specifications (along with the rigorous measures taken to ensure data quality) were described in detail in (Hong et al., 2022). Specifically, proper synchronization between EEG recording and MR imaging was ensured via Brain Products' SyncBox. The SyncBox receives pulses coming from the scanner's gradient clock board directly, and can therefore synchronize the sampling rate of the amplifier with the scanner clock system (Brain-Products., 2019). And to ensure subject safety during simultaneous EEG and fMRI acquisition, the scalp and ECG electrodes were embedded with series resistors of 10 kOhm and 20 kOhm, respectively. During the experiment, electrodes' impedances were kept under 25 kOhm (including the built-in resistors on each electrode) to minimize the noise in EEG acquisition.

**Localization of the LC and LC BOLD activity extraction** We used a combination of a predefined LC atlas (Keren et al., 2009) and subject-specific TSE images to determine the spatial

distribution of the LC in subjects' structural space, and then performed a more precise localization in functional space. Specifically, the LC atlas includes both one standard deviation (SD) and two SD estimates of the peak LC signal in standard space, and can be used as a template to map the spatial location of the LC in the brainstem. We first transformed the atlas to the structural space (Andersson et al., 2007), denoting these 1SD and 2SD LC masks as  $M_{1SD}$  and  $M_{2SD}$ . We denote the TSE images as  $I_{TSE}$ . Next as shown in Figure 3.2, and contrary to other studies (Gilam et al., 2017; Hubbard et al., 2011; Murphy et al., 2014) which localized LC in standard space, we first identified the spatial distribution of the LC in the structural space in order to eliminate resampling of the fMRI signal. As the LC shows a hyperintensity in TSE images (Sasaki et al., 2006), voxels within the LC structure exhibit high intensity compared to voxels which are outside of the nucleus. We used subject-specific  $I_{TSE}$  alongside  $M_{1SD}$  and  $M_{2SD}$  to develop a quantitative criterion. This criterion compares the intensities of voxels,  $I_{TSE}$ , in the LC mask and intensities of voxels in the vicinity of the mask. This localization strategy results in three outcomes, summarized in Figure 3.2.

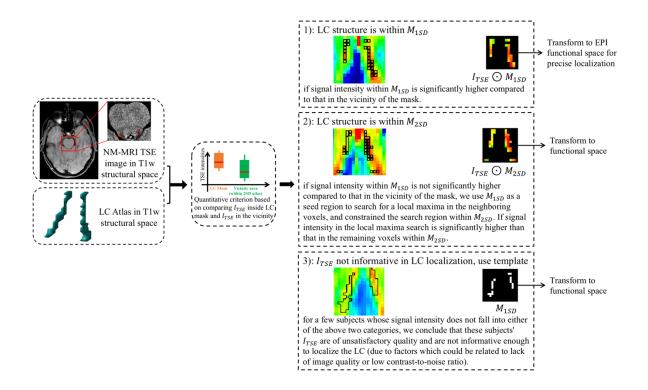


Figure 3.2: LC localization using a predefined LC atlas and the TSE image of each subject. In T1w structural space, we use a criterion (Student's t-test) to determine a coarse LC location. Then, either TSE intensities in the LC mask or an LC atlas is transformed to EPI functional space for a more precise localization (using trilinear interpolation). The result is one of three possible outcomes: 1) we localize the LC structure within  $M_{1SD}$ ; 2) we localize the LC structure within  $M_{2SD}$ ; 3) we localize the LC structure with the predefined LC atlas (i.e., without using any information from  $I_{TSE}$ ).

After identifying the spatial distribution of LC in the structural space, we fine-tuned the localization of LC in functional space by transforming  $I_{TSE} \cdot M_{1SD}$ ,  $I_{TSE} \cdot M_{2SD}$ , or  $M_{1SD}$  to functional space, respectively for the three outcomes given in Figure 3.2. We included both two-voxel and six-voxel versions of the LC in functional space. Voxel intensity within these fine-tuned LC masks were then normalized to represent the probability of each voxel being inside the LC structure. These probability maps were then applied to BOLD signal at LC, and produced

weighted average LC BOLD signals. Signals in the two-voxel and six-voxel LC masks are denoted as core-LC and entire-LC BOLD, respectively.

# 3.2.3 Results

LC BOLD activity extraction was evaluated by correlating LC BOLD signal to trial-to-trial variability of pupil diameter baseline (PDB) and pupillary response (PR) (see Figure 3.3(a)). Correlation analyses were carried out using a general linear model, with PDB and PR as the explanatory variables, and LC BOLD as the response variable. On the group level, we used a one sample t-test to determine if parameter estimates were significantly different than zero. As shown in Figure 3.3(b), BOLD activity extracted from core-LC with our method has a higher correlation with trial-to-trial variability of PDB (t = -3.499; p < 0.003) compared to activity extracted with an atlas-based method (t = -2.378; p < 0.029) or a local maximum-based method (t = 1.476; p > 0.157).

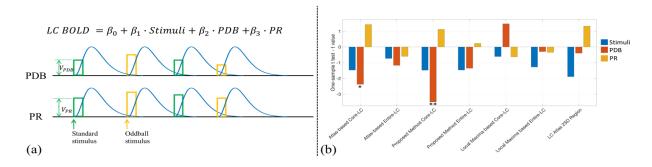


Figure 3.3: (a) GLM to estimate and test the contributions of PDB and PR to LC BOLD activity (controlling for the variance due to the presence of stimuli). Trial-to-trial variabilities of PDB and PR ( $V_{PDB}$  and  $V_{PR}$ ) were modeled as boxcar functions with the amplitude of each trial modulated by the pupil measurements. The boxcar functions were convolved with a canonical double-gamma hemodynamic response function before fitting into the GLM. (b) Group level statistical analysis in testing regression weights against zero. \*p < 0.05; \*\*p < 0.01.

# 3.2.4 Discussion

The locus coeruleus is a small nucleus in the brainstem whose function is integral to regulating cognitive arousal. Despite the LC's importance in cognitive processing, localizing it in functional space is challenging. Here, we developed a method that uses both subject-specific TSE images and a predefined atlas to automatically localize and extract BOLD activity from the LC. Using correlation to pupil dynamics as a metric, we compared our method to competing approaches. We found that core-LC BOLD activity extracted with our method had a stronger and more significant correlation with trial-to-trial variability of baseline pupil diameter, an important metric since non-luminance changes in pupil diameter have been shown to covary with LC electrophysiological recordings in non-human primates (Joshi et al., 2016). Given the substantial interest in how the LC modulates cortical brain dynamics to affect human cognition, we believe our approach would have utility for those interested in relating LC BOLD to cortical dynamics and behavior.

# 3.3 Pupillary Response Is Associated with the Reset and Switching of Functional Brain Networks during Salience Processing

### 3.3.1 Introduction

To navigate complex and dynamic environments our brains cannot allocate attention to everything, but instead must continuously mark and process salient objects (Uddin, 2015). For example, when we are walking on a busy street, we will likely direct attention to the traffic lights, a siren, and our planned route. In psychology and neuroscience, the term 'salience' refers to a noticeable or important object that stands out from the surroundings or background. Salience is usually accompanied by unexpectedness, novelty, and infrequency (Harsay et al., 2012). Typically, salience processing involves two general mechanisms (Menon, 2011): 1) bottom-up

processing that includes filtering and amplifying the sensory information; 2) top-down processing in support of anticipation, cognitive control, and goal-directed behaviors. To investigate salience processing, one of the widely used experimental paradigms is the oddball task, where subjects are instructed to detect distinct infrequent target stimuli in a stream of standard stimuli. In previous fMRI studies, a variety of brain areas have been identified as correlates of salience processing, including regions in the dorsal attention network, salience network, sensory cortex, primary somatosensory cortex (S1), and subcortex (Downar et al., 2002, 2000; Harsay et al., 2012; Kim, 2014). However, it is challenging to dissociate and interpret the distinct cognitive processes underlying these spatially distributed regions. Even though functional connectivity analyses have been used to dissociate brain networks (Seeley et al., 2007), the lack of time scales and the directionality in the couplings of these brain regions and networks still hinder the inference of their roles in salience processing.

Besides cortical networks, the locus coeruleus, as the primary source of norepinephrine, has also been associated with salience processing. The phasic LC activity has been shown to produce the P300 event-related potential (ERP), which typically appears robustly following target stimuli (responds weaker following standard stimuli) in oddball paradigms (Aston-Jones and Cohen, 2005; Vazey et al., 2018). Besides the P300 ERP, pupil diameter has also been used as a psychophysiological marker of the LC activity (Murphy et al., 2011). For example, in a single-unit recording study, both the spiking activity in the LC and pupil diameter are evoked following unexpected auditory stimuli (Joshi et al., 2016). Trial-by-trial associations were also observed between the pupillary response magnitude and LC responses. The association between the activity in the LC and pupil diameter fluctuations has also been shown in an fMRI study with oddball paradigm (Murphy et al., 2014). Together, these findings indicate the reliability of LC-

pupil relationships during neural processes of salient stimuli in the oddball paradigm. Pupil diameter fluctuations reflect salience, attention, surprise, efforts, and arousal (Joshi and Gold, 2020). In the oddball paradigm, target-driven pupil dilation reflects not only bottom-up processes, but also top-down cognitive processes of decision-making and task demands (Joshi and Gold, 2020).

Both the cortical network dynamics and the LC-NE system have been well characterized, such as the network switching model of the SN and DAN (Menon, 2011), and the network reset and the adaptive gain theory of the LC (Aston-Jones and Cohen, 2005; Bouret and Sara, 2005; Gilzenrat et al., 2010). Even though the SN, DAN, and the LC-NE system have been closely related to each other (Aston-Jones and Cohen, 2005; Corbetta et al., 2008; Hermans et al., 2011; Mäki-Marttunen and Espeseth, 2021) and all centrally positioned in salience processing, it is still unclear what their integrative roles are in the cognitive processes of salient events. Hence, it would be valuable to investigate the cortico-subcortical associations between the cortical network dynamics and pupil-indexed neuromodulatory systems, such as the LC-NE system. Critically, a better understanding requires the assessment of the directional couplings between cortical networks, and their associations with the pupil measurements (brain-pupil relationships) in the context of salience processing.

Emerging evidence from the recent literature indicates that neuromodulatory systems, such as the LC-NE system, are important factors in shaping functional network connectivity, reorganization, and dynamics (Brink et al., 2016; Shine, 2019; van den Brink et al., 2019; Zerbi et al., 2019). Thus, in this study, we explored this possibility using simultaneous recordings of pupillometry, EEG, and fMRI in an oddball paradigm. We first used a single-trial variability (STV) EEG-informed fMRI analysis, which allowed us to map the neural cascade underlying

salience processing. Second, with the functional connectivity (FC) analyses of the fMRI data, we were able to map dissociable spatiotemporal functional network organizations of these neural correlates. Then, by leveraging the temporal dynamics of EEG, we further characterized the directional interactions between these regions with an effective connectivity state-space model (Tu et al., 2019). Finally, we assessed brain-pupil relationships, which indicate the cortico-subcortical associations between the cortical network dynamics and the pupil-indexed LC-NE system. Specifically, we hypothesized that the pupil-indexed LC activity is associated with the effective connectivity of salience processing functional networks. Our results suggest that pupil-indexed LC-NE system and the SN share an integrative role in the reset and switching of functional brain networks in salience processing.

### 3.3.2 Methods

In this section, we describe the analyses of the multimodal pupillometry-EEG-fMRI data, specifically focused on data preprocessing, EEG single-trial analysis, EEG-informed fMRI analysis, fMRI functional connectivity analysis, EEG effective connectivity analysis, and brain-pupil correlation analysis. We used the same multimodal neuroimaging dataset as described in the section 3.2, and the details of participants, experimental design, and simultaneous pupillometry-EEG-fMRI data acquisition were described in details in the section 3.2.2. A flow chart is included in Figure 3.4 to illustrate the steps of data processing and single-modality/cross-modality data analyses.

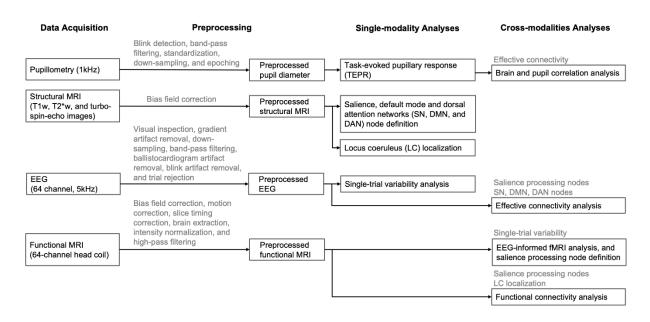


Figure 3.4: Flow chart illustrating the steps of data acquisition, preprocessing, single-modality analyses, and cross-modality analyses.

Pupillometry data preprocessing and epoching The preprocessing pipeline was adapted from the approach in (Urai et al., 2017). Firstly, blink detection was performed with Eyelink software, and then the blinks were padded by 150 ms and linearly interpolated. Additional blinks were further removed with a peak detection algorithm. We computed pupil diameter from the pupil area data, and then the pupil diameter time series were filtered with a bandpass second-order Butterworth filter (0.01 Hz to 10 Hz). Then, the pupil diameter data of each run were z-scored independently, and down-sampled to 500 Hz (the same sampling rate of the preprocessed EEG data). The preprocessed pupil diameter data were epoched from 500 ms before the stimulus to 2000 ms following the stimulus. Two pupil diameter measurements were examined including the prestimulus baseline pupil diameter (BPD) and the task-evoked pupillary response (TEPR). The BPD was defined as the averaged pupil diameter from 500 ms before the stimulus to the onset of the stimulus, and TEPR was defined as the maximum percentage deviation from BPD within each epoch.

**EEG preprocessing** Visual inspection was first performed, to make sure the raw EEG signal was not contaminated by confounding factors, including TR volume jitter and data saturation. An average artifact template subtraction approach was then used to remove the gradient artifact with Brain Products' Analyzer2 data processing software (Abreu et al., 2018; Allen et al., 2000). The data were then down-sampled to 500 Hz. After the gradient artifact removal, a tenth order median filter was applied, to reject any residual gradient artifact. Then, the EEG data were filtered with a fourth order bandpass Butterworth filter (0.5 Hz to 50 Hz), to remove DC drift and high frequency noise. After filtering, each subject's EEG data were concatenated over runs for the application of ballistocardiogram artifact (BCG) removal. Specifically, QRS detection was first carried out, and then the BCG was removed with EEGLAB's FMRIB plugin (simple mean approach). The BCG removed data were then re-referenced to the common average. The final step of preprocessing is blink artifact removal, where independent component analysis (ICA) was performed using EEGLAB's ICA function to compute ICs, manually identify and remove the blink ICs (Jung et al., 2000). The preprocessed EEG data were epoched identically as the pupillometry data from 500 ms before stimulus to 2000 ms following the stimulus. Then, baseline correction was carried out by removing the mean baseline value, which was computed from 500 ms before the stimulus onset to the stimulus onset for each epoch. We performed a trial rejection using a probability distribution-based criterion. Specifically, we rejected trials where the EEG signal from a single channel that is outside of 6SD, and the EEG signals from all channels that are outside of 2SD. We also rejected trials where subjects incorrectly responded or failed to respond.

Structural and functional MRI preprocessing The fMRI data were processed using FSL (V6.0) (S. M. Smith et al., 2004). Briefly, motion correction was performed using rigid-body registrations on all the volumes in reference to the middle time point volume (Jenkinson et al., 2002). Then, slice timing correction was carried out with Fourier-space time-series phaseshifting. The non-brain tissues were removed using BET (Smith, 2002). After that, grand-mean intensity normalization was applied by scaling the entire 4D data with a multiplicative factor. Lastly, a high-pass filtering (Gaussian-weighted least-squares straight line fitting, cut-off frequency 0.01 Hz) was carried out. No global signal regression was applied, since the global signal includes neuronal-related signals, and global signal regression has shown to introduce artificial negative correlations in the functional connectivity (Caballero-Gaudes and Reynolds, 2017). In the spatial normalization, the middle time point EPI volume head image of the fMRI data was rigidly registered (cost function as correlation) to the high resolution T2\*w head image. Then, the T2\*w head image was rigid registered (Boundary-based method) (Greve and Fischl, 2009) to the T1w head image. Lastly, the subject's T1w brain image was initially affine transformed and then non-linearly registered to the MNI152 (the nonlinear 6th generation atlas from FSL) brain image using FLIRT (Jenkinson et al., 2002) and FNIRT (Andersson et al., 2007) from the FSL software package. The structural T1w images were processed using FreeSurfer pipeline (Fischl et al., 2004), which resulted in brain tissue segmentations and surfaces reconstruction. The FreeSurfer segmentations of the T1w images include grey matter, white matter, lateral ventricles, brain masks, etc. And each subject's T1w image was also used to construct the volumetric head model and the source model using the FieldTrip toolbox (Oostenveld et al., 2011) for the effective connectivity state-space model.

**EEG single-trial analysis** A single-trial analysis with the sliding window approach was performed on the preprocessed EEG signal amplitude (Parra et al., 2005). Specifically, with a linear classifier maximally discriminating the target versus standard trials, a hyper-plane was learnt to project the multidimensional EEG signal into lowdimensional EEG single-trial variability discriminating components. Given the EEG signal,  $y_i(t)$  at time t, where  $i = 1, 2 \dots, T$  denotes trial index, logistic regression was used to learn the projection weights  $w(\tau)$ . The lowdimensional EEG STV discriminating components will be:

$$d_i(\tau) = \frac{1}{N} \sum_{t=\tau - \frac{N}{2}}^{\tau + \frac{N}{2}} w(\tau)^T y_i(t),$$
 (3.1)

where N = 50 ms denotes window width, the window center  $\tau$  was shifted from 0 to 1000 ms with respect to the stimulus onset in 25 ms increments. For each temporal window, the classifier performance was assessed with the AUC using leave-one-out (LOO) cross-validation. A permutation test was used to obtain the significance threshold for the AUC (100 times of permutations for each subject), where trial labels were randomly permuted and LOO was carried out. The null distribution of AUC values was generated and a threshold of p < 0.01 was used. Details of the STV analysis are illustrated in the Figure 3.5.

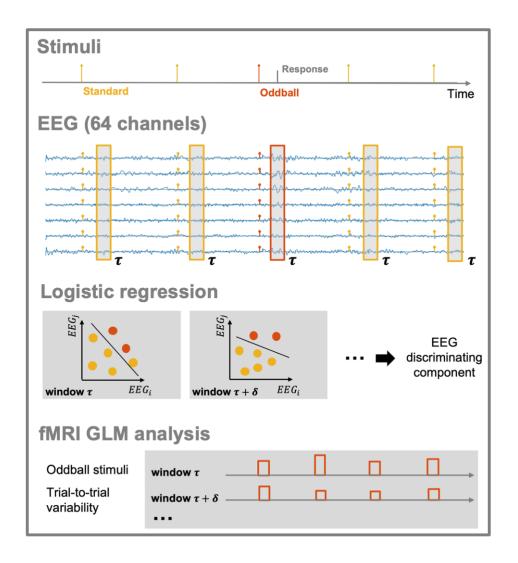


Figure 3.5: Schematic illustration of auditory oddball paradigm, single-trial analysis, and single-trial variability EEG-informed fMRI analysis. For each temporal window  $\tau$ , we applied a single-trial analysis with the extracted EEG data in the windows from all the trials, where a logistic regressor was trained to learn a weight matrix w maximally discriminating the target vs standard trials. From the weighting on the EEG channels with matrix w, an EEG discriminating component was computed as a low-dimensional representation of the EEG data. For example, two EEG sensors (channel i and j) were illustrated in the figure with a hyperplane discriminating target (red dots) and standard (yellow dots) trials. Similarly, single-trial analysis was applied to all other temporal windows spanning the trial independently with a sliding window approach (step size as  $\delta$ ). The EEG discriminating component at each temporal window was used to modulate regressors in a general linear model (GLM) to predict fMRI BOLD response (convolved with the canonical hemodynamic response function along with other regressors). The GLM analysis was applied with each temporal window independently.

STV EEG-informed fMRI analysis We fit a GLM for each EEG STV time window. Firstlevel GLM was performed independently on each voxel using multiple regression with five variables of interest. The regressors included: 1) event-related regressors with unmodulated height, and both onset and duration matched to the presence of the stimulus (one each for targets and standards); 2) RT variability regressor with unmodulated height, onset matched to the stimulus onset, and duration matched to the RT of the trial (orthogonalized with respect to the targets event-related regressor); 3) EEG STV regressors with height parametrically modulated using the demeaned EEG STV discriminating component, onset set to the time of interest  $\tau$ , and duration fixed to 100 ms (one each for targets and standards, orthogonalized with respect to the corresponding event-related regressor, oddball EEG STV regressor was also orthogonalized to RT regressor); 4) confounds (motion parameters, temporal derivatives of the variables of interest). At each time window  $\tau$ , the demeaned output of the logistic regression classifier, as the EEG STV discriminating component  $\tilde{d}_i(\tau) = d_i(\tau) - d_{mean}(\tau)$  was used to modulate the height of the EEG STV regressor boxcar function. All regressors were convolved with canonical Double-Gamma hemodynamic response function (HRF). The preprocessed fMRI data were spatially smoothed with a Gaussian kernel of FWHM 5 mm, then were fit with the GLM resulting to five different statistical parametric maps which will be warped onto a standard space (i.e. MNI152) to be able to perform group-level statistical analysis. For group-level statistical inference, we used FMRIB's Local Analysis of Mixed Effects (FLAME) from the FSL software package, where a mixed effect model was carried out, and the group-level statistical parametric maps were thresholded (z > 2.3, corrected cluster significance threshold of p = 0.05, thresholdfree cluster enhancement; Gaussian random field method). As the oddball EEG STV regressor was the primary regressor of interest (i.e., the regressor indicative of task-relevant processing),

we only used cortical regions whose BOLD signal covaries with this particular regressor in the subsequent analyses.

Salience processing node definition The oddball EEG STV related GLM statistical maps at each time of interest from the STV EEG-informed fMRI analysis were extracted for defining the nodes associated with the processing of oddball trials. At the peak voxel of each group-level significant cluster, a spherical region of interest (10 mm radius) centered on the voxel was generated. Centroid of peak locations was used for regions involved in more than one temporal windows (i.e. IS1, rSPL, and mPFC-SMA). After excluding one cluster with the peak voxel outside of the brain mask, ten ROIs were included for the subsequent analyses. The neuroanatomical localizations of the nodes were referred to the Human Connectome Project Multi-Modal Parcellation (HCP-MMP) (Glasser et al., 2016). Specifically, to alleviate intersubject variability in the cortical surface reconstruction, instead of mapping the HCP-MMP cortex parcellation to the volumetric space, the ROI masks in each subject's native structural space were projected to the subject's cortical surface. After surface-based spatial normalization to the FreeSurfer fsaverage template cortical surface (Fischl et al., 1999), a majority vote was caried out across subjects to obtain the group-level ROI surface areas, which were compared to the HCP-MMP parcellation for the naming of the anatomical locations of the nodes.

SN, DMN, and DAN node definition The locations of the nodes in the salience network, default mode network, and dorsal attention network were defined with the HCP-MMP atlas. The SN comprised three nodes: right and left anterior insula (AI) (each side includes area anterior agranular insular complex and middle insular area) and dorsal anterior cingulate cortex (ACC)

(includes area dorsal 32, anterior 32 prime, and p32 prime; details of area naming in (Glasser et al., 2016)). The DMN comprised five nodes: posterior cingulate cortex (includes RSC, 23d, 23c, d23ab, v23ab, 31a, 31pv, 31pd, POS1, POS2, 7m, DVT, ProS), precuneus (includes PCV), right and left angular gyrus (each side includes PGi, PGs, and PGp), and medial prefrontal cortex (includes 8BM, 9m, 10r, and 10v). The DAN comprised four nodes: right and left SPL (each side includes LIPv, LIPd, VIP, AIP, MIP, 7PC, 7AL, 7Am, 7PL, 7Pm, IP0, IP1, and IP2), and right and left frontal eye fields. The HCP-MMP atlas was transformed to each subject's cortical surface through surface-based registration using FreeSurfer. Then, the selected ROI surface areas were projected into the volumetric space. The ROI masks were warped into the MNI152 template space with the previously estimated registration parameters. A majority vote was caried out across subjects to obtain the group-level ROI masks. After thresholding the ROI masks (0.5 overlap rate across subjects), we extracted a weighted center of gravity for each ROI region. Similar to the previous analysis, a spherical ROI (10 mm radius) centered on that voxel was generated. Finally, these twelve nodes were used for the subsequent EEG effective connectivity state-space modeling. Details of the SN, DMN, and DAN nodes are illustrated in the Figure 3.6.

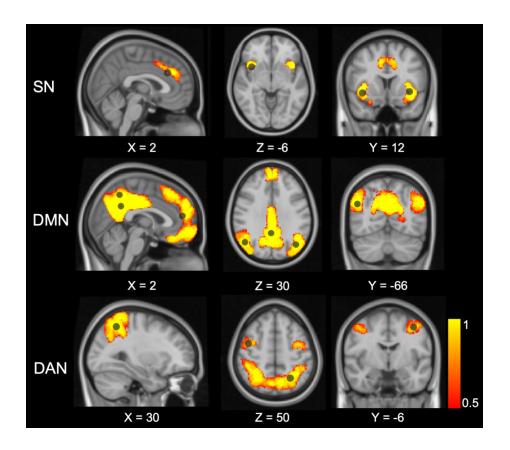


Figure 3.6: Network nodes definition with HCP-MMP atlas. The nodes (circles) of the SN, DMN, and DAN are overlaid with the selected network areas from the HCP-MMP atlas and the MNI152 brain image. The group-level region of interest masks (illustrated as spatial distribution maps) were obtained from majority vote across subjects.

fMRI functional connectivity analysis To control for physiological and motion-related noise, we regressed out motion-related nuisance signals from the preprocessed fMRI data (motion parameters included six standard head motion parameters, their temporal derivatives, and the squares of the above twelve motion parameters), as well as the signals in the left and right hemisphere white matter and lateral ventricles. To circumvent the error in spatial normalization and smoothing, we extracted the BOLD time series of the regions of interest (ROIs) in each subject's native functional EPI space. The ROI masks were transformed and warped into the subjects' EPI functional space with the estimated registration parameters. For each ROI, only the

grey matter BOLD signal was extracted by computing the intersection between the ROI masks and the grey matter mask. And we extracted a single BOLD time series from each ROI by averaging the time series of all the voxels within the intersected mask. No spatial smoothing was carried out. Before computing the FC, to remove the effects of the task, we regressed out taskevoked activations (both standard and target) from the ROIs BOLD signals. In the seed-based FC analysis for network localization, we used a mixed effects model. The first-level seed-based FC was calculated based on the Pearson correlation between the time series of each ROI and the time series of each voxel in the brain. Then, each subject's FC map was transformed into z-score with Fisher's Z transformation. And the FC z-score map was thresholded at p < 0.01. In the group-level, one sample student's t-test was performed to obtain the significant seed-based FC map of each ROI (p < 0.001 uncorrected). Similarly, in the node-by-node FC analysis, the firstlevel FC was computed based on the Pearson correlation across the time series of ROIs. Then, the FC matrix was transformed into z-score, and carried out to the group-level one sample student's t-test to obtain the significant FC matrix across ROIs (p < 0.05 uncorrected). To assess functional connectivity between the locus coeruleus and salience processing nodes, we localized the LC in each subject's functional space with a predefined LC atlas (Keren et al., 2009) and the subject's TSE image, and then the LC BOLD signal was extracted. Specifically, we first performed a rough localization by estimating the spatial range of the LC location in each subject's structural T1-weighted space, where a statistical criterion was used along with the TSE image intensity spatial distribution and the LC atlas. Then, the TSE image intensity within the estimated range was transformed into the subject's functional EPI space for a precise localization of the LC. The LC BOLD signal was extracted by averaging the voxel-wise BOLD time series, weighted by the TSE image intensities. Details are in (He et al., 2021). Functional connectivity

was computed with Pearson correlation between the BOLD signals extracted from the LC and salience processing nodes (mixed effect, p < 0.05 uncorrected).

EEG effective connectivity analysis: state-space modeling of the latent neural activity A state-space model was used to infer the latent brain dynamics across the nodes. To infer the activity in the EEG source space, a volumetric source model was used, where EEG sources (denoted as  $x_t$  at time t) are assumed to be uniformly distributed on a 3D grid inside the brain. Given the observations of the scalp EEG measurements  $y_t$ , a linear EEG forward model was used:  $y_t = Lx_t + e_t$ , where L is the lead field matrix and  $e_t$  is a Gaussian channel noise vector. We defined the latent state variables as  $s_t$ , where  $x_t = Gs_t + \epsilon_t$ , G is a binary indicator matrix, and  $\epsilon_t$  is a Gaussian noise vector. The influences across the latent states of neural dynamics were modeled as a multivariate autoregressive (MVAR) process as  $s_t = As_{t-1} + \sum_{k=1}^K B^k \, m_t^k s_{t-1} + \sum_{k=1}^K a_t \,$  $Du_t + \omega_t$ , where A is the intrinsic connectivity matrix,  $B^k$  is the  $k^{th}(k = 1, 2, ... K)$  modulatory connectivity matrix,  $m_t^k$  is the modulatory input,  $u_t$  is the external input, D is a diagonal matrix denotes the strength of  $u_t$ , and  $\omega_t$  is a Gaussian state noise vector. As for the model inference, the mean-field variational Bayesian approximation was used to make inference on the posterior distributions of the latent space variables and model parameters, during which the evidence lower bound was maximized. The model is described in detail elsewhere (Tu et al., 2019). In this study, we first used the ten salience processing nodes defined from the STV EEG-informed fMRI analysis results. Then, another model was fit with the twelve nodes of SN, DAN, and DMN defined from the HCP-MMP atlas. The ROIs were transformed into each subject's native structural space. The state-space model was fit to each run separately. The modulatory inputs were modeled as a unit height boxcar function with a sequence of events (one each for targets

and standards). Here, the model evidence lower bound (ELBO) was also used to quantify the quality of the model fitting. For the data of the runs failed in model fitting, we excluded those runs from subsequent analyses. Specifically, 11 out of 90 runs failed in the model fitting with salience processing nodes, and 7 out of 90 runs failed in the model fitting with SN, DAN, and DMN nodes. The estimated posterior distributions of model parameters in the first-level analysis were summarized for group-level Bayesian posterior inference using Bayesian parameter averaging (BPA) (Neumann and Lohmann, 2003), which computes a group-level joint posterior probability for the effect of interest. Compared to the conventional statistical null hypothesis significance tests (NHST), the Bayesian posterior inference is considered more robust as the influence from each run is weighted by the precision. The significant group-mean EC was estimated, where a posterior probability criterion of  $\alpha < 0.05$  (Bonferroni correction) was used to threshold the group-level posterior distribution for the inference of significant EC.

Brain and pupil correlation analysis To assess the relationship between the network-level interactions and pupillary response, we characterized the network-level connectivity in the positive and negative connections. Specifically, we defined positive and negative network interaction strength as the sum of all positive and negative connection parameters from one network node set to the other network node set (or to itself as self-connection network strength), respectively. And we also computed the mean TEPR across all the oddball trials for each subject. Therefore, we performed a correlation analysis across all subjects between the network interaction strength and the mean TEPR (Pearson correlation). As a control analysis, we also regressed out the median RT and the mean ELBO from the mean TEPR and network interaction strength, respectively, before performing the same analysis across subjects.

## 3.3.3 Results

All subjects responded to the task correctly with an accuracy of 99.4%  $\pm$  0.1% (mean  $\pm$  SD; SD, standard deviation) in detecting oddballs, and the response time (RT) is 403.5  $\pm$  66.9 (mean  $\pm$  SD) ms.

Pupillometry analysis We used an MRI-compatible eye-tracking camera to track pupil diameter fluctuations in parallel to simultaneous recordings of EEG and fMRI which measured brain activity. Pupil diameter data were then preprocessed and epoched (see Section 3.3.2 for details). The stimuli-locked grand average pupil diameter fluctuations are shown in Figure 3.7. We observed a slow pupil dilation evoked by the target oddball stimuli peaking around 1.4 s after the stimulus. To quantify the pupil dilation elicited by the salient stimuli, we extracted the maximum percentage pupil diameter change within each trial as task-evoked pupillary response.

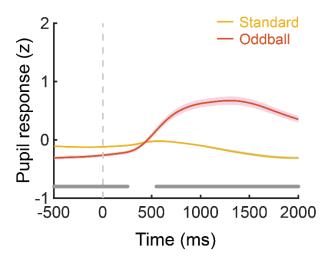


Figure 3.7: Stimuli-locked pupillary response. The z-scored pupil diameter fluctuations from 500 ms before the stimulus to 2000 ms following the stimulus were averaged across subjects for the oddball (red) and standard (yellow) stimuli. The shaded bands represent standard error, and the bottom gray line indicates significant difference

(Student's t-test, p < 0.001) between the pupil diameter evoked by the oddball and standard stimuli.

Single-trial EEG-informed fMRI analysis To identify the neural correlates involved in the salience processing cascade, we performed a single-trial EEG-informed fMRI analysis. Briefly, this method extracts the EEG components discriminating target versus standard trials at different temporal windows spanning the trial, and these are used to map the temporally evolved brain activities that are correlates of salience processing using the fMRI data. The area under the receiver operating characteristic curve (AUC) was used to evaluate the performance of the single-trial discrimination, and the AUC value is above 0.75 between 200 to 700 ms. More details are in the Methods Section 3.3.2 and Figure 3.5. As a sanity check, traditional EEG stimulus-locked ERP and traditional fMRI analysis results are included in the Figure 3.8. and Figure 3.9. We observed the P300 component with a peak around 390 ms in the ERP analysis, and regions in the DAN, SN, visual and auditory cortex, S1, and subcortex were identified as significant clusters in the traditional fMRI analysis of oddball effects. In the EEG-informed fMRI analysis, from the resulting group-level whole-brain BOLD activation maps, we identified significant clusters (p < 0.05, cluster corrected) at specific windows as shown in Figure 3.10A. These results revealed brain regions associated with salient stimuli processing: left superior parietal lobule (ISPL) (225 ms; positive cluster), left S1 (IS1) (250, 275, 350, and 375 ms; positive cluster), left orbitofrontal cortex (IOFC) (375 ms; negative cluster), left inferior parietal lobule (IIPL) (375 ms; negative cluster), left frontal operculum and temporal pole (600 ms; negative cluster), right primary motor cortex (rM1) (225 ms; positive cluster), right secondary visual cortex (rV2) (275 ms; positive cluster), right SPL (rSPL) (275 and 300 ms; positive cluster), right OFC (rOFC) and inferior frontal cortex (rIFC) (375 ms; negative cluster), and

supplementary motor area (SMA) and medial prefrontal cortex (mPFC) (400, 425, and 600 ms; negative cluster). These results indicate a coordinated task-related neural cascade, representing the spatiotemporal dynamics of the neural correlates in salience processing.

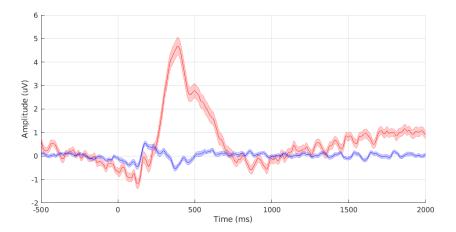


Figure 3.8: Stimulus locked event-related potential at the Pz electrode for the standard (blue) and oddball (red) trials, from 500 ms pre-stimulus to 2000 ms post-stimulus. The solid lines denote the group mean, and the shaded areas denote the standard error across subjects.

The P300 component was observed with a peak around 390 ms.

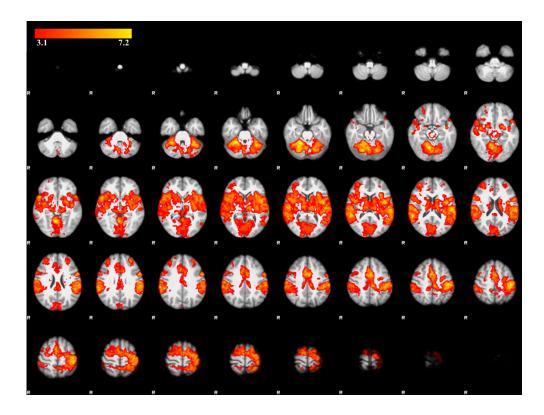


Figure 3.9: Axial slices of the thresholded group-level significant activations in the traditional fMRI analysis of the oddball effects (contrast as oddball versus standard stimuli). The z-statistic maps were displayed on top of the MNI152 template brain image. FMRIB's Local Analysis of Mixed Effects (FLAME) from the FSL software package was used for the group-level statistical inference. The group-level statistical parametric maps were thresholded with z > 3.1 and corrected cluster significance threshold of p = 0.05 (Gaussian random field method). Regions in the dorsal attention network, salience network, visual and auditory cortex, primary somatosensory cortex, and subcortex were identified as significant clusters. Please be noted that only the significant positive effects are shown here, and we did not observe any significant negative effects in the regions of the default mode network. The 'R' in the figure denotes right side of the brain.

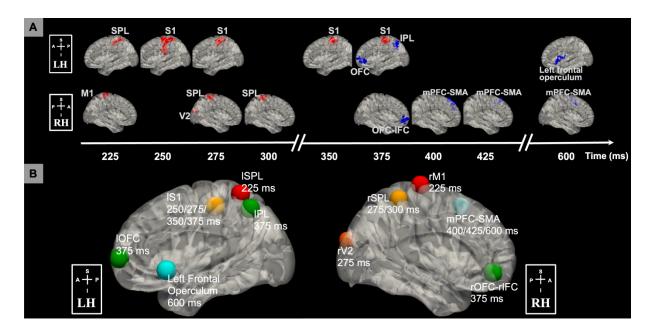


Figure 3.10: Neural correlates of salience processing defined with the EEG single-trial variability (STV) informed fMRI analysis. (A) Timing diagram showing significant grouplevel activation clusters (p < 0.05 cluster-wise multiple comparison correction). STV in EEG temporal components discriminating the target versus standard trials was used to map the spatiotemporally distributed BOLD fMRI correlates spanning the trial. EEG STV information was incorporated as BOLD predictors in voxel-wise general linear model (GLM) analysis of fMRI, controlling for the variance due to the presence of stimuli and response time (RT). Cluster colors denote positive (red) and negative (blue) effects. Time is relative to stimulus onset. (B) Definition of salience processing nodes. Each node is a sphere centered on the peak voxel of the group-level STV EEG-informed fMRI analysis results. Centroid of peak locations was used for regions involved in more than one temporal windows. Node colors denote timing of involvement in the trial from early to late (temporal order: red, orange, yellow, green, and blue). All clusters and nodes were overlaid on a 3D Montreal Neurological Institute (MNI) 152 brain pial surface for visualization. BOLD, blood-oxygen-leveldependent; RH, right hemisphere; LH, left hemisphere; A, anterior; P, posterior; S, superior; I inferior; SPL, superior parietal lobule; M1, primary motor cortex; S1, primary somatosensory cortex; V2, secondary visual cortex; OFC, orbitofrontal cortex; IPL, inferior parietal lobule; IFC, inferior frontal cortex; mPFC, medial prefrontal cortex; SMA, supplementary motor area.

**Network organization of brain regions associated with salience processing** Following this observed neural cascade associated with salience processing, a natural question we asked was about the organization of these spatiotemporally distributed regions. Specifically, we aimed to assess the network organization and connectivity between these brain regions. Thus, we defined

10 nodes: ISPL [x = -34, y = -52, z = 64; Montreal Neurological Institute (MNI) coordinates], IS1 (x = -46, y = -28, z = 52), IOFC (x = -40, y = 60, z = 4), IIPL (x = -48, y = -60, z = 50), left frontal operculum and temporal pole (x = -54, y = 16, z = -6), rM1 (z = 18, z = -22, z = 76), rV2 (z = 8, z = -94, z = 22), rSPL (z = 38, z = -42, z = 60), rOFC-rIFC (z = 42, z = 46, z = -8), mPFC-SMA (z = 4, z = 56) as shown in Figure 3.10B (see Section 3.3.2 for details of salience processing node definition).

Given the emerging evidence that indicates the relevance between task activation and the intrinsic network organization of the brain (Cole et al., 2016), we hypothesized that the previously identified nodes might represent organized underlying brain networks involved in salience processing. To test this hypothesis, a network localization approach was performed to map the brain regions functionally connected with each node (see Methods Section 3.3.2 for details; results in Figure 3.11). In the earliest time windows (225 to 275 ms), as expected, node rM1 was localized within the sensory motor network, and rV2 was part of the visual network. ISPL, rSPL, and IS1, which are spatiotemporally heterogeneous regions in the salience processing cascade, were mapped to a single brain network, i.e. DAN. Similarly, IOFC, rOFCrIFC, and IIPL, which are all correlated with the EEG discriminating components at 375 ms poststimulus, fell within the executive control network (ECN) (Seeley et al., 2007). Finally, in the latest time windows (400 to 600 ms), we found the nodes correlated with the late discriminating components, i.e. mPFC-SMA, left frontal operculum and temporal pole, were part of the SN. Overall, this observation suggests that these distributed nodes are spatially organized into intrinsic brain networks, indicating that the temporal evolution of different task activation regions (Figure 3.10A) spanning the trial might be supported by a specific set of brain networks (Figure 3.11).

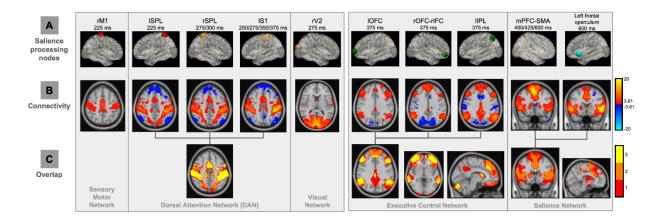


Figure 3.11: Network localization approach to map functional networks underlying salience processing nodes. (A) BOLD signals from the nodes (intersected with the grey matter mask) were extracted, controlling the nuisance signals (motion-related, ventricle and white matter signals). (B) Group-level functional connectivity (FC) results of each node (t-value, mixed-effect, p < 0.001 uncorrected). Seed-based FC analysis (with the task-related variability regressed out) was used to map network of regions connected to each node location. Colors denote positive (red) and negative (blue) correlations. (C) Spatial overlaps in the FC maps of each node identified spatial network organizations of salience processing nodes. Colors represent the number of FC maps overlapped. ISPL and rSPL, left and right superior parietal lobule; rM1, right primary motor cortex; IS1, left primary somatosensory cortex; rV2, right secondary visual area; IOFC and rOFC, left and right orbitofrontal cortex; IIPL, left inferior parietal lobule; rIFC, right inferior frontal cortex.

Following these results that distinct nodes might fall within a common network, our next objective was to directly examine the functional connectivity between the nodes. As shown in Figure 3.12 (p < 0.05, uncorrected), in line with the previously observed spatial organization of the nodes revealed by network connectivity (Figure 3.11), we found strong connections across the nodes within each network. For example, ISPL, rSPL, and IS1 showed a stronger within network (i.e. nodes of DAN) connectivity compared to their connections with other nodes. Furthermore, the functional connectivity results clearly identified three distinct groups of the nodes, organized by the EEG discriminating component time windows, indicating a temporal organization of the nodes. Thus, to assess the brain networks involved in the task-related neural

cascade, we defined three intrinsically connected salience processing networks, i.e. early-time (nodes: ISPL, rM1, rV2, rSPL, and IS1), middle-time (nodes: IIPL, IOFC, and rOFC-rIFC), and late-time (nodes: mPFC-SMA, left frontal operculum and temporal pole) networks.

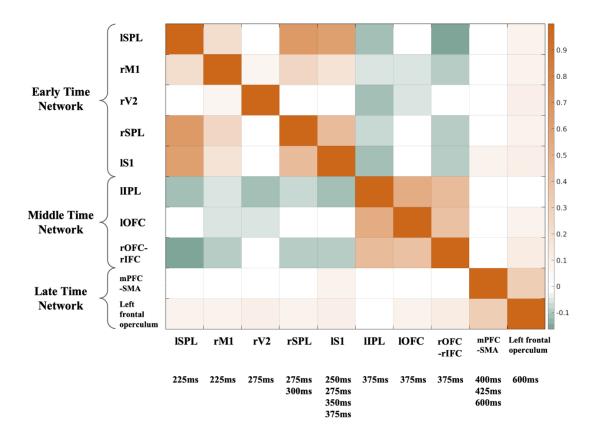


Figure 3.12: Functional connectivity (FC) across salience processing nodes (group averaged z-score, mixed-effect, p < 0.05 uncorrected). fMRI BOLD signals from the nodes (intersected with the grey matter mask) were extracted, controlling the nuisance signals (motion-related, ventricle and white matter signals). Pearson's correlation was calculated between BOLD signals from the nodes (with the task-related variability regressed out). FC results identified three distinct groups of the nodes, organized by the EEG discriminating component time windows, indicating a temporal network organization of the nodes: 1) early-time network includes ISPL and rSPL, rM1, rV2, and IS1; 2) middle-time network includes IOFC and rOFC, IIPL, and rIFC; 3) late-time network includes mPFC, SMA, left frontal operculum and temporal pole.

Modulated effective connectivity by salience processing In the functional connectivity analyses of fMRI data described above, we examined the spatial organizations of the salience

processing nodes. Our next step was to investigate the temporal dependence and directional interaction between these nodes, by fitting EEG data with a state-space effective connectivity (EC) model (see Methods Section 3.3.2 for details). In the group-level analysis, results for the significant salient stimuli modulated EC (Bayesian parameter averaging;  $\alpha < 0.05$ ; Bonferroni corrected) are shown in Figure 3.13, with positive and negative connections shown in Figure 3.14. To quantify the connection strength of each node, we computed the total connection strength (Figure 3.15), which is the sum of all the unsigned connection parameters (afferent, efferent and self-connection) associated with the node. These results showed that the mPFC-SMA and ISPL have the highest afferent and efferent connection strength, respectively, suggesting that the mPFC-SMA and ISPL are the hubs in the processing of salient stimuli.

## **Oddball Modulated Effective Connectivity** 0.2 ISPL rM1 0.1 rV2 rSPL IS1 -0.1 IIPL -0.2 **IOFC** rOFCrIFC -0.3 mPFC -SMA Left frontal -0.4 operculum ISPL rM1 rV2 rSPL IS1 IIPL **IOFC** mPFC Left frontal rOFC -SMA operculum -rIFC

Figure 3.13: Group-level mean effective connectivity modulated by the oddball stimuli between salience processing nodes (Bayesian parameter averaging;  $\alpha$  < 0.05; Bonferroni corrected). Please be noted the results here reflect mean group effect. The orange and blue color represents positive and negative effective connectivity, respectively.

From

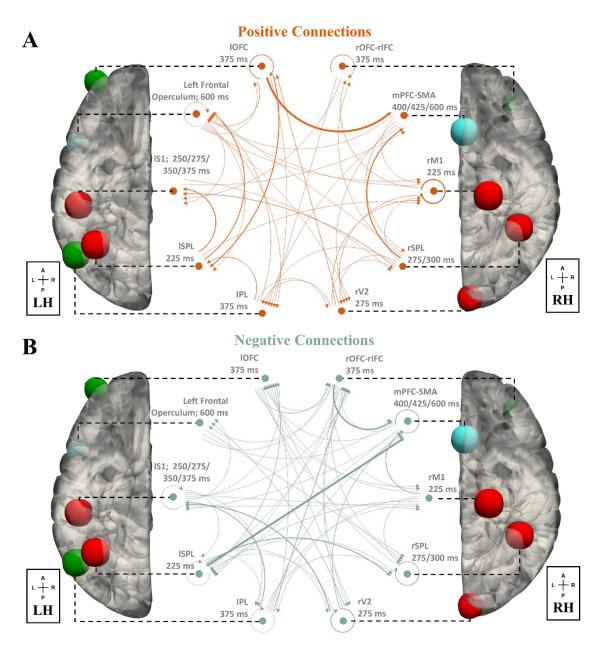


Figure 3.14: Effective connectivity (EC) across salience processing nodes (Bayesian parameter averaging,  $\alpha$  < 0.05, Bonferroni corrected). (A) positive EC, (B) negative EC. By leveraging the high temporal information in the EEG data, an effective connectivity statespace model was fit with the salience processing nodes. The arrow and thickness of the connecting lines correspond to the directionality and strength of EC, respectively. Dominant influence is observed in the connections of ISPL, IOFC and mPFC-SMA. The results here reflect mean group effect. Node colors denote timing of involvement (early-time: red; middle-time: green; late-time: blue).

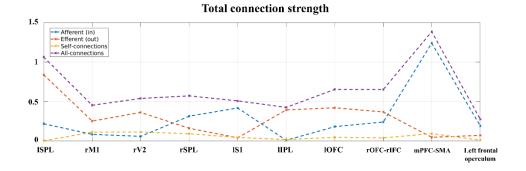


Figure 3.15: Total connection strength of each salience processing node. With the effective connectivity results, all the unsigned connection parameters (efferent, afferent and self-connection) associated with the node were summed up to compute the total connection strength. The results suggest that the ISPL and mPFC-SMA have the strongest total connection strength, indicating their roles as hubs in the processing of salience stimuli.

Relationship between effective connectivity and pupillary response Having demonstrated the directional interaction between the nodes modulated by salient stimuli, we next investigated the network-level EC, based on previously defined salience processing networks. To characterize the network-level connectivity in the positive and negative connections, for each subject, we computed positive and negative network connection strength as the sum of all positive and negative connection parameters from one network node set to the other network node set (or to itself as self-connection network strength), respectively. Next, we assessed the relevance of network-level EC strength to TEPR, by computing the Pearson correlation between positive (or negative) network connectivity strength and TEPR at the between-subject level. The significance level was set as  $\alpha < 0.05$  with Bonferroni correction. We found a significant correlation between the late-to-early positive network connectivity strength and TEPR (r = 0.6352, p = 0.0035; Figure 3.16A; after controlling RT and ELBO r = 0.6347, p = 0.0035; ELBO was used as an evaluation of model fitting), whereas other network interactions did not show a significant correlation. In detail, for the positive connections, the other network connectivity strength did not

show any statistically significant relationship with TEPR (Early-to-early: r = 0.4290, p = 0.0668; Early-to-middle: r = 0.3708, p = 0.1181; Early-to-late: r = 0.0916, p = 0.7091; Middle-to-early: r = 0.1163, p = 0.6354; Middle-to-middle: r = 0.1219, p = 0.6191; Middle-to-late: r = 0.1058, p = 0.6665; Late-to-middle: r = 0.1404, p = 0.5665; Late-to-late: r = -0.1568, p = 0.5214). For the negative connections, none of these network connections strength showed significant correlation with TEPR. The observed significant relationship (between the late-to-early positive network connectivity strength and TEPR) still holds at the between-run level, if the runs were pooled across all subjects (r = 0.4124, p = 0.0002). This outcome suggests that the TEPR is associated with the positive network couplings from the late-time network to the early-time network in the processing of salient stimuli, indicating a TEPR associated brain networks excitatory feedback (late-to-early) signal.

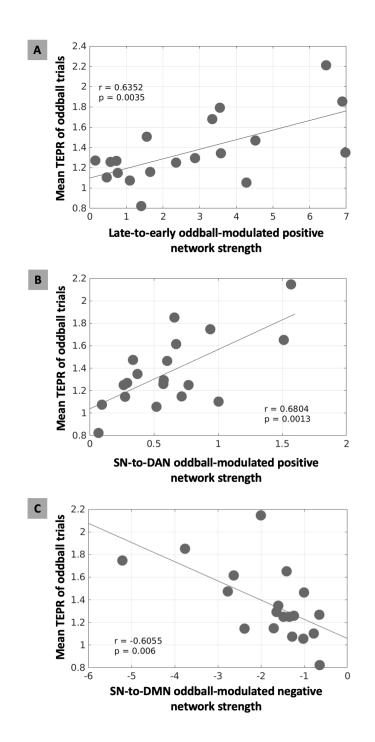


Figure 3.16: Brain-pupil relationships of the cortical network-level effective connectivity (EC) and task-evoked pupillary response (TEPR) in salience processing. (A) The oddball-modulated positive EC strength from the late-time to early-time network correlated with higher TEPR of oddball trials (p < 0.0035). In (B) and (C), to test the associations between pupil measurements and the triple-network model (SN, salience network; DAN, dorsal attention network; DMN, default mode network), we computed EC across nodes of these networks. (B) The oddball-modulated positive EC strength from SN to DAN correlated with

higher TEPR of oddball trials (p < 0.0013). (C) The oddball-modulated negative EC strength from SN to DMN correlated with higher TEPR of oddball trials (p < 0.0060).

**Involvement of locus coeruleus in salience processing** Given substantial evidence that pupil diameter is tightly coupled to the neuronal activity in the LC (Aston-Jones and Cohen, 2005; Joshi et al., 2016), pupil diameter has been used as an index of the LC activity (Gilzenrat et al., 2010). With the observed correlation between late-to-early network feedback signal and TEPR (Figure 3.16A), we therefore hypothesized that the LC might play a role in the interactions between large-scale cortical networks. To test the involvement of the LC in salience processing, we first examined the functional connectivity between the LC and salience processing nodes (see Section 3.2.2 for details of the LC localization and BOLD signal extraction). The LC showed significant functional connectivity with ISPL, IS1 and mPFC-SMA (ISPL: t = 2.64, p = 0.017; 1S1: t = 3.80, p = 0.001; mPFC-SMA: t = 3.15, p = 0.006), however, there were no significant results between the LC and the other salience processing nodes (rM1: t = 0.73, p = 0.476; rV2: t = 0.73, p = 0.476; rV2: t = 0.73= -1.15, p = 0.267; rSPL: t = 1.48, p = 0.156; IIPL: t = -0.45, p = 0.660; IOFC: t = -0.56, p = 0.579; rOFC-rIFC: t = -1.92, p = 0.071; Left frontal operculum: t = 0.96, p = 0.351). As a sanity check, whole-brain temporal signal-to-noise ratio analysis was performed with results in Figure 3.17, and the seed-based whole-brain FC results of the LC are included in Figure 3.18. With the functional couplings to the nodes of both early-time and late-time networks, this result indicates that the LC might be an important factor in the directional interactions between these two networks. This result is also consistent with the observation that ISPL and mPFC-SMA are the hubs in the modulated EC, rendering their importance in salience processing.

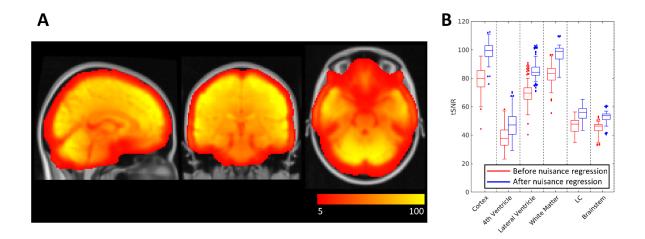


Figure 3.17: Whole brain temporal signal-to-noise ratio (tSNR) analysis was performed to assess the fMRI signal quality especially for the BOLD signal in the LC. The tSNR was computed for each voxel, by dividing the mean over the standard deviation. (A) Group-level mean tSNR map of preprocessed fMRI data (no spatial smoothing). The tSNR map of each run was spatially normalized into the MNI152 space, and then was averaged across all the runs of subjects. (B) Quantitative analysis and boxplot of tSNR distributions across runs in each ROI. The color denotes the tSNR before (red) and after (blue) the nuisance signal regression (motion parameters and BOLD signals in the 4th ventricle and the left and right hemisphere white matter and lateral ventricles). Before the functional connectivity analysis of the LC, we regressed out the BOLD signal in the 4th ventricle. The tSNR was computed for each voxel in the subject's native functional space, and then was averaged within the ROI (segmented with FreeSurfer). The LC two standard deviation template was used to delineate the LC ROI (Keren et al., 2009). The tSNR in the LC is above the standard cut-offs (tSNR > 30) (Grueschow et al., 2021).

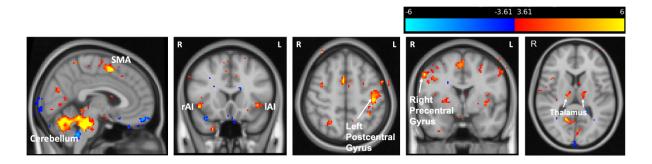


Figure 3.18: T-statistic maps of the LC seed-based whole-brain functional connectivity results. We used a mixed effects model for group inference. Each subject's FC map was transformed into z-score with Fisher's Z transformation. And the FC z-score map was thresholded at p < 0.01. In the group-level, one sample student's t-test was performed to obtain the significant seed-based FC map of the LC (p < 0.001 uncorrected). Significant

clusters were identified in the cerebellum, supplementary motor area (SMA), right and left anterior insula (AI), left postcentral gyrus, right precentral gyrus, and thalamus.

Following these results on the involvement of the LC with the late-to-early network feedback signal and the nodes of both DAN and SN (ISPL, IS1 and mPFC-SMA), and given the vast amount of literature on the triple-network model (Menon, 2011) of the DAN, SN, and default mode network, the final question we asked was whether this feedback signal reflects the network switching function of the SN, and whether pupil-indexed LC system is associated with the interactions between these three large-scale cortical networks. Thus, we fit the EEG data with the effective connectivity state-space model including the nodes of SN, DAN, and DMN, defined by the HCP-MMP (Human Connectome Project Multi-Modal Parcellation) atlas (Glasser et al., 2016) (see Section 3.3.2 and Figure 3.6 for details of SN, DAN, and DMN nodes definition; EC results in Figure 3.19). The significance level was set as  $\alpha$  < 0.05 with Bonferroni correction. As expected, we found a significant positive correlation between the salient stimuli modulated SNto-DAN positive network EC strength and TEPR (r = 0.6804, p = 0.0013; Figure 3.16B; after controlling RT and ELBO: r = 0.5949, p = 0.0072). This finding aligns with our previous results on the involvement of the LC in the late-to-early network feedback signal and the nodes of both DAN and SN. Interestingly, we also observed a significant negative correlation between the salient stimuli modulated SN-to-DMN negative network EC strength and TEPR (r = -0.6055, p =0.0060; Figure 3.16C; after controlling RT and ELBO: r = -0.6820, p = 0.0013). These significant relationships still hold at the between-run level, if the runs were pooled across all subjects (SN-to-DAN connection: r = 0.4051, p = 0.0002; SN-to-DMN connection: r = -0.2311, p = 0.0356). To eliminate the possibly alternative models that differ in the direction of information flow between SN, DAN, and DMN, we performed the same analysis between TEPR

and all the other inter-network connections, and there is no significant relationship between them. In detail, for the positive connections, whilst the SN-to-DAN network strength showed a significant correlation with TEPR, the other network connectivity strength did not show any statistically significant relationship with TEPR (DAN-to-DMN: r = -0.2710, p = 0.2616; DAN-to-SN: r = -0.0800, p = 0.7447; DMN-to-DAN: r = 0.4827, p = 0.0363; DMN-to-SN: r = 0.0570, p = 0.8167; SN-to-DMN: r = 0.3780, p = 0.1106). For the negative connections, whilst the SN-to-DMN network strength showed a significant correlation with TEPR, the other network connectivity strength did not show any statistically significant relationship with TEPR (DAN-to-DMN: r = 0.0244, p = 0.9209; DAN-to-SN: r = 0.0864, p = 0.7248; DMN-to-DAN: r = -0.4895, p = 0.0334; DMN-to-SN: r = -0.2279, p = 0.3478; SN-to-DAN: r = -0.2849, p = 0.2370). These results are in line with the previous studies on the function of SN for the switching between anticorrelated networks (Menon and Uddin, 2010; Uddin, 2015; Y. Zhou et al., 2018). In summary, the results indicate that the LC is involved in the switching between cortical networks.

## **Oddball Modulated Effective Connectivity**

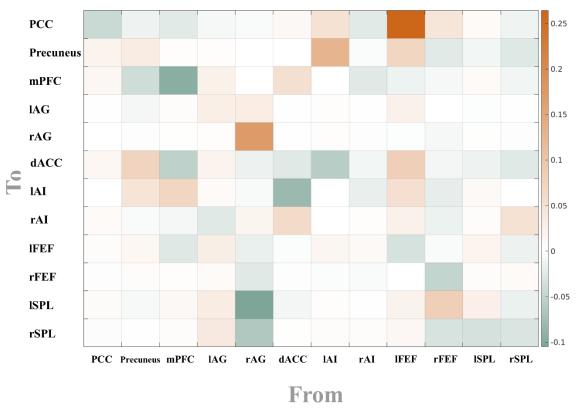


Figure 3.19: Group-level mean effective connectivity modulated by the oddball stimuli between the nodes of DMN, SN and DAN (Bayesian parameter averaging;  $\alpha$  < 0.05; Bonferroni corrected). The orange and blue color represents positive and negative effective connectivity, respectively.

## 3.3.4 Discussion

Spatiotemporal brain networks in salience processing We used EEG-informed fMRI analysis to map the spatiotemporal dynamics of neural substrates in salience processing. Specifically, the STV temporal information in the EEG was extracted at different time windows spanning the trial to explain the variance in the fMRI signal. This approach has been widely used to study a broad range of cognitive functions and human behaviors (Philiastides et al., 2021; Walz et al., 2013). Compared to conventional fMRI analyses, EEG-informed fMRI analysis

allows us to temporally dissociate the stimuli-evoked brain activation, or even identify regions absent in the conventional analyses (canceled out due to a temporal integration effect) (Goldman et al., 2009; Philiastides et al., 2021). This work extends this approach by introducing the functional connectome into the framework for mapping the underlying spatiotemporal network organizations of these neural substrates. Functional connectome has been shown as a reliable approach in elucidating intrinsic brain organizations (Fox et al., 2005a) and modeling cognitive task activation (Cole et al., 2016). In this study, based on the STV EEG-informed fMRI analysis and functional connectome network localization, we observed a spatiotemporal intrinsic network organization of the neural substrates in salience processing (Figure 3.20). The involvement of these nodes and networks in an auditory oddball task is consistent with prior studies: DAN, motor network, ECN and SN (Kim, 2014), and visual network (Goldman et al., 2009). In this study, the FC analysis was used only to map network organizations of brain areas, instead of making inference on the interactions, due to its correlation nature and the low temporal resolution of fMRI data. Thus, we performed EC analysis with EEG data. Comparison between the functional and effective connectivity with simultaneous EEG-fMRI is interesting, however, it is out of the scope of this study.

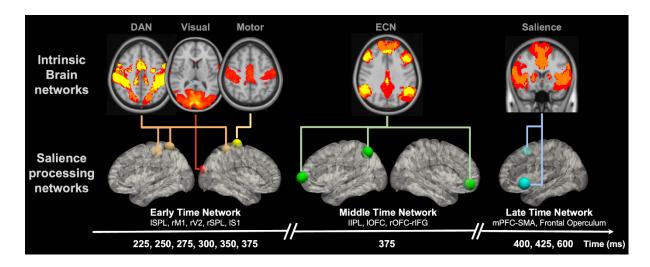


Figure 3.20: Neural cascades of salience processing and the spatiotemporal network organizations of salience processing nodes. Previous seed-based and node-by-node functional connectivity results suggest both spatial and temporal network organizations of the identified salience processing nodes, respectively. We hypothesized that the node-specific involvement of these functional networks might indicate a crucial role of these nodes in the temporally evolved processes of salience signal and the relationships between these networks. ECN, executive control network.

Given these observations, we inferred that the brain flexibly recruited specific nodes of distinct networks at different time windows spanning the trial according to the demand of specific cognitive processes and behavior responses. In the early-time windows, we observed a sustained activation of DAN subsystem from 225 ms to 375 ms, along with the rM1 at 225 ms and rV2 at 275 ms. Literatures have shown that DAN is associated with goal-driven attention and the role of linking them to appropriate motor responses (Corbetta et al., 2008). The observed activation of the early-time network might reflect the functions of these systems in salience processing. For example, the coactivation of rM1 and ISPL at 225 ms might reflect the relationship between DAN and the motor network, and their role in linking stimuli and responses. Based on the previous evidence that DAN exhibits top-down influences on the sensory cortex (Corbetta et al., 2008), we hypothesized that the involvement of the visual

network areas might indicate the modulation of attentional resources distribution (Shomstein and Yantis, 2004). This hypothesis was also supported by the observed self-inhibition EC in rV2 (Figure 3.14B). Similar to the reported temporal components underlying a visual spatial attention task in a Magnetoencephalography (MEG) study (Simpson et al., 2011), we also observed the involvement of ECN nodes (375 ms) right after the early activation of parietal and visual areas. This network's node-specific involvement might indicate a crucial role of these nodes in the network and salience processing. For example, prior studies suggest the existence of common nodes (left orbital frontoinsula, mPFC, and right dorsolateral prefrontal cortex) between the ECN and SN (Seeley et al., 2007). Thus, the observed involvement of the left frontal operculum and mPFC-SMA in the late time might reflect their roles in the relationship between ECN and SN, which might facilitate the temporal transition from ECN to SN in the late time of the trial. Future studies are needed to investigate the specific functions of these nodes in the relationship between brain networks.

Cognitive control in salience processing Based on the anatomical locations of the nodes in the network, ECN and SN have also been named lateral frontoparietal network (L-FPN) and midcingulo-insular network (M-CIN), respectively (Uddin et al., 2019). Previous studies have shown that the ECN/L-FPN and SN/M-CIN are two prominent cognitive control networks, supporting the goal-directed cognition and behavior (Cole et al., 2013; Fair et al., 2007). In these studies, L-FPN and M-CIN were named as frontoparietal network and cingulo-opercular network. To keep the terminology of the brain networks consistent in this study, we referred to ECN/L-FPN and SN/M-CIN following the guidelines in (Uddin et al., 2019). SN (cognitive domain name) and M-CIN (anatomical name) contains these core regions: bilateral anterior

insula and anterior midcingulate cortex. ECN (cognitive domain name) and L-FPN (anatomical name) contains these core regions: lateral prefrontal cortex, anterior inferior parietal lobule, and intraparietal sulcus. ECN/L-FPN and SN/M-CIN are coactivated together as the task-activation ensemble (Seeley et al., 2007) in goal-directed behaviors and tasks. However, converging evidence from the literature indicates distinct roles of ECN/L-FPN and SN/M-CIN in goal-directed behaviors. ECN/L-FPN acts as a flexible coordinator of goal-relevant information (Cocuzza et al., 2020), and may underlie phasic control such as initiates exogenously triggered control, adaptive adjustments, and executive functions (Dosenbach et al., 2007; Sadaghiani et al., 2012). Whereas, SN/M-CIN is related to stable maintenance of task-set (Fair et al., 2007) and tonic alertness (Sadaghiani and D'Esposito, 2015), and has also been proposed a role in lending processing resources to help other goal-relevant networks (Cocuzza et al., 2020).

In the present study, by leveraging STV temporal information in the EEG to tease apart the temporal neural processes in the goal-directed salience processing, we dissociated the stimuli-evoked coactivation of ECN/L-FPN and SN/M-CIN into two distinct temporal components (subsystem of ECN as the middle-time network deactivated at 375 ms, subsystem of SN as the late-time network deactivated during 400-600 ms). Along with this temporal dissociation, ECN/L-FPN and SN/M-CIN seemed to act with distinct roles in the salience processing, where ECN/L-FPN was deactivated preceding the behavior response (group-averaged RT: 404 ms) and the deactivation of SN/M-CIN. And ECN/L-FPN acted as a phasic control (deactivated only at 375 ms), which might provide the rapid control initiation to SN/M-CIN (deactivated starting 400 ms). This is also supported by the EC results that the oddball-modulated EC (Figure 3.13) showed a stronger connectivity strength from the subsystem of ECN/L-FPN to SN/M-CIN (mid-to-late; positive: 0.2523; negative: 0.3145) compared to the

connection from the subsystem of SN/M-CIN to ECN/L-FPN (late-to-mid; positive: 0.0165; negative: 0.1126). These results align with the interactive dual-networks model of ECN/L-FPN and SN/M-CIN in (Dosenbach et al., 2007). This rapid control initiation might be mostly driven by the EC from lOFC to mPFC-SMA, as indicated by the strong connection strength (Figure 3.14A). Whereas, SN/M-CIN was deactivated at multiple time points (400, 425, 600 ms) right after the response, indicating a stable maintenance of tonic alertness, which might facilitate the better detection performance in the next coming trial (Sadaghiani and D'Esposito, 2015). The involvement of SN/M-CIN regions in processing salient stimuli was reported by (Downar et al., 2002, 2000), where the anterior cingulate and the supplementary motor areas had been proposed a role in anticipation of forthcoming stimuli. We propose that the involvement of SN in the late time windows might allow the brain to disengage the current trial and maintain the preparedness for the next upcoming stimulus. As proposed in a single-unit recording study, pre-SMA (mPFC-SMA) is associated with task switching by first suppressing irrelevant task-set and then boosting a controlled response with the relevant task-set (Isoda and Hikosaka, 2007; Sakai, 2008). In the present study, we found mPFC-SMA deactivated starting at 400 ms, which might reflect a suppression or inhibition of the current trial encoded task-set. With the proposed role of pre-SMA (mPFC-SMA) in conflict monitoring (Botvinick et al., 2001; Isoda and Hikosaka, 2007), in the changing environment after the response, its involvement allows the brain to resolve the conflict between the current trial encoded task-set and the new environment, which facilitates task disengagement. This task-set suppressing and boosting role of the SN is consistent with the network switching theory (Menon and Uddin, 2010). It is worth noting that, in the traditional fMRI analysis of oddball effects (Figure 3.9), regions in the SN were identified as significantly activated clusters, whereas, our single-trial variability EEG-informed fMRI analysis results

suggest that the SN was deactivated in response to oddball events in the late window (Figure 3.10 and 3.20). These observations indicate that though the mean response of the SN is stronger for the oddball trials compared to the standard trials, our EEG-informed time-resolved analysis shows that late in the trial, when an oddball is less discriminating from a standard, as measured by EEG, the SN response is stronger to the oddball trial. We believe this result supports the proposed "windshield wiper" role of the SN in the literature (Sadaghiani and D'Esposito, 2015), and a stronger response in the SN might suppress the discriminating processes of the current trial, facilitating task disengagement. However, this hypothesis warrants further investigation. In the anticipation of upcoming inputs, SN may employ such a mechanism to increase preparedness by clearing currently ongoing activity in multiple cortical areas. The present findings provided more evidence for the functions, relationship, and timescales of these two cognitive control networks (i.e. ECN/L-FPN and SN/M-CIN).

Linking networks effective connectivity and pupillary response: LC is associated with network reset The LC-NE system has been proposed to modulate neural gain, attention, and arousal (Aston-Jones and Cohen, 2005). Pupil diameter fluctuations, as a proxy of LC activity (Joshi et al., 2016; Murphy et al., 2014), have been used to investigate how the ascending neuromodulator from the LC-NE system influences the cortex (Murphy et al., 2011). There is growing research on the relationship between brain measurements and pupil diameter, with evidence suggesting that pupil diameter fluctuations are associated with cortical membrane potential activity (McGinley et al., 2015), EEG P300 component of the ERP (Murphy et al., 2011), fMRI BOLD signal in the DMN, SN, thalamus, frontoparietal, visual, and sensorimotor regions (Schneider et al., 2016; Yellin et al., 2015), overall functional connectivity strength

during exploration (Tardiff et al., 2021), and global fluctuations in network structure (Eldar et al., 2013). These findings shed light on the understanding of brain-pupil relationships and cortico-subcortical associations, however, the role of the LC-NE system in the connectivity and interaction between specific brain networks within the context of a goal-driven task (e.g. salience processing) is less well understood. Here, by leveraging the high temporal resolution of the EEG, we used a state-space model for inferring the EC between brain networks involved in salience processing. We observed a very strong relationship between the late-to-early positive network interaction strength and TEPR (Figure 3.16A). In the oddball paradigm with motor response, studies have shown that TEPR reflects not only bottom-up mechanisms but also top-down higher-order processing (Joshi and Gold, 2020; Kim, 2014). Given the directionality of this TEPR-related network interaction, we propose that the phasic LC activity (indexed by TEPR) is associated with a feedback (top-down) signal from the late-time network (nodes of SN) to the early-time network (nodes of DAN, visual, and sensory motor network). Besides the close relationship between the LC activity and pupil diameter fluctuations, SN areas also exhibited close links to the LC-NE system and pupil measurements. The LC-NE system has shown to receive projections from the anterior cingulate cortex and anterior insula (Aston-Jones and Cohen, 2005; Corbetta et al., 2008), and has robust functional connectivity with these SN nodes (Hermans et al., 2011; Mäki-Marttunen and Espeseth, 2021). In an intracranial EEG study (Kucyi and Parvizi, 2020), both the spontaneous and task-evoked activations in the anterior insula are linked to the dynamics of pupillary dilation. The SN and pupil measurements have both been associated with task demands, efforts, difficulty (Beatty, 1982; Vassena et al., 2014), uncertainty and surprise (Joshi and Gold, 2020), conflict and error processing (Critchley et al., 2005), and anxiety (Browning et al., 2015; Seeley et al., 2007). The involvement of SN, as a

subsystem of the ventral attention network (VAN) (Uddin et al., 2019), aligns with evidence showing the involvement of VAN in both bottom-up stimulus saliency and top-down internal goals (Corbetta et al., 2008; Long and Kuhl, 2018).

Even with widespread projections of LC neurons throughout the cortex, recent studies suggested that there are substantial specificity and heterogeneity in the projections (Tardiff et al., 2021; Totah et al., 2019; van den Brink et al., 2019). For example, regions in DAN receive dense LC-NE inputs (Benarroch, 2009). Our functional connectivity analysis suggests that the LC-NE system, with connections to both SN and DAN nodes, might play an important role in the topdown control from SN to DAN along with other early-time network nodes. Our results strongly support the network-reset theory, which proposes that the VAN (SN as a subsystem) marks behavior transitions and facilitates a network reset signal along with the phasic LC-NE activity (indexed by TEPR), to reconfigurate the DAN (part of the early-time network) for settling the brain into another state in the new environment situation (Bouret and Sara, 2005; Corbetta et al., 2008). This theory also aligns with the previous discussions on the synchronized timing of the behavior response/transitions and the deactivation of SN areas, and the proposed preparedness role of the late involvement of SN areas. In light of recent studies in the LC-NE system effects on brain network reconfiguration (Zerbi et al., 2019), more studies are needed to investigate the role of LC-NE system in the interaction between brain networks (Poe et al., 2020; van den Brink et al., 2019).

SN, DAN, and DMN in salience processing: LC plays a role in network switching The anticorrelation between the DAN and the DMN has been characterized as a vital aspect of the human brain functional organization and dynamics (Fox et al., 2005a), with DAN and DMN

controlling environmentally directed and internally directed cognitive processes, respectively (Corbetta et al., 2008; Fox et al., 2005a). Converging evidence suggests that the nodes of the SN are at the apex of the cortical hierarchy between these two anticorrelated networks (Y. Zhou et al., 2018), with a critical role in the dynamic switching between them (Sridharan et al., 2008). A triple network model has been proposed for these three core neurocognitive networks (Menon, 2011), serving as a networks framework for understanding psychopathology (Menon, 2011) and cognitive aging (Tsvetanov et al., 2016). However, the neural mechanisms underlying dynamic switching, and how can the SN have such a wide spread access to DAN and DMN for coordinating the switching between them, are not well understood. Here, along with the close relationship between the SN and the LC-NE system discussed in the previous section, it is plausible to hypothesize that brainstem nuclei, such as the LC, may play a role in the dynamic switching of large-scale brain networks through the release of neuromodulatory neurotransmitters. Neuromodulation models of the LC have been proposed. In the adaptive-gain theory (Aston-Jones and Cohen, 2005; Gilzenrat et al., 2010), the LC receives task utility information from the ACC (SN node) and OFC, producing NE release at cortical target sites and adjusts the gain. The network glutamate amplification of noradrenaline (GANE) model (Mather et al., 2016; Poe et al., 2020) proposed that the SN recruits LC firing to enable NE local concentration modulation, accompanied by in parallel enhancement and suppression of largescale brain networks. In support of our hypothesis, i.e. the LC is associated with the network switching function of the SN, we found that increased TEPR (index of phasic LC activity) is associated with a stronger positive EC from the SN to the DAN, and a stronger negative EC from the SN to the DMN (Figure 3.16). This result confirmed the previous findings that the SN initiates the dynamic switching, and to our knowledge, this is the first study to show the

anticorrelated networks. This suggests a cortico-subcortical integrated network reorganization system, involving both the SN and the LC-NE system in the network reorganization (reset and dynamic switching) between the DAN and DMN (Figure 3.21).

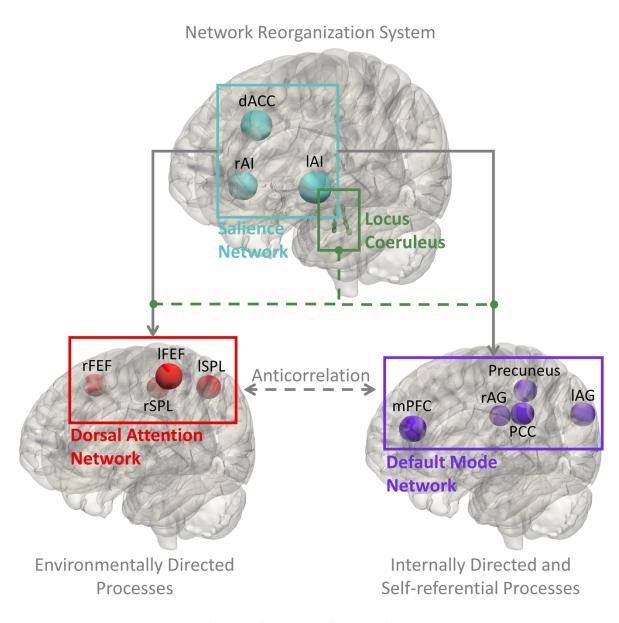


Figure 3.21: Cortico-subcortical integrated network reorganization (CS-INR) system. Previous brain-pupil relationships results aligned with the network switching model of SN in the literature, and also showed the role of the locus coeruleus norepinephrine (LC-NE) system in the network reset and the dynamic switching between anticorrelated networks (SN-to-DAN and SN-to-DMN). In support with the literature (Bouret and Sara, 2005), we

hypothesized that the reset and switching might be modulated by the release of the NE, as an effect of the ascending neuromodulation, which indicates that the SN and LC-NE system might cooperate and share an integrated role in salience processing. dACC, dorsal anterior cingulate cortex; lAI and rAI, left and right anterior insula; lSPL and rSPL, left and right superior parietal lobule; lFEF and rFEF, left and right frontal eye fields; mPFC, medial prefrontal cortex; PCC, posterior cingulate cortex; lAG and rAG, left and right angular gyrus.

Regarding the temporal profiles of the task responses in SN, DAN, and DMN, our results align with several intracranial EEG studies (Kucyi et al., 2020; Raccah et al., 2018), where they found the responses reached the fastest, intermediate, and slowest speed in the DAN, SN, and DMN, respectively. In our study, we also found an earlier involvement of the DAN (starting at 225 ms), preceding the responses in the SN starting at 400 ms. Interestingly, in our previous simultaneous EEG-fMRI study (Walz et al., 2014), we identified significant responses in the DMN at a relatively late time window (525 ms), supporting the temporal order of responses in DAN, SN, and DMN as reported in these intracranial EEG studies. However, these findings in the task-evoked responses do not imply interactions among these networks. In this study, our effective connectivity analyses extend such frameworks of networks' temporal dynamics, by proposing that the network switching signal from the SN to the DAN might reflect a late-to-early feedback signal. Here, the effective connectivity analysis results reflect the interactions between the networks regardless of the time windows. In support of the claims made previously, the strong relationship between the SN-to-DAN EC and TEPR suggests an important role of the LC-NE system in this network reset (or circuit-breaker) top-down control signal. Based on the involvement of the SN nodes as the late-time salience processing network (Figure 3.20), and its higher hierarchy among the DAN and DMN (Y. Zhou et al., 2018), the CS-INR is thought to be involved in the late phases of the salience processing, reflecting a mark of behavior transition, task disengagement, and preparedness, initiated by the deactivation of SN. However, our

findings do not rule out the possibility that the CS-INR system might also be involved at the other phases of the trial. For example, a recent study has found that the DAN, SN, visual and frontoparietal regions are involved in the early phase of the re-orienting, which has been interpreted as a network reset signal (Spadone et al., 2021). Different from our findings, these results might reflect the reorienting modulation in task engagement or bottom-up stimuli processing. Consistent with our hypothesis, the LC activation has been shown to be more closely aligned with the behavioral response than the stimulus onset (Aston-Jones and Cohen, 2005; Poe et al., 2020), and our previous work has also demonstrated that the DMN is involved in the late phase of the trial in a target detection task (Walz et al., 2014). The DMN has been implicated in future planning (Buckner et al., 2008), task switching (Crittenden et al., 2015), attention shifts (Arsenault et al., 2018), as well as other functions (Buckner et al., 2008), and the LC-NE system has been proposed to modulate the DMN as a neural modulator of mind wandering (Mittner et al., 2016). Our results are consistent with hypothesis that the LC-NE system modulates the connectivity between the DAN and DMN (Jason S Tsukahara and Engle, 2021), and also the proposed role as a 'master switch' (Ross and Van Bockstaele, 2021). Potential candidate mechanisms of the LC-NE modulation on the DAN and DMN are: 1) The LC-NE system modulates them through the heterogeneous spatial distribution of NE receptor types and densities across the cortex (van den Brink et al., 2018; Van den Brink et al., 2016); 2) The heterogeneity in LC cell populations might be responsible for the targeted modulations of specific cortex areas (Schwarz and Luo, 2015; Totah et al., 2019), for example, a modular organization in the LC with distinct efferent neural projection patterns has been reported (Poe et al., 2020; Uematsu et al., 2017); 3) The LC-NE system might interact with other subcortical nuclei in the modulation (van den Brink et al., 2019), such as thalamus, which has been associated with the LC activity (MäkiMarttunen and Espeseth, 2021), SN activity (Seeley et al., 2007), and the modulation of cortical networks connectivity (Buckner and DiNicola, 2019; Nakajima and Halassa, 2017). The work may inform future studies of the neural mechanisms underlying the LC-NE modulation on the cortex.

The close relationship between the LC-NE system and the SN has been investigated thoroughly in the literature, for example Herman et al. found that the noradrenergic activation during acute stress results in the changes in the functional connectivity strength within the SN, and these changes were inferred as network reconfiguration in their study (Hermans et al., 2011). Their findings established a causal link from the LC-NE system activity to the activity of the SN, however the interaction between the SN and other brain networks, and how the two systems cooperate in an integrative framework are still unclear. Whereas, our study suggests that the LC-NE system might be responsible for the network-level interactions between the SN and other brain networks. The CS-INR network model proposed here bridges the gap between the network reset model of the LC-NE system and the network switching model of the SN, which could potentially serve as a cortico-subcortical network reorganization paradigm for understanding the neural dynamics underlying various cognitive functions, such as salience processing. With the neuronal basis of fast control in the von Economo neurons (VENs) of SN (Menon and Uddin, 2010) and the spatially diffuse projections from the LC (Aston-Jones and Cohen, 2005), the CS-INR system is ideally suited to a variety of complex cognitive processes. Although our results shed light on the relationship between the LC-NE system and the cortical network reorganization in the context of an auditory oddball task, we speculate that the CS-INR system might play a more general role in cognitive functions, such as adaptations in environmental volatility (Angela et al., 2005; Browning et al., 2015), brain state switches/variations (Mccormick et al., 2020;

McGinley et al., 2015), cognitive control (Cocuzza et al., 2020; Eldar et al., 2013; Gilzenrat et al., 2010; Köhler et al., 2016). Further work is needed to uncover the implications of the CS-INR model in various cognitive processes and neurological diseases. For example, previous studies have associated the activity in the DAN and DMN regions with exploitation and exploration, respectively (Chakroun et al., 2020). And it has been proposed that the SN and the LC-NE system may play a role in the switching from exploitation to exploration (Aston-Jones and Cohen, 2005; Chakroun et al., 2020), hence, it will be interesting to test the CS-INR model in the exploration and exploitation tasks.

Broader implications of a simultaneous pupillometry-EEG-fMRI study. In this study, we deployed a framework involving simultaneous recordings of pupillometry, EEG, and fMRI to investigate neural processes and interactions in salience processing. The high spatial resolution of fMRI data and functional connectivity analysis were utilized to map the neural substrates and the functional organizations. The EEG data with high temporal resolution, the single-trial analysis, and the effective connectivity state-space model were used to temporally 'tag' the neural substrates and infer the directional interactions. As a proxy of the LC activity, pupillometry was included to study the cortico-subcortical associations. The multimodal methodological approaches and the CS-INR network model proposed here might promote further investigations on the brain dynamics underlying various cognitive processes and neurological diseases. For example, the role of the LC in cognitive control is intriguing but has not been fully explored. This might be due to the gap in current knowledge between the network models of the cortex and the models of the LC, such as how the LC's function in network reset is related to the network switching function of the SN. Besides their critical contribution to attentional processing

as demonstrated in this study, the CS-INR network model proposed here, or other cortico-subcortical network models, is also critical in the understanding of neurological diseases, such as Alzheimer's disease (AD). As the first brain region in which AD-related pathology appears, the LC has been associated with cognitive decline and aging (Mather and Harley, 2016). The studies of the LC and pupil diameter fluctuations, and their interactions with the cortical networks have important implications for the understanding of neurological diseases, such as AD. For example, a recent study showed that the LC in the older population has reduced interaction with the SN, suggesting subsequent impairment in the initiation of network switching, and inferior ability in prioritizing the importance of incoming events (Lee et al., 2020).

In addition to the other work from our group where we used this multi-modal approach to examine the relationship between LC activity, pupillary response, and cortical dynamics (Hong et al., 2022), there are two other very recent instances where this simultaneous triple-modality data acquisition was reported (Groot et al., 2021; Mayeli et al., 2020). Together with the work presented here, all four studies showcase unique analyses and insights that could be harnessed from simultaneous pupillometry-EEG-fMRI. For instance, while this work and Hong et al. used an asymmetric fusion approach, Groot et al. applied a symmetric fusion to the multi-modal data through a support vector machine, in order to investigate neural signatures of task-unrelated thoughts. Taken together, we believe that despite the technical challenges, this simultaneous multi-modal approach holds great value and potential in unraveling cortical dynamics at various levels.

# 3.4 Dynamic Causal Modeling of the Locus Coeruleus and preSMA Circuit in Attentional Processing

#### 3.4.1 Introduction

The locus coeruleus is a small nucleus located in the brainstem, as a primary source of norepinephrine. Both the LC-NE and the salience network are important contributors to attentional processing. For example, the LC and the SN have been proposed in a network reorganization model for salience processing (He et al., 2023), a moderated mediation model for response inhibition (Tomassini et al., 2022), and a connectivity framework for cognitive aging (Lee et al., 2020). To further explore the integrated functions of the LC and the SN, here, we use dynamic causal modeling (DCM) (Friston et al., 2003) to investigate the connectivity between the LC and the pre-supplementary motor area (preSMA), which is a primary node of the SN. However, the challenges in the neuroimaging of the brainstem (e.g. physiological noise (Brooks et al., 2013)) still hinder the study of the associations between this brainstem nucleus and the cortical systems. The brainstem is located at the junction of the cerebrum and the spinal cord, surrounded by major arteries and cerebrospinal fluid-filled ventricles. Consequently, the fMRI signal at brainstem contains a prominent amount of physiological noise from the neighboring structures with a poor signal-to-noise ratio. In the fMRI data, cardiac related physiological noise sources include changes in cerebral blood flow, cerebral blood volume (CBV), CSF flow, and arterial pulsatility (Brooks et al., 2013). To addresses this issue, we use physiological noise modeling base on the simultaneously recorded ECG data. Here, we also aim to evaluate the impact of cardiac noise correction on the connectivity.

#### 3.4.2 Methods

Pupillometry-EEG-fMRI data were simultaneously recorded from nineteen healthy subjects (age: 26 ± 3.6) in a 3T scanner as described in Section 3.2.2. fMRI data were collected using T2\*w EPI (TR = 2100ms; TE = 25ms; voxel size 3 x 3 x 3mm; matrix size 64 x 64 x 42; 150 volumes) and were preprocessed with FSL (S. M. Smith et al., 2004). We used an auditory oddball paradigm, where both the LC-NE and the SN systems were expected to be elicited. To remove the cardiac noise, we used retrospective image correction (RETROICOR) (Glover et al., 2000), by first using the R-peak detection in the ECG signal and the extraction of the cardiac phase associated with the timing of each fMRI-acquired image. Specifically, in RETROICOR, the cardiac fluctuations are modeled as quasi-periodic processes with a low-order Fourier series and varying cardiac phases. The phase is computed as the time difference between the cardiac signal peak and the sampling time of the slice, relative to the physiological cycle (R-peak to R-peak interval). The cardiac noise component was regressed out with general linear modeling.

Volume of interest (VOI) localization was described in Section 3.3.2. Specifically, the LC was localized using a predefined atlas and subject-specific neuromelanin-sensitive MR images. An EEG-informed fMRI analysis was used to define the node of preSMA. For the DCM, a first-order model was fitted to the BOLD signal from VOIs. Standard and oddball trials were modeled as modulatory inputs. We then performed Bayesian model comparison, where the full model was compared to the reduced models with permutations of connections turned on and off. Lastly, to associate the connections with behavioral and pupil measurement, a second-order parametric empirical Bayes (PEB) was constructed according to the response indicators of the runs.

#### 3.4.3 Results

Figure 3.22 shows the winning model with the highest model evidence (Friston et al., 2007). The endogenous/modulatory connections between the VOIs before and after RETROICOR are illustrated in Figure 3.22A and Figure 3.22B, respectively. In the second-order PEB analysis, response time, pupillary response (PR), and pupil baseline diameter (PBD) variabilities were included as response parameters. In the standard stimuli case, the modulatory connections made a contribution to the PBD and PR, whereas, in the oddball stimuli case, the modulatory connections do not show an obvious effect (Figure 3.23C and 3.23D). Additionally, we also tested the association between the modulatory connections and the pupil measurements with Pearson correlation. We found that after RETROICOR, the standard stimuli modulated connections are significantly correlated with the pupil measurements of standard trials (LC-to-LC and mean PR-standard: r = -0.269, p = 0.010; preSMA-to-LC and mean PBD-standard: r = -0.270, p = 0.009). No significant association between modulatory connections and pupil measurements was found before RETROICOR (LC-to-LC and mean PR-standard: r = -0.066, p = 0.536; preSMA-to-LC and mean PBD-standard: r = -0.066, p = 0.536; preSMA-to-LC and mean PBD-standard: r = -0.009).

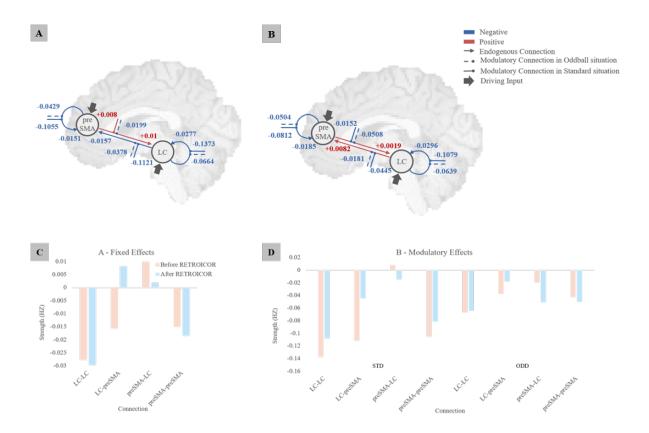


Figure 3.22: DCM and the endogenous/modulatory connections between the LC and preSMA. (A) and (B) represent the DCM connections before and after RETROICOR, respectively. The overlaid brain is only for illustration purposes. The numerical value with each connection represents the corresponding average effect at the group level. After RETROICOR, the results indicate a positive endogenous effect between the VOIs, whereas the self-connections are negative. (C) The comparison of endogenous connections before and after RETROICOR. (D) The comparison of context-dependent modulatory connections before and after RETROICOR. The 'STD' represents the standard stimuli situation, and the 'ODD' represents the oddball stimuli situation.

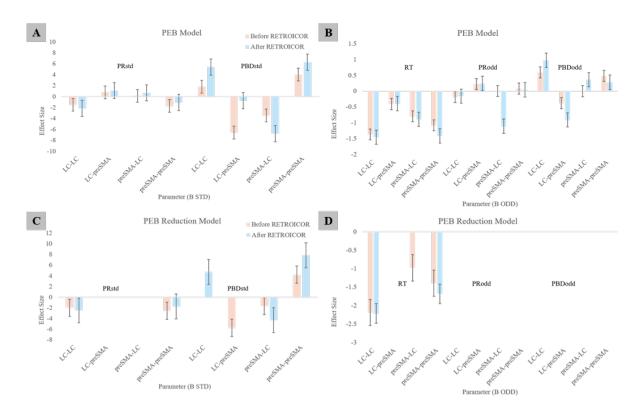


Figure 3.23: Parametric empirical Bayes (PEB) full and reduced model of the modulatory connection matrix based on the behavioral and pupil measurements. (A) The plot shows the PEB full model of the modulatory connection matrix in the standard stimuli situations. (B) The PEB full model of the modulatory connection matrix in oddball stimuli situations. (C) and (D) are the PEB reduced models in the standard and oddball stimuli situations, respectively. The thin line on each bar represents the standard error. RT, PRstd, PRodd, PBDstd, and PBDodd represent 'median response time', 'mean pupillary response of standard trials, 'mean pupillary response of oddball trials', 'mean pupil baseline diameter of standard trials', and 'mean pupil baseline diameter of oddball trials', respectively.

#### 3.4.4 Discussion

In this section, we examined interactions between the LC-NE and SN systems with DCM. We found that for standard trials, modulatory connections between the two systems contributed to the mean pupil measurements. Additionally, our results indicate that physiological noise removal impacts the relationship between pupillometry and LC-related connectivity, even

though such noise removal had been reported to have little impact on the relationship between pupillometry and BOLD signal in LC (Murphy et al., 2014).

# Chapter 4: Modulation of Functional Brain Networks using Transcranial Magnetic Stimulation and Its Brain-state Dependent Effects

#### 4.1 Introduction

TMS over the L-DLPFC is an FDA-approved treatment for depression. Concurrent TMSfMRI studies have established the propagation of TMS-induced activity from the left dorsolateral prefrontal cortex to various afferents (Dowdle et al., 2018). However, the TMS effects on networks distal to the stimulation site are less understood. And the state-dependent effects of TMS propagation pathways remain largely unexplored (Bergmann et al., 2021; Bradley et al., 2022). In the previous studies, it has been shown that TMS applied to the DLPFC attenuates hyperactivity in the default mode network (Liston et al., 2014), though its effects appear to be highly heterogenous, with reports of such stimulation both increasing and decreasing neuronal activity, depending on the region, network and stimulation parameters (Rafiei and Rahnev, 2022). Here, we aim to investigate the network-level effects of TMS, by assessing how application of TMS at L-DLPFC propagates through cortical networks and induces changes in whole-brain network connectivity. Specifically, we used concurrent TMS-EEG-fMRI to quantify TMS effects on the brain network systems, and we investigated the dependency of TMS-induced activity on the brain-state, indexed via EEG prefrontal alpha phase. Figure 4.1 illustrates the concurrent TMS-EEG-fMRI multimodal dataset.

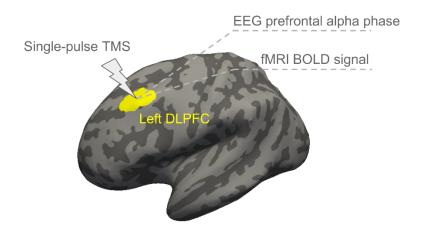


Figure 4.1: Illustration of the concurrent TMS-EEG-fMRI dataset used in the study. Specifically, simultaneous EEG-fMRI data were collected while single-pulse TMS was delivered to the left dorsolateral prefrontal cortex (DLPFC). To investigate brain-state dependency of TMS-induced fMRI signal changes, the phase of alpha oscillation in the EEG prefrontal recordings was used as an index of brain-state.

#### 4.2 Methods

An integrated fMRI-EEG-TMS instrument was developed and used in this study. EEG-fMRI data were acquired from twenty-eight depression patients inside a Siemens 3T Prisma scanner (EEG: 36 electrodes with 488 Hz sampling rate; fMRI: TR = 1750 ms with a 200 ms gap; TE1 = 11.20 ms; TE2 = 32.36 ms; TE3 = 53.52 ms; voxel size 3.2 x 3.2 x 3.2 mm; matrix size = 64 x 56 x 38; 233 volumes; 6 runs). Single-pulse TMS was delivered to the L-DLPFC (F3 electrode) at the beginning of the TR gap, with inter-trial-intervals drawn from a uniform distribution (4 - 6 TRs). fMRI data were preprocessed with AFNI (Cox and Hyde, 1997).

Whole-brain general linear modeling with FLOBS (Woolrich et al., 2004) was first performed to investigate TMS-induced BOLD response. The propagation of induced activity through cortical networks was quantified by computing the percent coverage of each network (brain parcellated with Schaefer atlas (Schaefer et al., 2018); Figure 4.3B). To investigate the TMS-modulated functional connectivity changes, we used psychophysiological interaction (PPI)

analysis (Friston et al., 1997). Specifically, local-global Schaefer cortical parcellation atlas (Schaefer et al., 2018) was used to define cortical region of interest and network systems, which is a fMRI based parcellation approach integrating local gradient and global similarity approaches based on resting state fMRI data from 1489 young adults. A whole-brain PPI analysis (Gerchen et al., 2014) was performed to assess any significant connections modulated by TMS. In the PPI analysis, the task modulated connectivity was examined. The interaction between the BOLD signal from one ROI and the task regressor was modeled by first deconvolving the BOLD signal from the canonical HRF and then being multiplied by the task timing boxcar function. As the PPI analysis focus on the second-order task modulation, controlling the first-order task modulation (task-evoked mean activation) is necessary, as the task-evoked mean activation could be a potential confounder and drives the false positive observed interaction between regions (Cole et al., 2019). Specifically, FLOBS based task regression was performed to account for the task-evoked mean activation, which has been shown to achieve a relatively low false positive results in controlling the confounds (Cole et al., 2019).

The FC matrix was symmetrized, and the beta-weights were summarized within/between networks. Finally, we assessed positive/negative node strength by computing the sum of all positive/negative connection weights associated with each node. Additionally, to investigate the dependency of induced FC changes on the brain-state (indexed via EEG prefrontal alpha phase), we performed the same PPI analysis where TMS trials were grouped into four bins based on the TMS timing relative to the phase of the EEG alpha rhythm.

Figure 4.2 illustrates the brain-state dependency analysis, where prefrontal alpha (7.5-12 Hz) was extracted from the EEG signals at channels FP1, F3 and F7, and the phase (index of brain-state) at TMS onset was estimated. TMS trials were grouped into four phase bins based on

the alpha phase. Then, general linear modeling was used to model the BOLD signal at left-DLPFC (stimulation site), with the trials in each phase bin as a separate regressor. For each subject, the phase bins that generated the highest and lowest BOLD response at left-DLPFC were identified as the subject-wise preferred-phase and nonpreferred-phase, respectively. Lastly, whole-brain GLM analysis was performed to identify correlates of the preferred-vs-nonpreferred phase contrast.

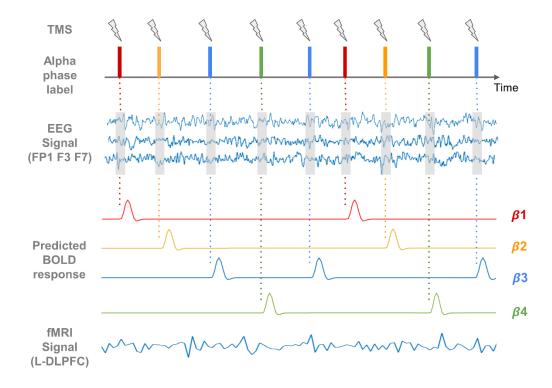


Figure 4.2: Illustration of brain-state dependency analysis. Single-pulse TMS trials were grouped into four bins based on their timing relative to frontal alpha phase. The TMS trials in the figure were labeled according to their phase bin group using four different colors: red, yellow, blue, green. The onset times of TMS trials in each phase bin were convolved with the canonical HRF, resulting in four predictors of the fMRI BOLD time series. Response amplitudes (beta weights) were used to describe TMS-induced effects on each condition (frontal alpha phase).

#### 4.3 Results

The group-level TMS-induced BOLD activation map is shown in Figure 4.3A (permutation test with FSL Randomise (Winkler et al., 2014); p < 0.05 FWE-corrected), and the induced-activity propagation coverage of networks is shown in Figure 4.3C. TMS significantly elevated BOLD signals in various brain regions including dorsal anterior cingulate, thalamus, right-DLPFC, but not left-DLPFC. In PPI analysis, we observed significant TMS-induced connectivity changes between networks (Figure 4.4A; p < 0.05 FDR-corrected; all negative effects). As shown in Figure 4.4B&C, the negative hubs (with a stronger negative node strength) are within the control-default regions, whereas the positive hubs are within the control-processing regions.

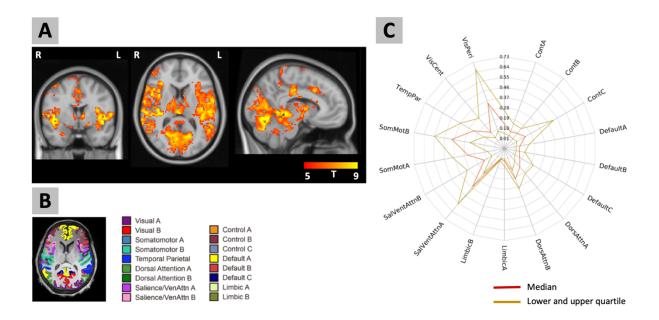


Figure 4.3: Quantification of TMS-induced BOLD response. (A) group-level activation map (t-value; p < 0.05 FWE multiple comparison correction; mixed effect); (B) Schaefer atlas brain parcellation (400 regions of interest) was applied to each subject by the registration of cortical surface; (C) Coverage across networks of TMS induced-activity (TMS applied to L-DLPFC). Shown is the percent (fractional, 0.0 - 1.0) coverage. The red line indicates the median across subjects. Brown lines indicate the lower and upper quartile across subjects. We found that SomMotB, SalVentAttnA, and VisPeri have the highest coverage of TMS-induced activity, and VisPeri, ContC, and SalVentAttnA have the highest inter-subject variability.

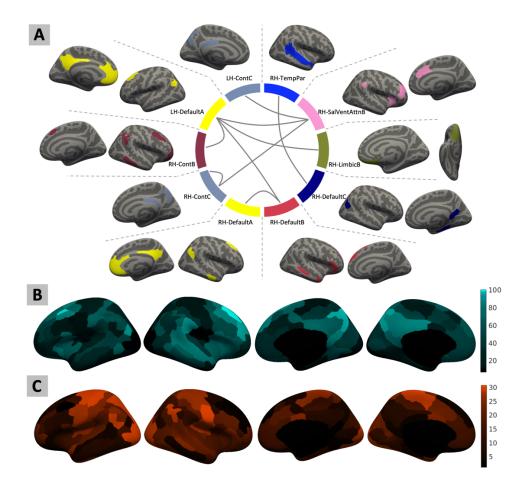


Figure 4.4: Quantification of TMS-induced functional connectivity changes. (A) Group level whole-brain psychophysiological interaction analysis results. TMS applied to L-DLPFC induced significant negative effects on the connectivity between cortical networks (p < 0.05 FDR multiple comparison correction). No significant positive effects were observed after multiple comparison correction. (B) and (C) represent negative and positive node strength by computing the sum of all the negative and positive connection weights between one node and all other nodes, respectively. The negative hubs are within the regions/nodes of the control and default network regions, whereas the positive hubs are within the control-processing regions.

In the results of brain-state dependency analysis, the preferred-vs-nonpreferred phase contrast analysis identified regions in the lateral frontoparietal network (Uddin et al., 2019) as significant clusters (p < 0.001,uncorrected) including bilateral DLPFC and inferior parietal lobule (Figure 4.5A). Lastly, at the subject-level, to investigate phase contrast effects at left-

DLPFC, we permuted trials' phase bin labels, and the permutation test showed that eleven subjects have significant phase contrast effects at left-DLPFC (p < 0.05). We also quantified the spatial overlap between TMS response contrast map and functional connectivity map, as shown in Figure 4.5B. Functional connectivity map using the left DLPFC as the seed region showed a network overlapped with the TMS response contrast map. In the results of brain-state dependency PPI analysis, TMS trials in the preferred phase bins induced significant (p < 0.05 FDR-corrected) negative FC changes between: 1) RH-Default-A and RH-Default-B; 2) RH-Default-A and RH-ContA; 3) RH-Default-A and RH-ContB, whereas no significant FC changes were observed for the TMS trials in the nonpreferred phase bins.

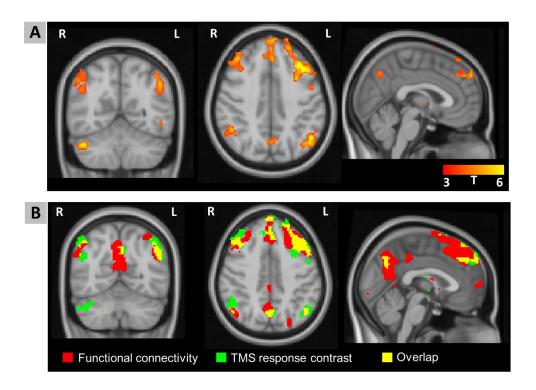


Figure 4.5: Brain state-dependency analysis results. (A) Preferred v.s. non-preferred phase contrast. Regions in the lateral frontoparietal network (L-FPN) were identified as significant clusters (t-value; p < 0.001; uncorrected). (B) Spatial overlap between TMS response contrast and functional connectivity. Functional connectivity map using the left DLPFC as the seed region showed a network overlapped with the TMS response contrast map.

#### 4.4 Discussion

In the results of PPI analysis, we found that TMS induced strong negative effects within and between DMN and control networks, which might help regulate the hyperactivity in the DMN of depression patients (Liston et al., 2014). The observations from our hub analysis align with the hypothesis in (Rafiei and Rahnev, 2022), where the positive and negative effects of TMS follow distinct pathways of control-processing and control-default regions, respectively. These pathways might reflect separate, yet parallel top-down signals organized by the categorized connector hubs in the brain (Gordon et al., 2018). In the results of brain-state

dependency analysis, the results suggest that the propagation of TMS-induced BOLD activity from the left-DLPFC to regions in the L-FPN might depend on the EEG prefrontal alpha phase. In general, this type of brain-state dependent analysis can be used to temporally optimize and personalize TMS targeting for treatment of depression (Faller et al., 2022; Pantazatos et al., 2022).

# **Chapter 5: Conclusions and Future Directions**

## 5.1 Summary

In this thesis, we employed novel computational and multimodal data analysis techniques to examine the structural and functional attributes of brain network systems. Our investigation encompassed a broad range of characteristics, including anatomy variability, task-related responses, connectivity, and the effects of neuromodulation. We have developed a novel regionbased spatial normalization approach that enables accurate quantification of brain structural variability. Our evaluation results demonstrated that this approach could improve the sensitivity and specificity in the group-level analysis of task-based fMRI studies. In addition to examining the structural organization of brain network systems, we conducted further investigation into their functional aspects. Our findings showed that pupillary response is associated with the reset and switching of brain networks during salience processing. These results contribute to the understanding of the interconnections between cortical networks and brainstem neuromodulatory system. Finally, our study extended beyond the examination of the structural and functional characteristics of brain network systems. We conducted a preliminary multimodal investigation using a neuromodulation approach, which has the potential to provide more causal evidence in the mapping of brain network systems.

In the first part of Chapter 2, we developed a landmark-guided region-based spatial normalization approach for analyzing structural and function MRI. Specifically, using automatic landmark detection and matching, we have developed and implemented a novel 3D volumetric spatial normalization solution that not only aligns the cortical folding patterns of the brain, but also results in a high correspondence between different regions along the cortical ribbon and their counterparts in the template image. Our solution substantially outperforms the existing top

performing volumetric spatial normalization method by giving a significantly higher correspondence between the structure of the neuroanatomical regions, and also yields higher sensitivity and specificity in the group-level statistics when analyzing task-based fMRI data with both auditory and visual stimuli. The limited accuracy of conventional methods becomes more prominent when applied to clinical and aging populations with severe alterations in brain morphology. When compared to the healthy group, this population-based bias has been shown to generate false-positive findings that have been reported as a genuine breakthrough in the literature (Liu et al., 2017). We conclude that our proposed LG-RBSN solution is a suitable substitute for the conventional volumetric whole brain registration methods that often fail to generate an accurate correspondence between regions of the cerebral cortex, particularly for clinical and aging populations.

In the second part of Chapter 2, we investigated the fMRI responses to visual stimuli, where we explored both the positive and negative hemodynamic responses in the visual network system. Our findings provide evidence that the two task-evoked NBRs due to unilateral visual stimulation are linearly related to the stimulus duration. Their extracted HRFs have similar magnitude and dynamics, while showing differences compared to the HRF extracted from PBR. The subject-wise expression of the cNBR is tightly coupled with that of the iNBR in the opposite hemisphere and significantly less correlated with PBR detected in its vicinity. Inversely, the spatial pattern of the iNBR is more inter-hemispherically similar to that of the PBR than to the corresponding cNBR. Neither of the PBR nor the two NBRs predict the task performance. Moreover, while attention did not alter the timings and peak magnitude of the PBR, both magnitude and return to baseline of the iNBR and cNBR (although not significant for cNBR) were modulated by attention. Our findings suggest that common neural and/or vascular

mechanisms underlie the cNBR and iNBR. These mechanisms are possibly different from the mechanisms that give rise to the PBR, and they might involve subcortical brain structures with projections to both hemispheres.

Drawing on the findings in Chapter 2, we hypothesized that deep brain structures, for example brainstem neuromodulatory systems, might regulate the task-evoked negative responses in the visual network. To further investigate such associations between cortical networks and brainstem neuromodulatory systems, we conducted multimodal investigations with a pupillometry-EEG-fMRI dataset in Chapter 3. In summary, firstly, the study in Chapter 3 reveals a coordinated neural cascade during salience processing, involving brain regions in the dorsal attention, visual, motor, executive control, and salience networks. Secondly, the study identified the network organization and effective connectivity between these brain regions, which were found to be associated with salient stimuli evoked pupillary response. These findings are in line with the proposed function of the pupil-indexed LC-NE system in network reset (Bouret and Sara, 2005; Corbetta et al., 2008). To advance understanding of the interactions between neuromodulatory systems and intrinsic brain networks in relation to cognition, the study presented additional analyses on the associations between the LC-NE system and networks including the SN, DAN, and DMN, where the results provide the first evidence in humans for the relevance of the LC-NE system to the function of the SN in the dynamic switching between anticorrelated cortical networks. The findings in Chapter 3 have important implications for multimodal neuroimaging data analyses, brain-pupil relationships, attentional processing, cognitive control networks, and network models of neurological diseases.

In Chapter 3, we conducted an investigation of brain network system reorganization in

the context of salience processing. Alongside this task-evoked network reorganization, endogenous network reorganization and the brain-state dependency were also crucial elements of brain network dynamics. Thus, in Chapter 4, we delved deeper into this subject by characterizing the causal effects of TMS on brain network systems. Our analysis included quantifying TMS-induced BOLD response and TMS-modulated functional connectivity changes, and we demonstrated the brain-state dependency of TMS effects. The quantification and understanding of TMS effects on brain network systems carry significant implications for the treatment of major depressive disorder and the development of personalized TMS treatment protocols, with a focus on both target-selection and timing parameters.

#### **5.2** Limitations and Future Work

In Chapter 2, we developed a novel spatial normalization approach to accurately quantify inter-subject variabilities in brain anatomy. However, it is already known that the functional architecture of the brain does not necessarily and accurately follow brain gyri and sulci morphology. Therefore, one might conclude that improving the correspondence between brain structural features (sulci and gyri) might not necessarily translate to improvement in functional correspondence of the aligned regions, and would alter the effects of the improved spatial normalization methods in functional imaging of the brain. Since we currently do not have an accurate measurement of the deviation of the functional architecture from brain morphology, it is difficult to assess any limit in which improvement of the regional correspondence becomes unattainable. And as compared to CVS, the worse performance of LG-RBSN in the functional evaluation with right ear auditory stimuli condition might be due to this reason. Nonetheless, we have shown that increasing the regional correspondence to 86% still increases the functional

correspondence for the visual stimuli and the left ear auditory stimuli conditions, and indicates that we are still operating under such limitation in these conditions. To further align the functional architecture of the brain, in future work, the proposed LG-RBSN can also be modified to identify landmarks from functional or other imaging modality data, so that landmarks correspondence is established using functional cortical registration methods to help align the brain functional organizations across subjects.

Alongside the quantification and investigation of brain structural organization, in Chapter 3, we investigated the functional organization of brain networks and their functional/effective connectivity. Specifically, we used effective connectivity to infer the directional couplings between brain networks. However, in the effective connectivity state-space model, the temporal dependence among the dynamics of latent neural states of different brain areas was modeled as a multivariate autoregressive process. For example, the effective connectivity estimates how the future neural states in one brain area are influenced by the current neural states in another brain area, and how the external experimental perturbation can modulate these couplings. Thus, the directionality of information flow was inferred based on temporal forecasting and control theory, and the 'directional interaction' in Chapter 3 is limited under the assumptions of our effective connectivity state space model. Future studies using simultaneous pupillometry, neuroimaging, and transcranial magnetic stimulation would be interesting to explore the relationship between pupil diameter fluctuations and brain networks couplings, and potentially to provide stronger evidence on the 'directionality' of brain networks interaction. Furthermore, the directionality in the cortico-subcortical interactions between the LC and cortex regions remain unclear. Based on the involvement of the SN in the late time of the trial observed in our data, we hypothesized that the network switching might be modulated by the release of the NE, as an effect of the ascending neuromodulation. Our hypothesis aligns with the findings in (Hermans et al., 2011), which provided evidence on the causal link from the LC-NE system activity to the activity of the SN. Whereas, in the adaptive gain theory, the LC is proposed to receive inputs from ACC and OFC, with the release of NE at cortical target sites (Aston-Jones and Cohen, 2005). Further investigations will be needed to better understand the directionality in the interactions between the LC and cortex regions.

Pupillometry has long been used to index the LC activity in previous studies (Aston-Jones and Cohen, 2005; Gilzenrat et al., 2010; Joshi and Gold, 2020; Murphy et al., 2011) and also in the study of Chapter 3, though it is challenging, as other neural circuits are involved in controlling pupil diameter as well (Joshi and Gold, 2020). For example, shifts of attention are mediated in part by the superior colliculus (SC). In the previous studies, the LC rather than the SC showed neural spiking responses to unexpected auditory events (Joshi et al., 2016). In an oddball task fMRI study, the pupil size fluctuations have been associated with the BOLD activity in the LC (Murphy et al., 2014). In Chapter 3, we utilized this well-studied oddball paradigm, where the coupling between pupillometry and the LC activity has been shown, to investigate the pupil-indexed activity in the LC. However, this does not rule out the possibility that other subcortical nuclei, such as thalamus, or other neuromodulators, such as acetylcholine, might contribute to pupil diameter fluctuations or interact with the LC-NE system. Further investigations are needed for direct neuroimaging of the LC, however, it is challenging due to the excessive physiological noise and distortion in brainstem imaging (Beissner, 2015), and the difficulty in the localization of the LC (Mäki-Marttunen and Espeseth, 2021). Additionally, the present study did not examine the relationship between the LC activity and pupillary response, as well as its relationship to the EEG measurement of cortex processes. Another study from our

group highlighted these additional analyses and comprehensive examinations of LC activity and their associations (Hong et al., 2022). In Chapter 3, we examined the relationship between effective connectivity and pupil measurement at the inter-individual level as shown in Figure 3.16. Future studies are needed to replicate our results at the intra-individual level. However, care should be taken when fitting the effective connectivity model without enough data points. And more experimental sessions and data acquisition for each individual may be needed.

In Chapter 3, we made inferences on the role of the pupil-indexed LC activity in salience processing, based on their interaction with the task-related neural substrates. However, besides the attentional processing of salient stimuli, pupil-indexed LC activity has also been associated to changes in arousal. Though these two LC associated processes, i.e. attention and arousal, have been shown to be independent (Vazey et al., 2018), an important future direction will be accounting for the LC associated arousal, and assessing its relationship to the cortex. In future studies, novel tasks can be devised to dissociate pupil-indexed LC activity in attention and arousal.

The interactions between the brainstem and cortex systems are less understood. For example, functional connectivity analysis has consistently identified regions in the midbrain of brainstem and other subcortical areas as part of the SN (Seeley et al., 2007). However, how they interact with the main nodes of the SN (dorsal ACC and anterior insula), and what is their integrative role in the context of SN function have not been explored (Menon, 2015). In future studies, it will be interesting to investigate the structural, functional and effective connectivity between the SN and the LC-NE system, to enhance our understanding of these crucial brain systems and their interactions. For example, we propose to use concurrent TMS-fMRI techniques to quantify the TMS-induced activity in the LC-NE system when TMS pulses are delivered to

the SN nodes. This approach will provide insights into the causal relationship between these two systems. By utilizing causal brain mapping techniques such as this, we will gain valuable insights into the understanding of TMS mechanisms and the development of novel therapeutic interventions.

In Chapter 3, we proposed a localization approach for the LC and examined the effective connectivity between the LC and the preSMA region. However, in future studies, care must be taken in the processing of neuroimaging data in the brainstem area, as the standard pipeline available in the neuroimaging field may be unsuitable. For example, in terms of spatial normalization approaches, the standard spatial normalization methods are solving a global optimization problem in the registration of the whole-brain, this standard approach might achieve sub-optimal results in the brainstem areas. Spatial normalization methods targeting the brainstem areas have been developed, such as the spatially unbiased atlas template (SUIT) method (Diedrichsen, 2006) and the automated brainstem co-registration (ABC) method (Napadow et al., 2006). However, all these existing methods relied on the matching of T1-weighted image intensities. This is feasible in the registration of cortical regions and systems to some extent, as the shapes and boundaries of cortical regions and systems can be characterized by the folding of the cerebral cortex and the contrast between grey matter and white matter in the T1-weighted image intensity contrast. However, the T1-weighted image intensities are homogeneous in the brainstem areas, which makes the characterization and registration of brainstem structures and regions almost impossible. Standard neuroimaging preprocessing pipeline typically includes spatial smoothing, which can compensate for the registration errors. However, in practice, spatial smoothing has been shown to obscure the estimate of brainstem nuclei BOLD activity (Murphy et al., 2014). As most of the brainstem nuclei are very small, it is not ideal to perform spatial

smoothing when coping with the neuroimaging data of the brainstem. Methods that accurately characterize and register brainstem structures are warranted.

## References

- Abreu, R., Leal, A., Figueiredo, P., 2018. EEG-informed fMRI: A review of data analysis methods. Front. Hum. Neurosci. https://doi.org/10.3389/fnhum.2018.00029
- Allen, P.J., Josephs, O., Turner, R., 2000. A method for removing imaging artifact from continuous EEG recorded during functional MRI. Neuroimage 12, 230–239.
- Anderson, R.J., Hoy, K.E., Daskalakis, Z.J., Fitzgerald, P.B., 2016. Repetitive transcranial magnetic stimulation for treatment resistant depression: Re-establishing connections. Clin. Neurophysiol. 127, 3394–3405. https://doi.org/10.1016/J.CLINPH.2016.08.015
- Andersson, J.L.R., Jenkinson, M., Smith, S., others, 2007. Non-linear registration, aka Spatial normalisation FMRIB technical report TR07JA2. FMRIB Anal. Gr. Univ. Oxford 2, e21.
- Andersson, J.L.R., Skare, S., Ashburner, J., 2003. How to correct susceptibility distortions in spin-echo echo-planar images: Application to diffusion tensor imaging. Neuroimage 20, 870–888. https://doi.org/10.1016/S1053-8119(03)00336-7
- Angela, J.Y., Dayan, P., Yu, A.J., Dayan, P., Angela, J.Y., Dayan, P., 2005. Uncertainty, neuromodulation, and attention. Neuron 46, 681–692.
- Arsenault, J.T., Caspari, N., Vandenberghe, R., Vanduffel, W., 2018. Attention shifts recruit the monkey default mode network. J. Neurosci. 38, 1202–1217.
- Arsigny, V., Pennec, X., Ayache, N., 2005. Polyrigid and polyaffine transformations: A novel geometrical tool to deal with non-rigid deformations Application to the registration of histological slices. Med. Image Anal. 9, 507–523. https://doi.org/10.1016/j.media.2005.04.001
- Ashburner, J., Andersson, J.L.R., Friston, K.J., 1999. High-dimensional image registration using symmetric priors. Neuroimage 9, 619–628. https://doi.org/10.1006/nimg.1999.0437
- Astafiev, S. V, Snyder, A.Z., Shulman, G.L., Corbetta, M., 2010. Comment on "Modafinil Shifts Human Locus Coeruleus to Low-Tonic, High-Phasic Activity During Functional MRI" and "Homeostatic Sleep Pressure and Responses to Sustained Attention in the Suprachiasmatic Area." https://doi.org/10.1126/science.1177200
- Aston-Jones, G., Cohen, J.D., 2005. An integrative theory of locus coeruleus-norepinephrine function: adaptive gain and optimal performance. Annu. Rev. Neurosci. 28, 403–450. https://doi.org/10.1146/annurev.neuro.28.061604.135709
- Auzias, G., Colliot, O., Glaunès, J.A., Perrot, M., Mangin, J.F., Trouve, A., Baillet, S., 2011. Diffeomorphic brain registration under exhaustive sulcal constraints. IEEE Trans. Med. Imaging 30, 1214–1227. https://doi.org/10.1109/TMI.2011.2108665
- Avants, B.B., Epstein, C.L., Grossman, M., Gee, J.C., 2008. Symmetric diffeomorphic image registration with cross-correlation: Evaluating automated labeling of elderly and neurodegenerative brain. Med. Image Anal. 12, 26–41. https://doi.org/10.1016/j.media.2007.06.004
- Avants, B.B., Tustison, N.J., Stauffer, M., Song, G., Wu, B., Gee, J.C., 2014. The Insight ToolKit image registration framework. Front. Neuroinform. 8, 44. https://doi.org/10.3389/fninf.2014.00044

- Balakrishnan, G., Zhao, A., Sabuncu, M.R., Guttag, J., Dalca, A. V., 2019. VoxelMorph: A Learning Framework for Deformable Medical Image Registration. IEEE Trans. Med. Imaging 38, 1788–1800. https://doi.org/10.1109/TMI.2019.2897538
- Beatty, J., 1982. Task-evoked pupillary responses, processing load, and the structure of processing resources. Psychol. Bull. 91, 276–292. https://doi.org/10.1037/0033-2909.91.2.276
- Beg, M.F., Miller, M.I., Trouvé, A., Younes, L., 2005. Computing large deformation metric mappings via geodesic flows of diffeomorphisms. Int. J. Comput. Vis. 61, 139–157. https://doi.org/10.1023/B:VISI.0000043755.93987.aa
- Beissner, F., 2015. Functional MRI of the Brainstem: Common Problems and their Solutions. Clin. Neuroradiol. https://doi.org/10.1007/s00062-015-0404-0
- Benarroch, E.E., 2009. The locus ceruleus norepinephrine system: functional organization and potential clinical significance. Neurology 73, 1699–1704.
- Benson, N.C., Butt, O.H., Brainard, D.H., Aguirre, G.K., 2014. Correction of Distortion in Flattened Representations of the Cortical Surface Allows Prediction of V1-V3 Functional Organization from Anatomy 10, e1003538. https://doi.org/10.1371/JOURNAL.PCBI.1003538
- Bergmann, T.O., Varatheeswaran, R., Hanlon, C.A., Madsen, K.H., Thielscher, A., Siebner, H.R., 2021. Concurrent TMS-fMRI for causal network perturbation and proof of target engagement. Neuroimage 237, 118093. https://doi.org/10.1016/J.NEUROIMAGE.2021.118093
- Boas, D.A., Jones, S.R., Devor, A., Huppert, T.J., Dale, A.M., 2008. A vascular anatomical network model of the spatio-temporal response to brain activation. Neuroimage 40, 1116–1129.
- Bocci, T., Pietrasanta, M., Cerri, C., Restani, L., Caleo, M., Sartucci, F., 2014. Visual callosal connections: role in visual processing in health and disease. Rev. Neurosci. 25, 113–127.
- Bookstein, F.L.F.L., 1989. Principal warps: thin-plate splines and the decomposition of deformations. IEEE Trans. Pattern Anal. Mach. Intell. 11, 567–585. https://doi.org/10.1109/34.24792
- Botvinick, M.M., Carter, C.S., Braver, T.S., Barch, D.M., Cohen, J.D., 2001. Conflict monitoring and cognitive control. Psychol. Rev. 108, 624–652. https://doi.org/10.1037/0033-295X.108.3.624
- Bouret, S., Sara, S.J., 2005. Network reset: a simplified overarching theory of locus coeruleus noradrenaline function. Trends Neurosci. 28, 574–582. https://doi.org/10.1016/J.TINS.2005.09.002
- Boynton, G.M., Engel, S.A., Glover, G.H., Heeger, D.J., 1996. Linear systems analysis of functional magnetic resonance imaging in human V1. J. Neurosci. 16, 4207–4221. https://doi.org/10.1523/JNEUROSCI.16-13-04207.1996
- Braak, H., Del Tredici, K., 2014. Neuroanatomy and pathology of sporadic Alzheimer's disease.
- Bradley, C., Nydam, A.S., Dux, P.E., Mattingley, J.B., 2022. State-dependent effects of neural stimulation on brain function and cognition. Nat. Rev. Neurosci. 2022 238 23, 459–475. https://doi.org/10.1038/s41583-022-00598-1
- Brain-Products., 2019. BrainAmp & BrainAmp MR Series Operating Instructions. Brain Prod. GmbH.
- Bressler, D., Spotswood, N., Whitney, D., 2007. Negative BOLD fMRI Response in the Visual

- Cortex Carries Precise Stimulus-Specific Information. PLoS One 2, e410. https://doi.org/10.1371/JOURNAL.PONE.0000410
- Bressler, D.W., Fortenbaugh, F.C., Robertson, L.C., Silver, M.A., 2013. Visual spatial attention enhances the amplitude of positive and negative fMRI responses to visual stimulation in an eccentricity-dependent manner. Vision Res. 85, 104–112. https://doi.org/10.1016/j.visres.2013.03.009
- Brink, R.L. van den, Pfeffer, T., Warren, C.M., Murphy, P.R., Tona, K.-D., Wee, N.J.A. van der, Giltay, E., Noorden, M.S. van, Rombouts, S.A.R.B., Donner, T.H., Nieuwenhuis, S., 2016. Catecholaminergic Neuromodulation Shapes Intrinsic MRI Functional Connectivity in the Human Brain. J. Neurosci. 36, 7865. https://doi.org/10.1523/JNEUROSCI.0744-16.2016
- Brooks, J.C.W., Faull, O.K., Pattinson, K.T.S., Jenkinson, M., Beissner, F., 2013. Physiological Noise in Brainstem fMRI. Front. Hum. Neurosci. 7, 623. https://doi.org/10.3389/fnhum.2013.00623
- Browning, M., Behrens, T.E., Jocham, G., O'reilly, J.X., Bishop, S.J., 2015. Anxious individuals have difficulty learning the causal statistics of aversive environments. Nat. Neurosci. 18, 590–596.
- Buckner, R.L., Andrews-Hanna, J.R., Schacter, D.L., 2008. The brain's default network: anatomy, function, and relevance to disease. Ann. N. Y. Acad. Sci. 1124, 1–38.
- Buckner, R.L., DiNicola, L.M., 2019. The brain's default network: updated anatomy, physiology and evolving insights. Nat. Rev. Neurosci. 20, 593–608.
- Buracas, G.T., Boynton, G.M., 2007. The effect of spatial attention on contrast response functions in human visual cortex. J. Neurosci. 27, 93–97.
- Caballero-Gaudes, C., Reynolds, R.C., 2017. Methods for cleaning the BOLD fMRI signal. Neuroimage 154, 128–149. https://doi.org/10.1016/J.NEUROIMAGE.2016.12.018
- Chakroun, K., Mathar, D., Wiehler, A., Ganzer, F., Peters, J., 2020. Dopaminergic modulation of the exploration/exploitation trade-off in human decision-making. Elife 9, e51260. https://doi.org/10.7554/ELIFE.51260
- Chen, A.C., Oathes, D.J., Chang, C., Bradley, T., Zhou, Z.-W.W., Williams, L.M., Glover, G.H., Deisseroth, K., Etkin, A., Williamsa, L.M., Glover, G.H., Deisseroth, K., Etkin, A., 2013. Causal interactions between fronto-parietal central executive and default-mode networks in humans. Proc. Natl. Acad. Sci. 110, 19944–19949. https://doi.org/10.1073/PNAS.1311772110
- Chen, C.C., Tyler, C.W., Liu, C.L., Wang, Y.H., 2005. Lateral modulation of BOLD activation in unstimulated regions of the human visual cortex. Neuroimage 24, 802–809. https://doi.org/10.1016/j.neuroimage.2004.09.021
- Christensen, G.E., Johnson, H.J., 2001. Consistent image registration. IEEE Trans. Med. Imaging 20, 568–582. https://doi.org/10.1109/42.932742
- Cipolla, M.J., 2009. The cerebral circulation. Integr. Syst. Physiol. From Mol. to Funct. 1, 1–59.
- Cocchi, L., Sale, M. V., Lord, A., Zalesky, A., Breakspear, M., Mattingley, J.B., 2015. Dissociable effects of local inhibitory and excitatory theta-burst stimulation on large-scale brain dynamics. J. Neurophysiol. 113, 3375–3385. https://doi.org/10.1152/JN.00850.2014
- Cocuzza, C. V., Ito, T., Schultz, D., Bassett, D.S., Cole, M.W., 2020. Flexible coordinator and switcher hubs for adaptive task control. J. Neurosci. 40, 6949–6968.

- https://doi.org/10.1523/JNEUROSCI.2559-19.2020
- Cole, M.W., Ito, T., Bassett, D.S., Schultz, D.H., 2016. Activity flow over resting-state networks shapes cognitive task activations. Nat. Neurosci. 19, 1718–1726. https://doi.org/10.1038/nn.4406
- Cole, M.W., Ito, T., Schultz, D., Mill, R., Chen, R., Cocuzza, C., 2019. Task activations produce spurious but systematic inflation of task functional connectivity estimates. Neuroimage 189, 1–18. https://doi.org/10.1016/j.neuroimage.2018.12.054
- Cole, M.W., Reynolds, J.R., Power, J.D., Repovs, G., Anticevic, A., Braver, T.S., 2013. Multi-task connectivity reveals flexible hubs for adaptive task control. Nat. Neurosci. 16, 1348–1355. https://doi.org/10.1038/nn.3470
- Corbetta, M., Patel, G., Shulman, G.L., 2008. The reorienting system of the human brain: from environment to theory of mind. Neuron 58, 306–324. https://doi.org/10.1016/j.neuron.2008.04.017
- Cox, R.W., Hyde, J.S., 1997. Software Tools for Analysis and Visualization of fMRI Data. https://doi.org/10.1002/(SICI)1099-1492(199706/08)10:4/5
- Critchley, H.D., Tang, J., Glaser, D., Butterworth, B., Dolan, R.J., 2005. Anterior cingulate activity during error and autonomic response. Neuroimage 27, 885–895.
- Crittenden, B.M., Mitchell, D.J., Duncan, J., 2015. Recruitment of the default mode network during a demanding act of executive control. Elife 4, e06481.
- Dale, A.M., Buckner, R.L., 1997. Selective averaging of rapidly presented individual trials using fMRI. Hum. Brain Mapp. 5, 329–340.
- de Gee, J.W., Colizoli, O., Kloosterman, N.A., Knapen, T., Nieuwenhuis, S., Donner, T.H., 2017. Dynamic modulation of decision biases by brainstem arousal systems. Elife 6, e23232. https://doi.org/10.7554/eLife.23232
- Desai, R., Liebenthal, E., Possing, E.T., Waldron, E., Binder, J.R., 2005. Volumetric vs. surface-based alignment for localization of auditory cortex activation. Neuroimage 26, 1019–1029. https://doi.org/10.1016/j.neuroimage.2005.03.024
- Desikan, R.S., Ségonne, F., Fischl, B., Quinn, B.T., Dickerson, B.C., Blacker, D., Buckner, R.L., Dale, A.M., Maguire, R.P., Hyman, B.T., Albert, M.S., Killiany, R.J., 2006. An automated labeling system for subdividing the human cerebral cortex on MRI scans into gyral based regions of interest. Neuroimage 31, 968–980. https://doi.org/10.1016/j.neuroimage.2006.01.021
- Diedrichsen, J., 2006. A spatially unbiased atlas template of the human cerebellum. Neuroimage 33, 127–138. https://doi.org/10.1016/j.neuroimage.2006.05.056
- DiNuzzo, M., Mascali, D., Moraschi, M., Bussu, G., Maugeri, L., Mangini, F., Fratini, M., Giove, F., 2019. Brain Networks Underlying Eye's Pupil Dynamics. Front. Neurosci. 13, 965. https://doi.org/10.3389/fnins.2019.00965
- Dosenbach, N.U.F., Fair, D.A., Miezin, F.M., Cohen, A.L., Wenger, K.K., Dosenbach, R.A.T., Fox, M.D., Snyder, A.Z., Vincent, J.L., Raichle, M.E., Schlaggar, B.L., Petersen, S.E., others, 2007. Distinct brain networks for adaptive and stable task control in humans. Proc. Natl. Acad. Sci. 104, 11073–11078. https://doi.org/10.1073/PNAS.0704320104
- Dowdle, L.T., Brown, T.R., George, M.S., Hanlon, C.A., 2018. Single pulse TMS to the DLPFC, compared to a matched sham control, induces a direct, causal increase in caudate,

- cingulate, and thalamic BOLD signal. Brain Stimul. 11, 789–796. https://doi.org/10.1016/J.BRS.2018.02.014
- Downar, J., Crawley, A.P., Mikulis, D.J., Davis, K.D., 2002. A cortical network sensitive to stimulus salience in a neutral behavioral context across multiple sensory modalities. J. Neurophysiol. 87, 615–620. https://doi.org/10.1152/jn.00636.2001
- Downar, J., Crawley, A.P., Mikulis, D.J., Davis, K.D., 2000. A multimodal cortical network for the detection of changes in the sensory environment. Nat. Neurosci. 3, 277–283. https://doi.org/10.1038/72991
- Durrleman, S., Pennec, X., Trouvé, A., Thompson, P., Ayache, N., 2008. Inferring brain variability from diffeomorphic deformations of currents: An integrative approach. Med. Image Anal. 12, 626–637. https://doi.org/10.1016/j.media.2008.06.010
- Edwards, P., Hill, D., Little, J., Sahni, V., Hawkes, D., 1995. Medical Image Registration Incorporating Deformations., in: BMVC. pp. 1–10. https://doi.org/10.5244/c.9.69
- Eldar, E., Cohen, J.D., Niv, Y., 2013. The effects of neural gain on attention and learning. Nat. Neurosci. 16, 1146–1153. https://doi.org/10.1038/nn.3428
- Fabri, M., Polonara, G., Mascioli, G., Salvolini, U., Manzoni, T., 2011. Topographical organization of human corpus callosum: An fMRI mapping study. Brain Res. 1370, 99–111. https://doi.org/10.1016/j.brainres.2010.11.039
- Fair, D.A., Dosenbach, N.U.F., Church, J.A., Cohen, A.L., Brahmbhatt, S., Miezin, F.M., Barch, D.M., Raichle, M.E., Petersen, S.E., Schlaggar, B.L., 2007. Development of distinct control networks through segregation and integration. Proc. Natl. Acad. Sci. 104, 13507–13512. https://doi.org/10.1073/PNAS.0705843104
- Faller, J., Doose, J., Sun, X., McIntosh, J.R., Saber, G.T., Lin, Y., Teves, J.B., Blankenship, A., Huffman, S., Goldman, R.I., George, M.S., Brown, T.R., Sajda, P., 2022. Daily prefrontal closed-loop repetitive transcranial magnetic stimulation (rTMS) produces progressive EEG quasi-alpha phase entrainment in depressed adults. Brain Stimul. 15, 458–471. https://doi.org/10.1016/J.BRS.2022.02.008
- Fischl, B., Rajendran, N., Busa, E., Augustinack, J., Hinds, O., Yeo, B.T.T., Mohlberg, H., Amunts, K., Zilles, K., 2008. Cortical folding patterns and predicting cytoarchitecture. Cereb. Cortex 18, 1973–1980. https://doi.org/10.1093/cercor/bhm225
- Fischl, B., Salat, D.H., Busa, E., Albert, M., Dieterich, M., Haselgrove, C., Van Der Kouwe, A., Killiany, R., Kennedy, D., Klaveness, S., Montillo, A., Makris, N., Rosen, B., Dale, A.M., 2002. Whole brain segmentation: Automated labeling of neuroanatomical structures in the human brain. Neuron 33, 341–355. https://doi.org/10.1016/S0896-6273(02)00569-X
- Fischl, B., Sereno, M.I., Tootell, R.B.H.H., Dale, A.M., 1999. High-resolution intersubject averaging and a coordinate system for the cortical surface. Hum. Brain Mapp. 8, 272–284. https://doi.org/10.1002/(SICI)1097-0193(1999)8:4<272::AID-HBM10>3.0.CO;2-4
- Fischl, B., Van Der Kouwe, A., Destrieux, C., Halgren, E., Ségonne, F., Salat, D.H., Busa, E., Seidman, L.J., Goldstein, J., Kennedy, D., Caviness, V., Makris, N., Rosen, B., Dale, A.M., others, Caviness, V., Makris, N., Rosen, B., Dale, A.M., others, 2004. Automatically parcellating the human cerebral cortex. Cereb. Cortex 14, 11–22. https://doi.org/10.1093/cercor/bhg087
- Fox, M.D., Buckner, R.L., White, M.P., Greicius, M.D., Pascual-Leone, A., 2012. Efficacy of

- Transcranial Magnetic Stimulation Targets for Depression Is Related to Intrinsic Functional Connectivity with the Subgenual Cingulate. BPS. https://doi.org/10.1016/j.biopsych.2012.04.028
- Fox, M.D., Snyder, A.Z., Vincent, J.L., Corbetta, M., Essen, D.C. Van, Raichle, M.E., 2005a. The human brain is intrinsically organized into dynamic, anticorrelated functional networks. Proc. Natl. Acad. Sci. 102, 9673–9678. https://doi.org/10.1073/PNAS.0504136102
- Fox, M.D., Snyder, A.Z., Vincent, J.L., Corbetta, M., Van Essen, D.C., Raichle, M.E., Essen, D.C. Van, Raichle, M.E., Van Essen, D.C., Raichle, M.E., 2005b. The human brain is intrinsically organized into dynamic, anticorrelated functional networks. Proc. Natl. Acad. Sci. 102, 9673–9678. https://doi.org/10.1073/PNAS.0504136102
- Friston, K., Mattout, J., Trujillo-Barreto, N., Ashburner, J., Penny, W., 2007. Variational free energy and the Laplace approximation. Neuroimage 34, 220–234. https://doi.org/10.1016/J.NEUROIMAGE.2006.08.035
- Friston, K.J., Buechel, C., Fink, G.R., Morris, J., Rolls, E., Dolan, R.J., 1997. Psychophysiological and Modulatory Interactions in Neuroimaging. Neuroimage 6, 218–229. https://doi.org/10.1006/NIMG.1997.0291
- Friston, K.J., Harrison, L., Penny, W., 2003. Dynamic causal modelling. Neuroimage 19, 1273–1302. https://doi.org/10.1016/S1053-8119(03)00202-7
- Gandhi, S.P., Heeger, D.J., Boynton, G.M., 1999. Spatial attention affects brain activity in human primary visual cortex. Proc. Natl. Acad. Sci. 96, 3314–3319.
- Gerchen, M.F., Bernal-Casas, D., Kirsch, P., 2014. Analyzing task-dependent brain network changes by whole-brain psychophysiological interactions: A comparison to conventional analysis. Hum. Brain Mapp. 35, 5071–5082. https://doi.org/10.1002/hbm.22532
- Gilam, G., Lin, T., Fruchter, E., Hendler, T., 2017. Neural indicators of interpersonal anger as cause and consequence of combat training stress symptoms. Psychol. Med. 47, 1561–1572. https://doi.org/10.1017/S0033291716003354
- Gilzenrat, M.S., Nieuwenhuis, S., Jepma, M., Cohen, J.D., 2010. Pupil diameter tracks changes in control state predicted by the adaptive gain theory of locus coeruleus function. Cogn. Affect. Behav. Neurosci. 10, 252–269. https://doi.org/10.3758/CABN.10.2.252
- Glasser, M.F., Coalson, T.S., Robinson, E.C., Hacker, C.D., Harwell, J., Yacoub, E., Ugurbil, K., Andersson, J., Beckmann, C.F., Jenkinson, M., others, Smith, S.M., Van Essen, D.C., others, 2016. A multi-modal parcellation of human cerebral cortex. Nature 536, 171–178. https://doi.org/10.1038/nature18933
- Glover, G.H., Li, T.-Q., Ress, D., 2000. Image-Based Method for Retrospective Correction of Physiological Motion Effects in fMRI: RETROICOR. https://doi.org/10.1002/1522-2594(200007)44:1<162::AID-MRM23>3.0.CO;2-E
- Goense, J., Merkle, H., Logothetis, N.K., 2012. High-Resolution fMRI Reveals Laminar Differences in Neurovascular Coupling between Positive and Negative BOLD Responses. Neuron 76, 629–639. https://doi.org/10.1016/j.neuron.2012.09.019
- Goldman, R.I., Wei, C.-Y.Y., Philiastides, M.G., Gerson, A.D., Friedman, D., Brown, T.R., Sajda, P., 2009. Single-trial discrimination for integrating simultaneous EEG and fMRI: Identifying cortical areas contributing to trial-to-trial variability in the auditory oddball task. Neuroimage 47, 136–147. https://doi.org/10.1016/j.neuroimage.2009.03.062

- Good, C.D., Johnsrude, I.S., Ashburner, J., Henson, R.N.A., Friston, K.J., Frackowiak, R.S.J., 2001. A voxel-based morphometric study of ageing in 465 normal adult human brains. Neuroimage 14, 21–36. https://doi.org/10.1006/nimg.2001.0786
- Gordon, E.M., Lynch, C.J., Gratton, C., Laumann, T.O., Gilmore, A.W., Greene, D.J., Ortega, M., Nguyen, A.L., Schlaggar, B.L., Petersen, S.E., Dosenbach, N.U.F., Nelson, S.M., 2018. Three Distinct Sets of Connector Hubs Integrate Human Brain Function. Cell Rep. 24, 1687-1695.e4. https://doi.org/10.1016/J.CELREP.2018.07.050
- Goutte, C., Nielsen, F.A., Hansen, K.H., 2000. Modeling the hemodynamic response in fMRI using smooth FIR filters. IEEE Trans. Med. Imaging 19, 1188–1201.
- Grenander, U., Miller, M.I., 1998. Computational anatomy: an emerging discipline. Q. Appl. Math. 56, 617–694. https://doi.org/10.1090/qam/1668732
- Greve, D.N., Fischl, B., 2009. Accurate and robust brain image alignment using boundary-based registration. Neuroimage 48, 63–72.
- Groot, J.M., Boayue, N.M., Csifcsák, G., Boekel, W., Huster, R., Forstmann, B.U., Mittner, M., 2021. Probing the neural signature of mind wandering with simultaneous fMRI-EEG and pupillometry. Neuroimage 224, 117412. https://doi.org/10.1016/j.neuroimage.2020.117412
- Grueschow, M., Stenz, N., Thörn, H., Ehlert, U., Breckwoldt, J., Brodmann Maeder, M., Exadaktylos, A.K., Bingisser, R., Ruff, C.C., Kleim, B., 2021. Real-world stress resilience is associated with the responsivity of the locus coeruleus. Nat. Commun. 12, 2275. https://doi.org/10.1038/s41467-021-22509-1
- Guo, H., Rangarajan, A., Joshi, S.C., 2005. 3-D diffeomorphic shape registration on hippocampal data sets. Lect. Notes Comput. Sci. (including Subser. Lect. Notes Artif. Intell. Lect. Notes Bioinformatics) 3750 LNCS, 984–991. https://doi.org/10.1007/11566489\_121
- Han, X., Fischl, B., 2007. Atlas renormalization for improved brain MR image segmentation across scanner platforms. IEEE Trans. Med. Imaging 26, 479–486. https://doi.org/10.1109/TMI.2007.893282
- Han, X., Jovicich, J., Salat, D., van der Kouwe, A., Quinn, B., Czanner, S., Busa, E., Pacheco, J., Albert, M., Killiany, R., Maguire, P., Rosas, D., Makris, N., Dale, A., Dickerson, B., Fischl, B., 2006. Reliability of MRI-derived measurements of human cerebral cortical thickness: The effects of field strength, scanner upgrade and manufacturer. Neuroimage 32, 180–194. https://doi.org/10.1016/J.NEUROIMAGE.2006.02.051
- Harel, N., Lee, S.-P., Nagaoka, T., Kim, D.-S., Kim, S.-G., 2002. Origin of negative blood oxygenation level—dependent fMRI signals. J. Cereb. blood flow Metab. 22, 908–917.
- Harsay, H.A., Spaan, M., Wijnen, J.G., Ridderinkhof, K.R., 2012. Error awareness and salience processing in the oddball task: shared neural mechanisms. Front. Hum. Neurosci. 6, 246. https://doi.org/10.3389/FNHUM.2012.00246
- Hawco, C., Voineskos, A.N., Steeves, J.K.E., Dickie, E.W., Viviano, J.D., Downar, J., Blumberger, D.M., Daskalakis, Z.J., 2018. Spread of activity following TMS is related to intrinsic resting connectivity to the salience network: A concurrent TMS-fMRI study. Cortex 108, 160–172. https://doi.org/10.1016/J.CORTEX.2018.07.010
- He, H., Ettehadi, N., Shmuel, A., Razlighi, Q.R., 2022. Evidence suggesting common mechanisms underlie contralateral and ipsilateral negative BOLD responses in the human visual cortex. Neuroimage 262, 119440.

- https://doi.org/10.1016/J.NEUROIMAGE.2022.119440
- He, H., Hong, L., Sajda, P., 2021. An Automatic and Subject-specific Method for Locus Coeruleus Localization and BOLD Activity Extraction, in: Proc. Intl. Soc. Mag. Reson. Med.
- He, H., Razlighi, Q., 2020. Volumetric Registration of Brain Cortical Regions by Automatic Landmark Matching and Large Deformation Diffeomorphisms, in: Proceedings International Symposium on Biomedical Imaging. IEEE Computer Society, pp. 1412–1415. https://doi.org/10.1109/ISBI45749.2020.9098572
- He, H., Razlighi, Q.R., 2022. Landmark-guided region-based spatial normalization for functional magnetic resonance imaging. Hum. Brain Mapp. 43, 3524–3544. https://doi.org/10.1002/HBM.25865
- He, H.I., Hong, L., Sajda, P., 2023. Pupillary response is associated with the reset and switching of functional brain networks during salience processing. PLOS Comput. Biol. 19, e1011081. https://doi.org/10.1371/JOURNAL.PCBI.1011081
- Heinemann, L., Kleinschmidt, A., Müller, N.G., 2009. Exploring BOLD changes during spatial attention in non-stimulated visual cortex. PLoS One 4. https://doi.org/10.1371/JOURNAL.PONE.0005560
- Hermans, E.J., Van Marle, H.J.F., Ossewaarde, L., Henckens, M.J.A.G., Qin, S., Van Kesteren, M.T.R., Schoots, V.C., Cousijn, H., Rijpkema, M., Oostenveld, R., Fernández, G., 2011. Stress-related noradrenergic activity prompts large-scale neural network reconfiguration. Science (80-.). 334, 1151–1153. https://doi.org/10.1126/SCIENCE.1209603/SUPPL\_FILE/HERMANS.SOM.PDF
- Hong, L., He, H., Sajda, P., 2022. Pupil-linked phasic arousal relates to the reduction of response inhibition: inferences from a simultaneous pupillometry and EEG-fMRI study. bioRxiv 2022.08.22.504728. https://doi.org/10.1101/2022.08.22.504728
- Hu, D., Huang, L., 2015. Negative hemodynamic response in the cortex: Evidence opposing neuronal deactivation revealed via optical imaging and electrophysiological recording. J. Neurophysiol. 114, 2152–2161. https://doi.org/10.1152/JN.00246.2015
- Hubbard, C.S., Labus, J.S., Bueller, J., Stains, J., Suyenobu, B., Dukes, G.E., Kelleher, D.L.,
  Tillisch, K., Naliboff, B.D., Mayer, E.A., 2011. Corticotropin-Releasing Factor Receptor 1
  Antagonist Alters Regional Activation and Effective Connectivity in an Emotional–Arousal
  Circuit during Expectation of Abdominal Pain. J. Neurosci. 31, 12491–12500.
  https://doi.org/10.1523/JNEUROSCI.1860-11.2011
- Huettel, S.A., McCarthy, G., 2000. Evidence for a refractory period in the hemodynamic response to visual stimuli as measured by MRI. Neuroimage 11, 547–553. https://doi.org/10.1006/nimg.2000.0553
- Iadecola, C., Yang, G., Ebner, T.J., Chen, G., 1997. Local and propagated vascular responses evoked by focal synaptic activity in cerebellar cortex. J. Neurophysiol. 78, 651–659. https://doi.org/10.1152/JN.1997.78.2.651
- Iseger, T.A., Van Bueren, N.E.R., Kenemans, J.L., Gevirtz, R., Arns, M., 2019. A frontal-vagal network theory for Major Depressive Disorder: Implications for optimizing neuromodulation techniques. https://doi.org/10.1016/j.brs.2019.10.006
- Isoda, M., Hikosaka, O., 2007. Switching from automatic to controlled action by monkey medial frontal cortex. Nat. Neurosci. 10, 240–248. https://doi.org/10.1038/nn1830

- Jack, C.R., Petersen, R.C., Xu, Y.C., Waring, S.C., O'Brien, P.C., Tangalos, E.G., Smith, G.E., Ivnik, R.J., Kokmen, E., 1997. Medial temporal atrophy on MRI in normal aging and very mild Alzheimer's disease. Neurology 49, 786–794. https://doi.org/10.1212/WNL.49.3.786
- Jenkinson, M., Bannister, P., Brady, M., Smith, S., 2002. Improved optimization for the robust and accurate linear registration and motion correction of brain images. Neuroimage 17, 825–841.
- Joshi, A.A., Shattuck, D.W., Thompson, P.M., Leahy, R.M., 2007. Surface-constrained volumetric brain registration using harmonic mappings. IEEE Trans. Med. Imaging 26, 1657–1668. https://doi.org/10.1109/TMI.2007.901432
- Joshi, A.A., Shattuck, D.W., Thompson, P.M., Leahy, R.M., 2005. A framework for registration, statistical characterization and classification of cortically constrained functional imaging data, in: Biennial International Conference on Information Processing in Medical Imaging. Springer, Berlin, Heidelberg, pp. 186–196. https://doi.org/10.1007/11505730\_16
- Joshi, S., Gold, J.I., 2020. Pupil size as a window on neural substrates of cognition. Trends Cogn. Sci. 24, 466–480. https://doi.org/10.1016/j.tics.2020.03.005
- Joshi, S., Li, Y., Kalwani, R.M., Gold, J.I., 2016. Relationships between pupil diameter and neuronal activity in the locus coeruleus, colliculi, and cingulate cortex. Neuron 89, 221–234. https://doi.org/10.1016/j.neuron.2015.11.028
- Joshi, S.C.S.C., Miller, M.I.M.I., 2000. Landmark matching via large deformation diffeomorphisms. IEEE Trans. image Process. 9, 1357–70. https://doi.org/10.1109/83.855431
- Joshi, S.H., Cabeen, R.P., Joshi, A.A., Sun, B., Dinov, I., Narr, K.L., Toga, A.W., Woods, R.P., 2012. Diffeomorphic sulcal shape analysis on the cortex. IEEE Trans. Med. Imaging 31, 1195–1212. https://doi.org/10.1109/TMI.2012.2186975
- Jung, T.-P., Makeig, S., Westerfield, M., Townsend, J., Courchesne, E., Sejnowski, T.J., 2000. Removal of eye activity artifacts from visual event-related potentials in normal and clinical subjects. Clin. Neurophysiol. 111, 1745–1758.
- Kastrup, A., Baudewig, J., Schnaudigel, S., Huonker, R., Becker, L., Sohns, J.M., Dechent, P., Klingner, C., Witte, O.W., 2008. Behavioral correlates of negative BOLD signal changes in the primary somatosensory cortex. Neuroimage 41, 1364–1371. https://doi.org/10.1016/j.neuroimage.2008.03.049
- Keren, N.I., Lozar, C.T., Harris, K.C., Morgan, P.S., Eckert, M.A., 2009. In vivo mapping of the human locus coeruleus. Neuroimage 47, 1261–1267. https://doi.org/10.1016/j.neuroimage.2009.06.012
- Kim, H., 2014. Involvement of the dorsal and ventral attention networks in oddball stimulus processing: A meta-analysis. Hum. Brain Mapp. 35, 2265–2284. https://doi.org/10.1002/HBM.22326
- Klein, A., Andersson, J., Ardekani, B.A., Ashburner, J., Avants, B., Chiang, M.C., Christensen, G.E., Collins, D.L., Gee, J., Hellier, P., Song, J.H., Jenkinson, M., Lepage, C., Rueckert, D., Thompson, P., Vercauteren, T., Woods, R.P., Mann, J.J., Parsey, R. V., 2009. Evaluation of 14 nonlinear deformation algorithms applied to human brain MRI registration. Neuroimage 46, 786–802. https://doi.org/10.1016/j.neuroimage.2008.12.037
- Klingner, C.M., Hasler, C., Brodoehl, S., Witte, O.W., 2010. Dependence of the negative BOLD response on somatosensory stimulus intensity. Neuroimage 53, 189–195.

- https://doi.org/10.1016/J.NEUROIMAGE.2010.05.087
- Köhler, S., Bär, K.-J., Wagner, G., 2016. Differential involvement of brainstem noradrenergic and midbrain dopaminergic nuclei in cognitive control. Hum. Brain Mapp. 37, 2305–2318.
- Krebs, R.M., Park, H.R.P., Bombeke, K., Boehler, C.N., 2018. Modulation of locus coeruleus activity by novel oddball stimuli. Brain Imaging Behav. 12, 577–584. https://doi.org/10.1007/S11682-017-9700-4/FIGURES/2
- Kuang, D., 2019. Cycle-consistent training for reducing negative jacobian determinant in deep registration networks, in: International Workshop on Simulation and Synthesis in Medical Imaging. Springer, pp. 120–129. https://doi.org/10.1007/978-3-030-32778-1\_13
- Kucyi, A., Daitch, A., Raccah, O., Zhao, B., Zhang, C., Esterman, M., Zeineh, M., Halpern, C.H., Zhang, K., Zhang, J., Parvizi, J., 2020. Electrophysiological dynamics of antagonistic brain networks reflect attentional fluctuations. Nat. Commun. 2020 111 11, 1–14. https://doi.org/10.1038/s41467-019-14166-2
- Kucyi, A., Parvizi, J., 2020. Pupillary dynamics link spontaneous and task-evoked activations recorded directly from human insula. J. Neurosci. 40, 6207–6218. https://doi.org/10.1523/JNEUROSCI.0435-20.2020
- Lee, T.H., Kim, S.H., Katz, B., Mather, M., 2020. The Decline in Intrinsic Connectivity Between the Salience Network and Locus Coeruleus in Older Adults: Implications for Distractibility. Front. Aging Neurosci. 12, 2. https://doi.org/10.3389/FNAGI.2020.00002/XML/NLM
- Lepore, N., Joshi, A.A., Leahy, R.M., Brun, C., Chou, Y.-Y., Pennec, X., Lee, A.D., Barysheva, M., De Zubicaray, G.I., Wright, M.J., McMahon, K.L., Toga, A.W., Thompson, P.M., 2010. A new combined surface and volume registration, in: Medical Imaging 2010: Image Processing. International Society for Optics and Photonics, p. 76231E. https://doi.org/10.1117/12.844434
- Liston, C., Chen, A.C., Zebley, B.D., Drysdale, A.T., Gordon, R., Leuchter, B., Voss, H.U., Casey, B.J., Etkin, A., Dubin, M.J., 2014. Default Mode Network Mechanisms of Transcranial Magnetic Stimulation in Depression. Biol. Psychiatry 76, 517–526. https://doi.org/10.1016/J.BIOPSYCH.2014.01.023
- Little, J.A., Hill, D.L.G., Hawkes, D.J., 1997. Deformations Incorporating Rigid Structures. Comput. Vis. Image Underst. 66, 223–232. https://doi.org/10.1006/cviu.1997.0608
- Liu, X., Gerraty, R.T., Grinband, J., Parker, D., Razlighi, Q.R., 2017. Brain atrophy can introduce age-related differences in BOLD response. Hum. Brain Mapp. 38, 3402–3414. https://doi.org/10.1002/hbm.23597
- Liu, Y., Shen, H., Zhou, Z., Hu, D., 2011. Sustained negative BOLD response in human fMRI finger tapping task. PLoS One 6. https://doi.org/10.1371/JOURNAL.PONE.0023839
- Logothetis, N.K., 2008. What we can do and what we cannot do with fMRI. Nature 453, 869–878. https://doi.org/10.1038/NATURE06976
- Long, N.M., Kuhl, B.A., 2018. Bottom-up and top-down factors differentially influence stimulus representations across large-scale attentional networks. J. Neurosci. 38, 2495–2504. https://doi.org/10.1523/JNEUROSCI.2724-17.2018
- Mäki-Marttunen, V., Espeseth, T., 2021. Uncovering the locus coeruleus: comparison of localization methods for functional analysis. Neuroimage 224, 117409.

- https://doi.org/10.1016/j.neuroimage.2020.117409
- Mandeville, J.B., Marota, J.J.A., 1999. Vascular filters of functional MRI: Spatial localization using BOLD and CBV contrast. Magn. Reson. Med. 42, 591–598. https://doi.org/10.1002/(SICI)1522-2594(199909)42:3<591::AID-MRM23>3.0.CO;2-8
- Mather, M., Clewett, D., Sakaki, M., Harley, C.W., 2016. Norepinephrine ignites local hotspots of neuronal excitation: How arousal amplifies selectivity in perception and memory. Behav. Brain Sci. 39. https://doi.org/10.1017/S0140525X15000667
- Mather, M., Harley, C.W., 2016. The locus coeruleus: essential for maintaining cognitive function and the aging brain. Trends Cogn. Sci. 20, 214–226. https://doi.org/10.1016/j.tics.2016.01.001
- Mayeli, A., Al Zoubi, O., Misaki, M., Stewart, J.L., Zotev, V., Luo, Q., Phillips, R., Fischer, S., Götz, M., Paulus, M.P., 2020. Integration of simultaneous resting-state electroencephalography, functional magnetic resonance imaging, and eye-tracker methods to determine and verify electroencephalography vigilance measure. Brain Connect. 10, 535–546.
- Mccormick, D.A., Nestvogel, D.B., He, B.J., 2020. Neuromodulation of brain state and behavior. Annu. Rev. Neurosci. 43, 391–415. https://doi.org/10.1146/annurev-neuro-100219
- McGinley, M.J., David, S. V., McCormick, D.A., 2015. Cortical membrane potential signature of optimal states for sensory signal detection. Neuron 87, 179–192. https://doi.org/10.1016/J.NEURON.2015.05.038
- Menon, R.S., Ogawa, S., Hu, X., Strupp, J.P., Anderson, P., Uğurbil, K., 1995. BOLD Based Functional MRI at 4 Tesla Includes a Capillary Bed Contribution: Echo-Planar Imaging Correlates with Previous Optical Imaging Using Intrinsic Signals. Magn. Reson. Med. 33, 453–459. https://doi.org/10.1002/MRM.1910330323
- Menon, V., 2015. Salience Network, Brain Mapping: An Encyclopedic Reference. Elsevier Inc. https://doi.org/10.1016/B978-0-12-397025-1.00052-X
- Menon, V., 2011. Large-scale brain networks and psychopathology: a unifying triple network model. Trends Cogn. Sci. 15, 483–506. https://doi.org/10.1016/J.TICS.2011.08.003
- Menon, V., Uddin, L.Q., 2010. Saliency, switching, attention and control: a network model of insula function. Brain Struct. Funct. 214, 655–667. https://doi.org/10.1007/S00429-010-0262-0
- Miller, M.I., Beg, M.F., Ceritoglu, C., Stark, C., 2005. Increasing the power of functional maps of the medial temporal lobe by using large deformation diffeomorphic metric mapping. Proc. Natl. Acad. Sci. 102, 9685–9690. https://doi.org/10.1073/pnas.0503892102
- Minzenberg, M.J., Watrous, A.J., Yoon, J.H., Ursu, S., Carter, C.S., 2008. Modafinil shifts human locus coeruleus to low-tonic, high-phasic activity during functional MRI. Science (80-.). 322, 1700–1702.
  - https://doi.org/10.1126/SCIENCE.1164908/SUPPL\_FILE/MINZENBERG\_SOM.PDF
- Mittner, M., Hawkins, G.E., Boekel, W., Forstmann, B.U., 2016. A neural model of mind wandering. Trends Cogn. Sci. 20, 570–578. https://doi.org/10.1016/j.tics.2016.06.004
- Morey, R.A., Dunsmoor, J.E., Haswell, C.C., Brown, V.M., Vora, A., Weiner, J., Stjepanovic, D., Wagner, H.R., Mid-Atlantic, V.A., LaBar, K.S., Brancu, M., Marx, C.E., Naylor, J.C., Van Voorhees, E., Taber, K.H., Beckham, J.C., Calhoun, P.S., Fairbank, J.A., Szabo, S.T., 2015. Fear learning circuitry is biased toward generalization of fear associations in posttraumatic

- stress disorder. Transl. Psychiatry 2015 512 5, e700–e700. https://doi.org/10.1038/tp.2015.196 Müller, N.G., Kleinschmidt, A., 2004. The attentional 'spotlight's' penumbra: center-surround modulation in striate cortex. Neuroreport 15, 977–980.
- Mullinger, K.J., Mayhew, S.D., Bagshaw, A.P., Bowtell, R., Francis, S.T., 2014. Evidence that the negative BOLD response is neuronal in origin: A simultaneous EEG-BOLD-CBF study in humans. Neuroimage 94, 263–274. https://doi.org/10.1016/j.neuroimage.2014.02.029
- Muraskin, J., Brown, T.R., Walz, J.M., Tu, T., Conroy, B., Goldman, R.I., Sajda, P., 2018. A multimodal encoding model applied to imaging decision-related neural cascades in the human brain. Neuroimage 180, 211–222. https://doi.org/10.1016/j.neuroimage.2017.06.059
- Murphy, P.R., O'Connell, R.G., O'Sullivan, M., Robertson, I.H., Balsters, J.H., 2014. Pupil diameter covaries with BOLD activity in human locus coeruleus. Hum. Brain Mapp. 35, 4140–4154. https://doi.org/10.1002/hbm.22466
- Murphy, P.R., Robertson, I.H., Balsters, J.H., O'connell, R.G., 2011. Pupillometry and P3 index the locus coeruleus–noradrenergic arousal function in humans. Psychophysiology 48, 1532–1543. https://doi.org/10.1111/J.1469-8986.2011.01226.X
- Nakajima, M., Halassa, M.M., 2017. Thalamic control of functional cortical connectivity. Curr. Opin. Neurobiol. 44, 127–131.
- Napadow, V., Dhond, R., Kennedy, D., Hui, K.K.S., Makris, N., 2006. Automated Brainstem Coregistration (ABC) for MRI. Neuroimage 32, 1113–1119. https://doi.org/10.1016/j.neuroimage.2006.05.050
- Neumann, J., Lohmann, G., 2003. Bayesian second-level analysis of functional magnetic resonance images. Neuroimage 20, 1346–1355. https://doi.org/10.1016/S1053-8119(03)00443-9
- Ogawa, S., Tank, D.W., Menon, R., Ellermann, J.M., Kim, S.G., Merkle, H., Ugurbil, K., 1992. Intrinsic signal changes accompanying sensory stimulation: Functional brain mapping with magnetic resonance imaging. Proc. Natl. Acad. Sci. U. S. A. 89, 5951–5955. https://doi.org/10.1073/PNAS.89.13.5951
- Oostenveld, R., Fries, P., Maris, E., Schoffelen, J.M., 2011. FieldTrip: Open source software for advanced analysis of MEG, EEG, and invasive electrophysiological data. Comput. Intell. Neurosci. 2011. https://doi.org/10.1155/2011/156869
- Pantazatos, S.P., McIntosh, J.R., Saber, G.T., Sun, X., Doose, J., Faller, J., Lin, Y., Teves, J.B., Blankenship, A., Huffman, S., Goldman, R.I., George, M.S., Sajda, P., Brown, T.R., 2023. The timing of transcranial magnetic stimulation relative to the phase of prefrontal alpha EEG modulates downstream target engagement. Brain Stimul. 16, 830–839. https://doi.org/10.1016/J.BRS.2023.05.007
- Pantazatos, S.P., McIntosh, J.R., Saber, G.T., Sun, X., Doose, J., Faller, J., Lin, Y., Teves, J.B., Blankenship, A., Huffman, S., Goldman, R.I., George, M.S., Sajda, P., Brown, T.R., 2022. Functional and effective connectivity between dorsolateral prefrontal and subgenual anterior cingulate cortex depends on the timing of transcranial magnetic stimulation relative to the phase of prefrontal alpha EEG. bioRxiv 1–19. https://doi.org/10.1101/2022.02.14.480466
- Parker, D., Liu, X., Razlighi, Q.R., 2017. Optimal slice timing correction and its interaction with fMRI parameters and artifacts. Med. Image Anal. 35, 434–445.

- https://doi.org/10.1016/j.media.2016.08.006
- Parker, D.B., Razlighi, Q.R., 2019a. The Benefit of Slice Timing Correction in Common fMRI Preprocessing Pipelines. Front. Neurosci. 13, 821. https://doi.org/10.3389/fnins.2019.00821
- Parker, D.B., Razlighi, Q.R., 2019b. Task-evoked Negative BOLD Response and Functional Connectivity in the Default Mode Network are Representative of Two Overlapping but Separate Neurophysiological Processes. Sci. Reports 2019 91 9, 1–17. https://doi.org/10.1038/s41598-019-50483-8
- Parra, L.C., Spence, C.D., Gerson, A.D., Sajda, P., 2005. Recipes for the linear analysis of EEG. Neuroimage 28, 326–341. https://doi.org/10.1016/j.neuroimage.2005.05.032
- Pessoa, L., Gutierrez, E., Bandettini, P., Ungerleider, L., 2002. Neural correlates of visual working memory: fMRI amplitude predicts task performance. Neuron 35, 975–987. https://doi.org/10.1016/S0896-6273(02)00817-6
- Philiastides, M.G., Tu, T., Sajda, P., 2021. Inferring Macroscale Brain Dynamics via Fusion of Simultaneous EEG-fMRI. Annu. Rev. Neurosci. 44, 315–334. https://doi.org/10.1146/annurev-neuro-100220-093239
- Pitiot, A., Malandain, G., Bardinet, E., Thompson, P.M., 2003. Piecewise affine registration of biological images, in: WBIR. pp. 91–101.
- Poe, G.R., Foote, S., Eschenko, O., Johansen, J.P., Bouret, S., Aston-Jones, G., Harley, C.W., Manahan-Vaughan, D., Weinshenker, D., Valentino, R., Berridge, C., Chandler, D.J., Waterhouse, B., Sara, S.J., others, 2020. Locus coeruleus: a new look at the blue spot. Nat. Rev. Neurosci. 21, 644–659. https://doi.org/10.1038/s41583-020-0360-9
- Porras, A.R., Paniagua, B., Ensel, S., Keating, R., Rogers, G.F., Enquobahrie, A., Linguraru, M.G., 2018. Locally Affine Diffeomorphic Surface Registration and Its Application to Surgical Planning of Fronto-Orbital Advancement. IEEE Trans. Med. Imaging 37, 1690–1700. https://doi.org/10.1109/TMI.2018.2816402
- Postelnicu, G., Zollei, L., Fischl, B., 2009. Combined volumetric and surface registration. IEEE Trans. Med. Imaging 28, 508–522. https://doi.org/10.1109/TMI.2008.2004426
- Raccah, O., Daitch, A.L., Kucyi, A., Parvizi, J., 2018. Direct cortical recordings suggest temporal order of task-evoked responses in human dorsal attention and default networks. J. Neurosci. 38, 10305–10313. https://doi.org/10.1523/JNEUROSCI.0079-18.2018
- Rafiei, F., Rahnev, D., 2022. TMS Does Not Increase BOLD Activity at the Site of Stimulation: A Review of All Concurrent TMS-fMRI Studies. eNeuro. https://doi.org/10.1523/ENEURO.0163-22.2022
- Razlighi, Q.R., 2016. Region-based spatial normalization for aging research with fmri, in: 22nd Annu. Meeting of the OHBM, Geneva, Switzerland.
- Razlighi, Q.R., Habeck, C., Steffener, J., Gazes, Y., Zahodne, L.B., Mackay-Brandt, A., Stern, Y., 2014. Unilateral disruptions in the default network with aging in native space. Brain Behav. 4, 143–157. https://doi.org/10.1002/BRB3.202
- Razlighi, Q.R., Oh, H., Habeck, C., O'Shea, D., Gazes, E., Eich, T., Parker, D.B., Lee, S., Stern, Y., 2017. Dynamic Patterns of Brain Structure–Behavior Correlation Across the Lifespan. Cereb. Cortex 27, 3586–3599. https://doi.org/10.1093/CERCOR/BHW179
- Reuter, M., Schmansky, N.J., Rosas, H.D., Fischl, B., 2012. Within-subject template estimation for unbiased longitudinal image analysis. Neuroimage 61, 1402–1418.

- https://doi.org/10.1016/J.NEUROIMAGE.2012.02.084
- Robertson, I.H., 2013. A noradrenergic theory of cognitive reserve: implications for Alzheimer's disease. Neurobiol. Aging 34, 298–308. https://doi.org/10.1016/J.NEUROBIOLAGING.2012.05.019
- Ross, J.A., Van Bockstaele, E.J., 2021. The Locus Coeruleus- Norepinephrine System in Stress and Arousal: Unraveling Historical, Current, and Future Perspectives. Front. Psychiatry 0, 1581. https://doi.org/10.3389/FPSYT.2020.601519
- Sadaghiani, S., D'Esposito, M., 2015. Functional characterization of the cingulo-opercular network in the maintenance of tonic alertness. Cereb. Cortex 25, 2763–2773. https://doi.org/10.1093/CERCOR/BHU072
- Sadaghiani, S., Scheeringa, R., Lehongre, K., Morillon, B., Giraud, A.-L.L., d'Esposito, M., Kleinschmidt, A., 2012. Alpha-band phase synchrony is related to activity in the frontoparietal adaptive control network. J. Neurosci. 32, 14305–14310. https://doi.org/10.1523/JNEUROSCI.1358-12.2012
- Sakai, K., 2008. Task set and prefrontal cortex. Annu. Rev. Neurosci. 31, 219–245. https://doi.org/10.1146/ANNUREV.NEURO.31.060407.125642
- Saladin, K.S., McFarland, R.K., 2008. Human anatomy. McGraw-Hill New York.
- Sasaki, M., Shibata, E., Tohyama, K., Takahashi, J., Otsuka, K., Tsuchiya, K., Takahashi, S., Ehara, S., Terayama, Y., Sakai, A., 2006. Neuromelanin magnetic resonance imaging of locus ceruleus and substantia nigra in Parkinson's disease. Neuroreport 17, 1215–1218. https://doi.org/10.1097/01.WNR.0000227984.84927.A7
- Schaefer, A., Kong, R., Gordon, E.M., Laumann, T.O., Zuo, X.-N., Holmes, A.J., Eickhoff, S.B., Yeo, B.T.T., 2018. Local-Global Parcellation of the Human Cerebral Cortex from Intrinsic Functional Connectivity MRI. Cereb. Cortex 28, 3095–3114. https://doi.org/10.1093/CERCOR/BHX179
- Schäfer, K., Blankenburg, F., Kupers, R., Grüner, J.M., Law, I., Lauritzen, M., Larsson, H.B.W., 2012. Negative BOLD signal changes in ipsilateral primary somatosensory cortex are associated with perfusion decreases and behavioral evidence for functional inhibition. Neuroimage 59, 3119–3127. https://doi.org/10.1016/j.neuroimage.2011.11.085
- Schneider, M., Hathway, P., Leuchs, L., Sämann, P.G., Czisch, M., Spoormaker, V.I., 2016. Spontaneous pupil dilations during the resting state are associated with activation of the salience network. Neuroimage 139, 189–201. https://doi.org/10.1016/J.NEUROIMAGE.2016.06.011
- Schwarz, L.A., Luo, L., 2015. Organization of the locus coeruleus-norepinephrine system. Curr. Biol. 25, R1051--R1056.
- Seeley, W.W., Menon, V., Schatzberg, A.F., Keller, J., Glover, G.H., Kenna, H., Reiss, A.L., Greicius, M.D., 2007. Dissociable intrinsic connectivity networks for salience processing and executive control. J. Neurosci. 27, 2349–2356. https://doi.org/10.1523/JNEUROSCI.5587-06.2007
- Shepard, D., 1968. A two-dimensional interpolation function for irregularly-spaced data, in: Proceedings of the 1968 23rd ACM National Conference. pp. 517–524. https://doi.org/10.1145/800186.810616
- Shine, J.M., 2019. Neuromodulatory influences on integration and segregation in the brain.

- Trends Cogn. Sci. 23, 572–583. https://doi.org/10.1016/j.tics.2019.04.002
- Shmuel, A., Augath, M., Oeltermann, A., Logothetis, N.K., 2006. Negative functional MRI response correlates with decreases in neuronal activity in monkey visual area V1. Nat. Neurosci. 9, 569–577. https://doi.org/10.1038/NN1675
- Shmuel, A., Augath, M., Rounis, E., Logothetis, N., Smirnakis, S., 2003. Negative BOLD response ipsilateral to the visual stimulus; origin is not blood stealing, in: 9th International Conference on Functional Mapping of the Human Brain (HBM 2003). pp. e570--e571.
- Shmuel, A., Yacoub, E., Pfeuffer, J., Van de Moortele, P.F., Adriany, G., Hu, X., Ugurbil, K., 2002. Sustained negative BOLD, blood flow and oxygen consumption response and its coupling to the positive response in the human brain. Neuron 36, 1195–1210. https://doi.org/10.1016/S0896-6273(02)01061-9
- Shomstein, S., Yantis, S., 2004. Control of attention shifts between vision and audition in human cortex. J. Neurosci. 24, 10702–10706. https://doi.org/10.1523/JNEUROSCI.2939-04.2004
- Siddiqi, S.H., Kording, K.P., Parvizi, J., Fox, M.D., 2022. Causal mapping of human brain function. Nat. Rev. Neurosci. 2022 236 23, 361–375. https://doi.org/10.1038/s41583-022-00583-8
- Simonovsky, M., Gutiérrez-Becker, B., Mateus, D., Navab, N., Komodakis, N., 2016. A deep metric for multimodal registration, in: Medical Image Computing and Computer-Assisted Intervention-MICCAI 2016: 19th International Conference, Athens, Greece, October 17-21, 2016, Proceedings, Part III 19. Springer, pp. 10–18.
- Simpson, G. V, Weber, D.L., Dale, C.L., Pantazis, D., Bressler, S.L., Leahy, R.M., Luks, T.L., 2011. Dynamic activation of frontal, parietal, and sensory regions underlying anticipatory visual spatial attention. J. Neurosci. 31, 13880–13889. https://doi.org/10.1523/JNEUROSCI.1519-10.2011
- Smith, A.T., Singh, K.D., Greenlee, M.W., 2000. Attentional suppression of activity in the human visual cortex. Neuroreport 11.
- Smith, A.T., Williams, A.L., Singh, K.D., 2004. Negative BOLD in the visual cortex: Evidence against blood stealing. Hum. Brain Mapp. 21, 213. https://doi.org/10.1002/HBM.20017
- Smith, S.M., 2002. Fast robust automated brain extraction. Hum. Brain Mapp. 17, 143–155.
- Smith, S.M., Jenkinson, M., Woolrich, M.W., Beckmann, C.F., Behrens, T.E.J., Johansen-Berg, H., Bannister, P.R., De Luca, M., Drobnjak, I., Flitney, D.E., Niazy, R.K., Saunders, J., Vickers, J., Zhang, Y., De Stefano, N., Brady, J.M., Matthews, P.M., 2004. Advances in functional and structural MR image analysis and implementation as FSL. Neuroimage 23, S208–S219. https://doi.org/10.1016/j.neuroimage.2004.07.051
- Sommer, S., Nielsen, M., Lauze, F., Pennec, X., 2011. A multi-scale kernel bundle for LDDMM: Towards sparse deformation description across space and scales, in: Biennial International Conference on Information Processing in Medical Imaging. pp. 624–635. https://doi.org/10.1007/978-3-642-22092-0\_51
- Spadone, S., Betti, V., Sestieri, C., Pizzella, V., Corbetta, M., Della Penna, S., 2021. Spectral signature of attentional reorienting in the human brain. Neuroimage 118616.
- Sridharan, D., Levitin, D.J., Menon, V., 2008. A critical role for the right fronto-insular cortex in switching between central-executive and default-mode networks. Proc. Natl. Acad. Sci. 105, 12569–12574. https://doi.org/10.1073/pnas.0800005105

- Stefanovic, B., Warnking, J.M., Pike, G.B., 2004. Hemodynamic and metabolic responses to neuronal inhibition. Neuroimage 22, 771–778. https://doi.org/10.1016/j.neuroimage.2004.01.036
- Sun, W., Tang, Y., Qiao, Y., Ge, X., Mather, M., Ringman, J.M., Shi, Y., 2020. A probabilistic atlas of locus coeruleus pathways to transentorhinal cortex for connectome imaging in Alzheimer's disease. Neuroimage 223, 117301. https://doi.org/10.1016/J.NEUROIMAGE.2020.117301
- Sydnor, V.J., Cieslak, M., Duprat, R., Deluisi, J., Flounders, M.W., Long, H., Scully, M., Balderston, N.L., Sheline, Y.I., Bassett, D.S., Satterthwaite, T.D., Oathes, D.J., 2022. Cortical-subcortical structural connections support transcranial magnetic stimulation engagement of the amygdala. Sci. Adv. 8, 5803.
  - https://doi.org/10.1126/SCIADV.ABN5803/SUPPL\_FILE/SCIADV.ABN5803\_SM.PDF
- Tardiff, N., Medaglia, J.D., Bassett, D.S., Thompson-Schill, S.L., 2021. The modulation of brain network integration and arousal during exploration. Neuroimage 240, 118369. https://doi.org/10.1016/J.NEUROIMAGE.2021.118369
- Thirion, J.P., 1998. Image matching as a diffusion process: An analogy with Maxwell's demons. Med. Image Anal. 2, 243–260. https://doi.org/10.1016/S1361-8415(98)80022-4
- Thompson, Da.W., 1992. On Growth and Form. Cambridge University Press, Cambridge. https://doi.org/10.1017/CBO9781107325852
- Tisserand, D.J., Jolles, J., 2003. On the involvement of prefrontal networks in cognitive ageing. Cortex 39, 1107–1128. https://doi.org/10.1016/S0010-9452(08)70880-3
- Tomassini, A., Hezemans, F.H., Ye, R., Tsvetanov, K.A., Wolpe, N., Rowe, J.B., 2022. Prefrontal Cortical Connectivity Mediates Locus Coeruleus Noradrenergic Regulation of Inhibitory Control in Older Adults. https://doi.org/10.1523/JNEUROSCI.1361-21.2022
- Tona, K.D., Keuken, M.C., de Rover, M., Lakke, E., Forstmann, B.U., Nieuwenhuis, S., van Osch, M.J.P., 2017. In vivo visualization of the locus coeruleus in humans: quantifying the test–retest reliability. Brain Struct. Funct. 222, 4203–4217. https://doi.org/10.1007/s00429-017-1464-5
- Tootell, R.B.H., Mendola, J.D., Hadjikhani, N.K., Liu, A.K., Dale, A.M., 1998. The representation of the ipsilateral visual field in human cerebral cortex. Proc. Natl. Acad. Sci. U. S. A. 95, 818–824. https://doi.org/10.1073/PNAS.95.3.818/ASSET/EA084E35-0B78-4B6E-B615-9CA63EF41C07/ASSETS/GRAPHIC/PQ2573470005.JPEG
- Totah, N.K.B.B., Logothetis, N.K., Eschenko, O., 2019. Noradrenergic ensemble-based modulation of cognition over multiple timescales. Brain Res. 1709, 50–66. https://doi.org/10.1016/J.BRAINRES.2018.12.031
- Tsukahara, Jason S., Engle, R.W., 2021. Is baseline pupil size related to cognitive ability? Yes (under proper lighting conditions). Cognition 211, 104643. https://doi.org/10.1016/j.cognition.2021.104643
- Tsukahara, Jason S, Engle, R.W., 2021. Fluid intelligence and the locus coeruleus-norepinephrine system. Proc. Natl. Acad. Sci. 118.
- Tsvetanov, K.A., Henson, R.N.A.A.N., Tyler, L.K., Razi, A., Geerligs, L., Ham, T.E., Rowe, J.B., others, Kamen Tsvetanov, X.A., Henson, R.N.A.A.N., Tyler, L.K., Razi, A., Geerligs, L., Ham, T.E., Rowe, J.B., Centre for Ageing, C., Tsvetanov, K.A., Henson, R.N.A.A.N., Tyler,

- L.K., Razi, A., Geerligs, L., Ham, T.E., Rowe, J.B., 2016. Extrinsic and intrinsic brain network connectivity maintains cognition across the lifespan despite accelerated decay of regional brain activation. J. Neurosci. 36, 3115–3126. https://doi.org/10.1523/JNEUROSCI.2733-15.2016
- Tu, T., Paisley, J., Haufe, S., Sajda, P., 2019. A state-space model for inferring effective connectivity of latent neural dynamics from simultaneous EEG/fMRI, Advances in Neural Information Processing Systems.
- Tucholka, A., Fritsch, V., Poline, J.-B., Thirion, B., 2012. An empirical comparison of surface-based and volume-based group studies in neuroimaging. Neuroimage 63, 1443–1453. https://doi.org/10.1016/J.NEUROIMAGE.2012.06.019
- Uddin, L.Q., 2015. Salience processing and insular cortical function and dysfunction. Nat. Rev. Neurosci. https://doi.org/10.1038/nrn3857
- Uddin, L.Q., Yeo, B.T.T., Spreng, R.N., 2019. Towards a Universal Taxonomy of Macro-scale Functional Human Brain Networks. Brain Topogr. 32, 926–942. https://doi.org/10.1007/s10548-019-00744-6
- Uematsu, A., Tan, B.Z., Ycu, E.A., Cuevas, J.S., Koivumaa, J., Junyent, F., Kremer, E.J., Witten, I.B., Deisseroth, K., Johansen, J.P., 2017. Modular organization of the brainstem noradrenaline system coordinates opposing learning states. Nat. Neurosci. 20, 1602–1611. https://doi.org/10.1038/nn.4642
- Urai, A.E., Braun, A., Donner, T.H., 2017. Pupil-linked arousal is driven by decision uncertainty and alters serial choice bias. Nat. Commun. 8, 1–11.
- Vaillant, M., Miller, M.I., Younes, L., Trouvé, A., 2004. Statistics on diffeomorphisms via tangent space representations. Neuroimage 23, 161–169. https://doi.org/10.1016/j.neuroimage.2004.07.023
- van den Brink, R.L., Nieuwenhuis, S., Donner, T.H., Brink, R.L. van den, Nieuwenhuis, S., Donner, T.H., 2018. Amplification and suppression of distinct brainwide activity patterns by catecholamines. J. Neurosci. 38, 7476–7491. https://doi.org/10.1523/JNEUROSCI.0514-18.2018
- van den Brink, R.L., Pfeffer, T., Donner, T.H., 2019. Brainstem modulation of large-scale intrinsic cortical activity correlations. Front. Hum. Neurosci. 13, 340. https://doi.org/10.3389/fnhum.2019.00340
- Van den Brink, R.L., Pfeffer, T., Warren, C.M., Murphy, P.R., Tona, K.D., van der Wee, N.J.A., Giltay, E., Van Noorden, M.S., Rombouts, S.A.R.B., Donner, T.H., Nieuwenhuis, S., 2016. Catecholaminergic neuromodulation shapes intrinsic MRI functional connectivity in the human brain. J. Neurosci. 36, 7865–7876. https://doi.org/10.1523/JNEUROSCI.0744-16.2016
- Van Essen, D.C., 2005. A Population-Average, Landmark- and Surface-based (PALS) atlas of human cerebral cortex. Neuroimage 28, 635–662. https://doi.org/10.1016/j.neuroimage.2005.06.058
- Vassena, E., Silvetti, M., Boehler, C.N., Achten, E., Fias, W., Verguts, T., 2014. Overlapping neural systems represent cognitive effort and reward anticipation. PLoS One 9, e91008. https://doi.org/10.1371/JOURNAL.PONE.0091008
- Vazey, E.M., Moorman, D.E., Aston-Jones, G., 2018. Phasic locus coeruleus activity regulates cortical encoding of salience information. Proc. Natl. Acad. Sci. 115, E9439--E9448.

- https://doi.org/10.1073/pnas.1803716115
- Vink, J.J.T., Mandija, S., Petrov, P.I., van den Berg, C.A.T., Sommer, I.E.C., Neggers, S.F.W., 2018. A novel concurrent TMS-fMRI method to reveal propagation patterns of prefrontal magnetic brain stimulation. Hum. Brain Mapp. 39, 4580–4592. https://doi.org/10.1002/HBM.24307
- Walz, J.M., Goldman, R.I., Carapezza, M., Muraskin, J., Brown, T.R., Sajda, P., 2014. Simultaneous EEG-fMRI reveals a temporal cascade of task-related and default-mode activations during a simple target detection task. Neuroimage 102, 229–239. https://doi.org/10.1016/j.neuroimage.2013.08.014
- Walz, J.M., Goldman, R.I., Carapezza, M., Muraskin, J., Brown, T.R., Sajda, P., 2013. Simultaneous EEG-fMRI reveals temporal evolution of coupling between supramodal cortical attention networks and the brainstem. J. Neurosci. 33, 19212–19222. https://doi.org/10.1523/JNEUROSCI.2649-13.2013
- Winkler, A.M., Ridgway, G.R., Webster, M.A., Smith, S.M., Nichols, T.E., 2014. Permutation inference for the general linear model. Neuroimage 92, 381–397. https://doi.org/10.1016/J.NEUROIMAGE.2014.01.060
- Woolrich, M.W., Behrens, T.E.J., Smith, S.M., 2004. Constrained linear basis sets for HRF modelling using Variational Bayes. Neuroimage 21, 1748–1761.
- Yang, X., Kwitt, R., Styner, M., Niethammer, M., 2017. Quicksilver: Fast predictive image registration A deep learning approach. Neuroimage 158, 378–396. https://doi.org/10.1016/j.neuroimage.2017.07.008
- Yellin, D., Berkovich-Ohana, A., Malach, R., 2015. Coupling between pupil fluctuations and resting-state fMRI uncovers a slow build-up of antagonistic responses in the human cortex. Neuroimage 106, 414–427. https://doi.org/10.1016/j.neuroimage.2014.11.034
- Yeo, B.T.T., Sabuncu, M.R., Vercauteren, T., Ayache, N., Fischl, B., Golland, P., 2010. Spherical demons: Fast diffeomorphic landmark-free surface registration. IEEE Trans. Med. Imaging 29, 650–668. https://doi.org/10.1109/TMI.2009.2030797
- Zerbi, V., Floriou-Servou, A., Markicevic, M., Vermeiren, Y., Sturman, O., Privitera, M., von Ziegler, L., Ferrari, K.D., Weber, B., De Deyn, P.P., Wenderoth, N., Bohacek, J., others, 2019. Rapid reconfiguration of the functional connectome after chemogenetic locus coeruleus activation. Neuron 103, 702–718. https://doi.org/10.1016/j.neuron.2019.05.034
- Zhang, M., Liao, R., Dalca, A. V., Turk, E.A., Luo, J., Grant, P.E., Golland, P., 2017. Frequency diffeomorphisms for efficient image registration, in: International Conference on Information Processing in Medical Imaging. pp. 559–570. https://doi.org/10.1007/978-3-319-59050-9\_44
- Zhou, J., Benson, N.C., Kay, K.N., Winawer, J., 2018. Compressive temporal summation in human visual cortex. J. Neurosci. 38, 691–709. https://doi.org/10.1523/JNEUROSCI.1724-17.2017
- Zhou, Y., Friston, K.J., Zeidman, P., Chen, J., Li, S., Razi, A., 2018. The hierarchical organization of the default, dorsal attention and salience networks in adolescents and young adults. Cereb. Cortex 28, 726–737. https://doi.org/10.1093/cercor/bhx307